People's Democratic Republic of Algeria
Ministry of Higher Education and Scientific Research
Ferhat Abbas-Setif1 University
Faculty of Sciences
Department of Physics

Thesis Submitted for the Degree of Doctor 3rd Cycle LMD of Physics in Radiation and Matter

Title:

Application of thermally and optically stimulated luminescence (TL&OSL) in radiation dosimetry: Elaboration and response study of Al_2O_3:Sb and BeO_R dosimeter materials

Presented by: **Chahra-Zed BENKHELIFA**

Board of Examiners:

Prof. Naima AMRANI	University of Setif 1	President
Prof. Fayçal KHARFI	University of Setif 1	Thesis Director
Dr. Lakhdar GUERBOUS	Nuclear Research Centre of Algiers	Examiner
Dr. Khelifa HADDADI	University of Setif 1	Examiner
Dr. Melia HAMICI	University of Setif 1	Invited Member

-February 29th, 2024-

Acknowledgments

I owe a great debt of gratitude to many people whom without their support, assistance, and encouragements, this thesis would not have been possible.

My deepest appreciation goes to Prof. F. Kharfi, my thesis director, for its effort, time, motivation and instructions he provided me throughout my doctoral studies. Its vast knowledge and wealth of experience have inspired me throughout my studies. He has been a tremendous advisor and mentor for me. I would like to thank him for supporting my research.

I would like to express my thankfulness to my thesis committee: Pr. A. Amrani, Dr. L. Guerbous, Dr. K. Haddadi and Dr. M. Hamici, for kindly agreeing to be part of the examining committee and for their useful interventions.

Sincere thanks to all the faculty and staff members of the Department of Physics of Ferhat Abbas Setif-1 University for providing the foundation of knowledge and precious cooperation.

I would like to extend my sincere thanks to Dr. M. Hamici and Dr. E. Şahiner, for their untiring assistance during the experiments, positive and constructive instructions. Their help has broadened my academic knowledge.

Dedication

There are a number of people without whom this thesis would not be possible, and to whom I am fully indebted and grateful for the assistance provided.

To my parents Bachir and Saliha Abdelkrim, who have been a source of inspiration and strength when I thought of giving up, and who continue to provide moral, emotional and financial support.

To my sisters Randa and Nawaim and my brothers in law, for their love and support.
To my nephews Iskander, Lyne, Yousser and Kinan.

To my friend F. Houda who has been there for me emotionally and intellectually as I've worked on my coursework.

Content

List of Figures

Chapter I

Chapter II

Chapter III

Chapter IV

Chapter V

List of Tables

Chapter II

Chapter III

Chapter IV

Chapter V

List of Acronyms

CB : Conduction Band.

eV : Electronvolt.

FOK : First-Order Kinetics.

GCD : Glow Curve Deconvolution.

GOK : General-Order Kinetics.

HELA : Hybrid Evolutionary Linear Algorithm.

ICRP : International Commission on Radiological Protection.

ICSD : Inorganic Crystal Structure Database.

IR : Infrared.

JCPDS : Joint Committee on Powder Diffraction Standards.

K : Kelvin.

OSLD : Optically Stimulated Luminescent Dosimetry.

PM : Photomultiplier.

RPL : Radiophotoluminescence.

TLD : Thermo-Luminescent dosimetry.

UV : Ultraviolet.

VB : Valence Band.

VESTA : Visualization for Electronic Structural Analysis.

Introduction

Radiation dosimetry is a field of physical science that quantifies the energy that ionizing radiation, whether from direct or indirect exposure, deposits in a specific material. It estimates and calculates quantities (doses) that represent the amount of energy absorbed by a material and its deposition rate [1]. Various dosimetry systems and techniques are used in different domains around machines and sources delivering ionizing radiation. Dosimetry techniques capabilities depend on type, intensity and energy of involved radiation. The most employed quantities to quantify the radiation intensity and hazard are absolute or relative dose and dose rate. Radiation dosimeters are classified into two main categories: active and passive. Radiation dosimetery has very important and effective use in radiation protection and radiation applications such as in medicine for radiation therapy and imaging and archeology for dating. The application of ionizing radiation are nowadays extended to many other fields such as agriculture, nondestructive testing, pharmacology…

Thermoluminescence (TL) and optically stimulated luminescence (OSL) have become the techniques of choice in many radiation dosimetry areas and applications. The techniques are being widespread used in various radiation dosimetry fields, such as personal, environmental, retrospective, and space. In TL and OSL dosimetry ionizing radiations induce electrons and holes trapping in the forbidden band. The amount of trapped electrons is proportional to radiation intensity. In both techniques, the signals are collected through the electrons and holes recombination after external stimulation. In TL, thermal stimulation is used, which is provided by heat control system, while in OSL, a controlled-light optical stimulation is used [2]. Theoretical studies on TL and OSL mostly consist of investigating the differential rate equations that govern the charge carrier transition (usually electrons and holes) between different states of trapping related to impurities, defects in the sample under study, and the valence and conduction bands. The search for new prospective of TL and OSL materials continues to be a primary area of study in luminescence dosimetry [3]. It is the subject of many researches and publications.

In the present thesis project, the main purpose is the synthesis, for first time, of Sb-doped Al_2O_3 based luminescent material via the sol-gel technique and its characterization using different techniques. The elaborated α-Al_2O_3:Sb is tested for use in radiation dosimetry and its dosimetry properties were checked . It is also a question to study the OSL and TL kinetics of a new-developed BeO_R dosimeter through various methods for determining some parameters of

interest. Moreover, the TL and OSL dose responses are also established, allowing effective use in radiation dosimetry.

This manuscript is subdivided into five chapters covering the theoretical and experimental aspects of the undertaken work. The first chapter includes the theory of thermoluminescence (TL) and optically stimulated luminescence (OSL) and mathematics models governing both phenomena. The second chapter covers the applications of TL and OSL in radiation dosimetry. The third chapter presents the available literature on TL and OSL materials and their uses in radiation dosimetry. In fourth chapter, the experimental work and results on the elaboration, characterization and use of α-Al_2O_3:Sb in radiation dosimetry are presented and discussed. The last chapter is reserved to the presentation and discussion of the obtained results from TL&OSL kinetics and dose-response study of BeO_R.

CHAPTER I

Principle and kinetics of Thermoluminescence (TL) and Optically Stimulated Luminescence (OSL)

I.1 Luminescence

Luminescent materials (phosphors) are solids that convert some types of energy into electromagnetic radiation more and beyond thermal radiation [4]. This emitted electromagnetic radiation is usually in the visible range, although it can also be in the UV or infrared regions [5]. The wavelength of emitted light distinguishes the luminescent substances [6]. Different types of luminescence can be classified according to the type of used radiation to excite emission. Thus, photoluminescence is excited by electromagnetic (often ultraviolet) radiation, radioluminescence by ionizing radiation, and cathodoluminecence by a beam of energetic electrons. Luminescence can also be caused by the energy of chemical reactions known as chemiluminescence, by frictional and electrostatic forces called triboluminescence, by electric fields called electroluminescence, by sound waves called sonoluminescence [7]. Thermoluminescence does not refer directly to thermal excitation, but rather to warming a preexcited phosphor [8].

Luminescence can be classified based on the time taken (i.e., characteristic time τ_c) between radiation absorption and emission of light (see Figure I.1).

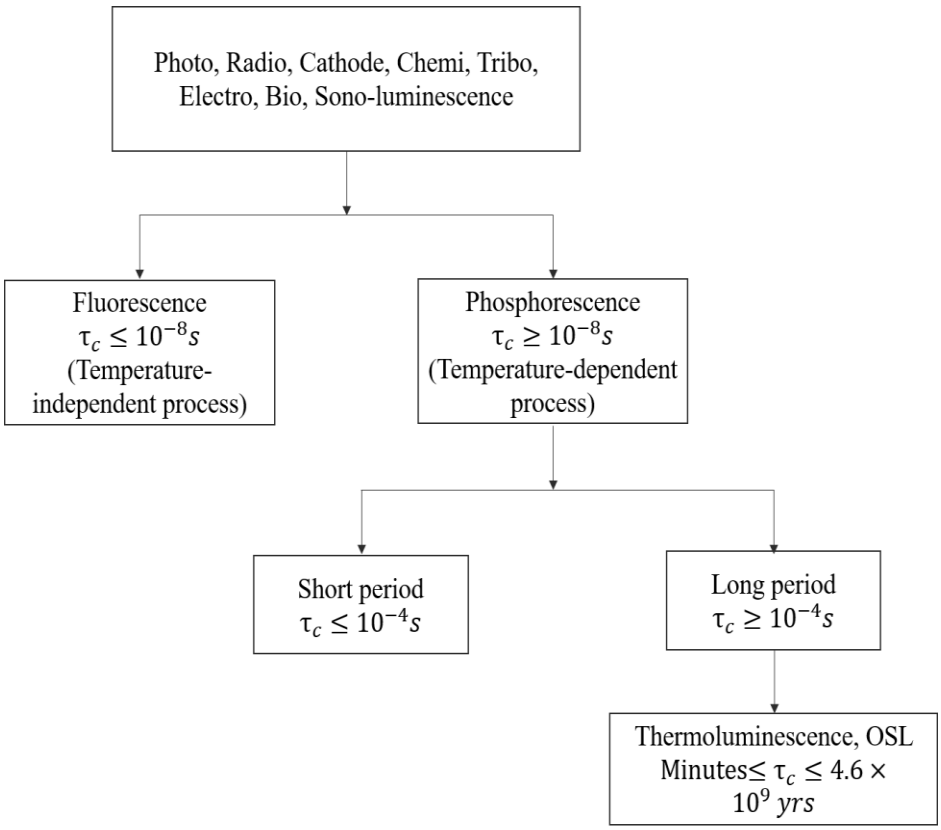

Figure I. 1. The lifetime based 'family tree' of luminescence phenomena [9].

I.2 Luminescence classification

The fluorescence is essentially independent of temperature, whereas the phosphoresence decay is strongly dependent on temperature. The phosphorescence can be split into two types: short period ($\leq 10^{-4}\ s$) and long period ($\geq 10^{-4}\ s$). The energy transitions involved in the generation of fluorescence and phosphorescence emissions are depicted in Figure I.2.

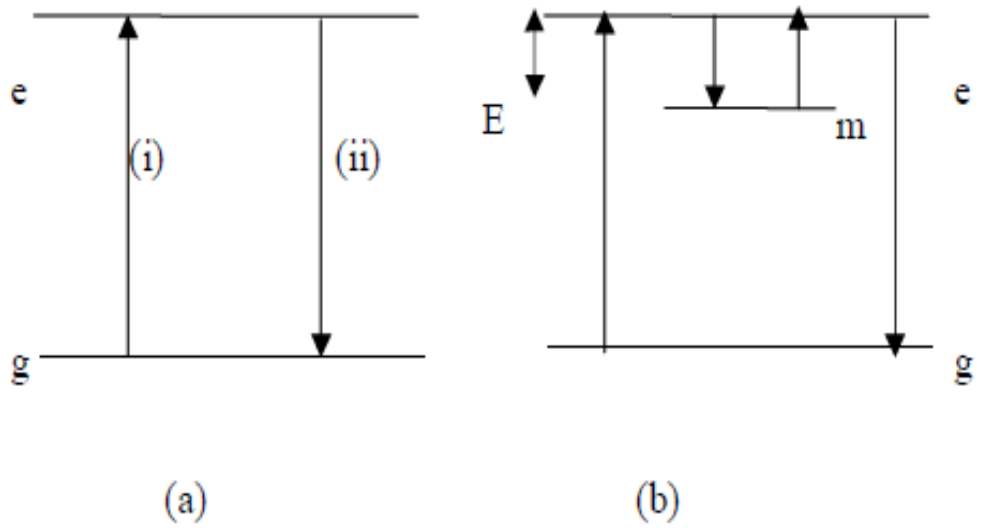

Figure I. 2. (a) fluorescence and (b) phosphorescence, where 'e' is excited state, 'g' is ground state, 'm' is meta-stable level and 'E' is energy difference between 'm' and 'e' [9].

Reffering to Figure I.2 (a)(i), luminescence emission can be explained by the energy transfer from radiation to the electrons of a solid, resulting in electron excitation from a ground state to an excited state. When an excited electron returns to its ground state, a luminescence photon is emitted, as shown in Figure I.2 (a)(ii). Thus, for fluorescence.

The first explanation of temperature-dependent phosphorescence was given by Jablonski in 1935, who introduced a meta-stable level in the forbidden gap between the excited and ground states, as illustrated in Figure I.2 (b). An electron excited can be trapped in the meta-stable state until it is given enough energy to return to the ground state through light emission. Thus, the phosphorescence delay corresponds to the time the electron spends in the meta-stable state. The average time spent in the trap at temperature T is given by:

$$\tau = s^{-1}\exp(\frac{E}{kT}) \tag{I.1}$$

Where s is the frequency factor (s^{-1}), E represents the activation energy or trap depth (eV), k is Boltzmann's constant (Ev.K^{-1}), T is the absolute temperature (K) [9].

I.3 Thermoluminescence (TL)

TL is the light emission by some crystals after being irradiated (α particles, X rays, γ-rays, or other high-energy radiation) when stimulated by heat [10].

Robert Boyle described thermoluminescence phenomenon in 1663, when he observed a strange glimmering light when warming a diamond in the dark. Other scientists, such as Henri Becquerel, studied thermoluminescence, and in 1904, Marie Curie reported that the thermoluminescent characteristics of crystals could be restored by exposing them to radium. In 1945, Randall and Wilkins provided the basic mathematical understanding of thermoluminescence kinetics [11].

I.3.1 Theory of TL

The fundamental theory of TL is based on the presence of imperfections, impurities, and defects in otherwise ordered crystals, which give rise to allowed discrete energy levels in the forbidden gap of the crystal that may capture electrons or holes.

The defect centers may be divided into three categories:

1. Intrinsic,
2. Extrinsic,
3. Defects caused by ionizing radiation.

The intrinsic or native defects include:

- Vacancies or atoms that are missing (known as Schottky defects). A vacancy is a defect that occurs when one atom is extracted from its site without being replaced.
- Interstitial or Frenkel defect. It is made up of an atom X positioned in a crystal X in a non-proper lattice site.
- Substitutional defect. When the lattice site of an atom X in a crystal X is occupied with an atom Y.
- Previous defects in aggregate form.

Extrinsic or impurity defects, such as chemical impurities Y in a crystal X can be:

- Substitutional impurity: an atom Y replaces an atom X.
- Interstitial impurity: an atom Y is inserted in an additional site that does not belong to the perfect crystal.

The purpose of irradiating the material with ionizing radiations is producing free electrons and holes in abundance due to the interaction of the incident radiation with atoms of the bulk sample. The concentration of these defects at room temperature can be increased by heating the

sample and then cooling it suddenly (quenching). The increased number of defects present at higher temperatures may be frozen in this manner.

The free electron in the crystal can be attracted to the localized positive charge by a Coulomb force and trapped in the vacancy. This system or center is known as the *F* center. A positive ion vacancy, on the other hand, represents a hole trap, and the system is known as a *V* center. Other hole centers are also possible: when a hole is trapped by a pair of negative ions, the V_k center is formed. The V_3 center is made up of a neutral halogen molecule that occupies the site of a halogen ion, as depicted in Figure I.3 [12, 13].

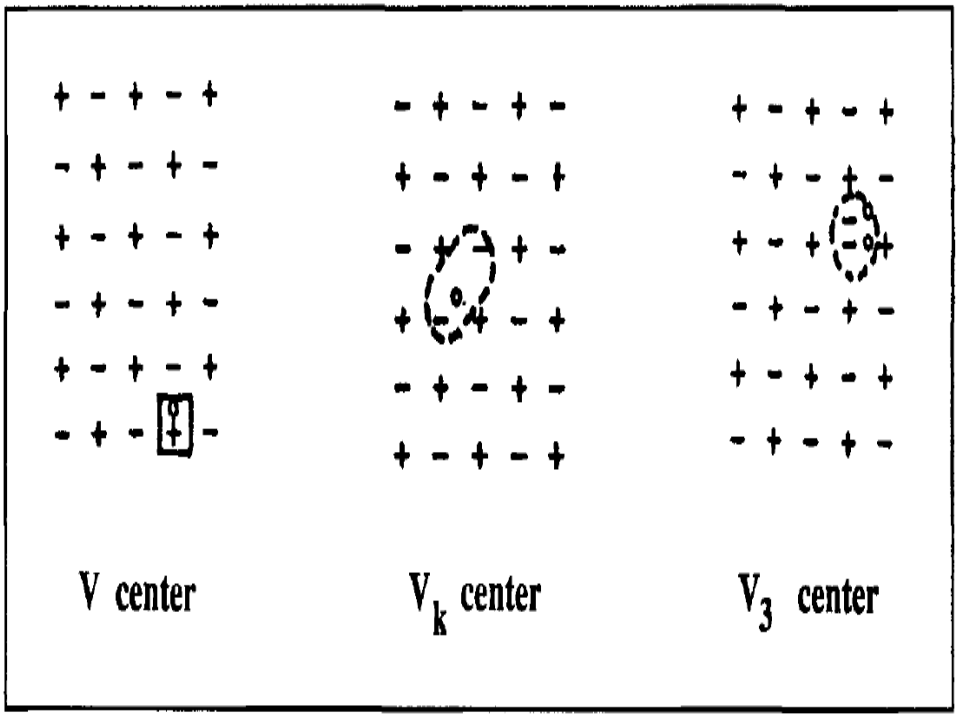

Figure I. 3. Centers V, V_k and V_3 in real crystal [13].

The presence of these defects may introduce two types of levels:

1- Trapping centers (*T*),

2- Luminescence centers (*L*).

During excitation of the solid, the radiation produces electron and hole pairs throughout the sample with a fraction reaching the conduction and valence bands, respectively. These carriers could be trapped in electron and hole traps in the forbidden gap. It is rather conventional to talk about electron traps close to the conduction band and piercing traps (holes) if close to the valence band. Under these conditions, trapped electrons may be raised into the conduction band

during TL readout by heating, following their motion in the conduction band, recombine with a hole in a luminescence center, yielding an emitted photon [14, 15].

Figure I.4 depicts the energy levels of TL phenomenon in a simple representational view.

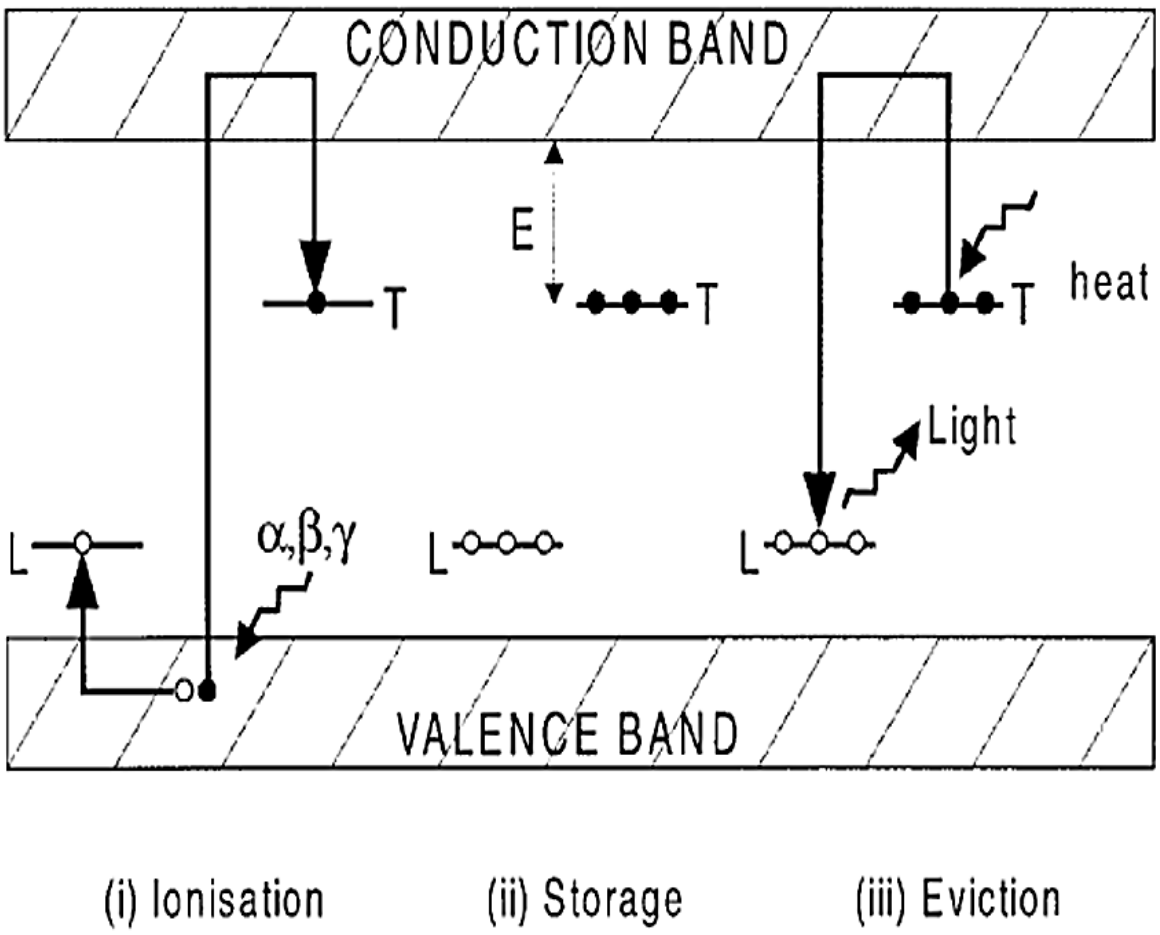

Figure I. 4. Energy level presentation for thermoluminescence [16].

As shown in Figure above, i) ionisation caused by nuclear radiation exposure, with electron and hole trapping at defects *T* and *L*, respectively. ii) radiation energy storage over time ; the lifetime of the electrons in traps depends on the trap's energy depth *E* also known as the activation energy below the conduction band. iii) electrons are evicted from electron traps by heating, and some of these reach luminescence centres (*L*) ; with emission of light due to the recombination with holes into these centres.

The characterization of the TL signal is by the so-called "glow curve", with distinct peaks occurring at different temperatures, which relate to the electron traps present in the sample [16].

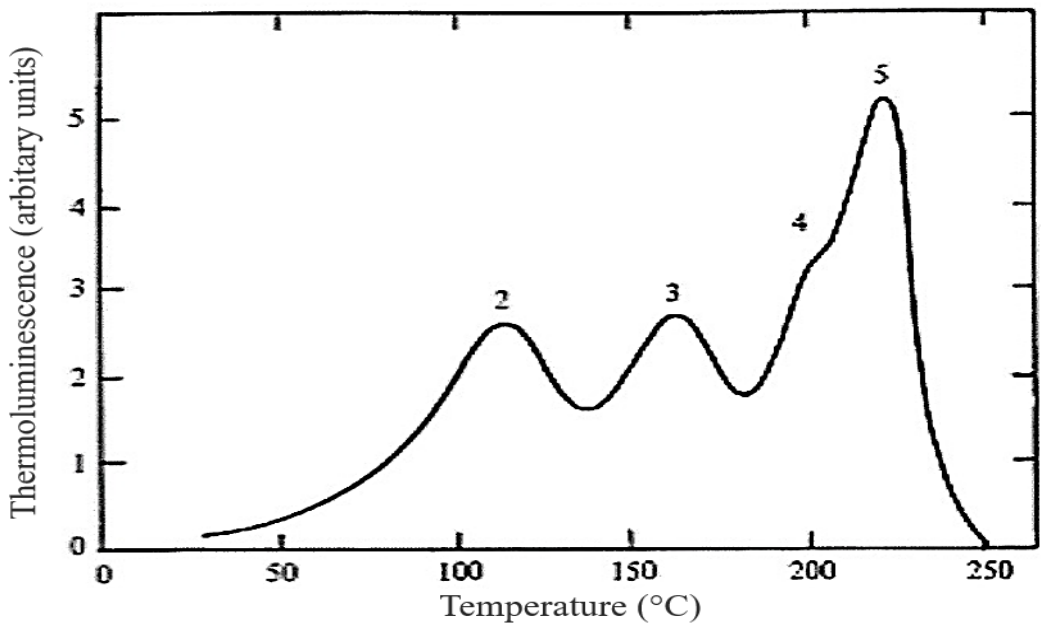

Figure I. 5. The glow curve of Mg and Ti doped-LiF, irradiated by γ-rays at room temperature. Heating rate β=3°C.s^{-1}[9].

Figure I.5 presents the TL glow curve of LiF:Mg, Ti irradiated with γ-ray source, revealing 5 peaks occurring at different temperatures with a peak recorded at a low temperature (i.e., below 50 °C) that is non-stable and possesses high fading for a linear heating rate of 3°C. s^{-1}.

I.3.2 Kinetics of thermoluminescence (TL)

I.3.2.1 Thermoluminescence: equations governing the TL peak

In 1956, Adirovitch proposed a set of three equations to explain the phosphorescence decay.

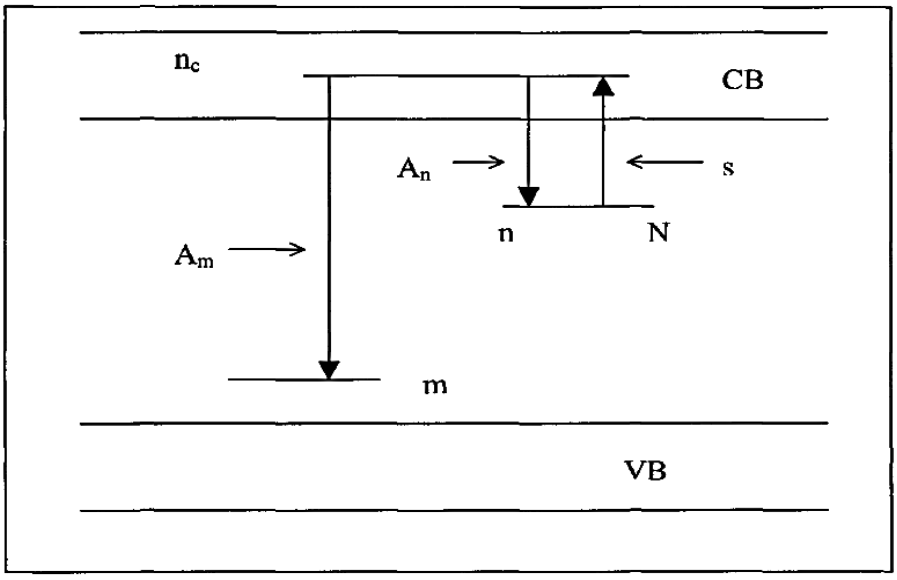

Figure I. 6. Adirovitch's energy level diagram for the decay of phosphorescence [12].

In 1960, Haering-Adams and Halperin-Braner both utilized the same concept for explaining the flow of charge between delocalized bands and localized energy levels during trap emptying. Figure I.6 depicts the diagram of the energy levels.These equations which control the transition of electrons from the trapping center to the recombination center via the conduction band were applied for the first time by Halperin and Braner in an attempt to explain TL glow-curves as follows:

$$I = -\left(\frac{dm}{dt}\right) = mn_c A_m \tag{I.2}$$

$$\left(\frac{dn}{dt}\right) = -np + n_c(N-n)A_n \tag{I.3}$$

$$\frac{dm}{dt} = \frac{dn}{dt} + \frac{dn_c}{dt} \tag{I.4}$$

where,

I symbolizes the TL glow curve's intensity,

m and n are the densities of holes and electrons in the recombination and trap centres, respectively,

n_c is the density of electrons in the conduction band,

A_m is the recombination probability,

A_n is the retrapping probability,

t is the time corresponding to T,

N is the density of the total trap center,

These are the basic equations that have been used by many researchers to explain the occurrence of the TL glow curve [12, 17].

I.3.2.2 Randall-Wilkins model: First-order kinetics

Basing on the simplest model consisting of conduction band and valence band, Randall and Wilkins demonstrated in 1945 that if no retrapping of the released electrons is assumed, a TL peak resulting from a single electron trapping state and a single kind of center results in first-order kinetics. Probability per unit time for trapped electrons to escape from the trap is given by:

$$p = s\exp(-\frac{E}{kT}) \tag{I.5}$$

If the temperature T is kept constant, then the number of trapped electrons n decreases with time t according to the following expression:

$$\frac{dn}{dt} = -pn \tag{I.6}$$

By integrating this equation, one obtains

$$n = n_0 \, exp\left[-s \exp\left(-\frac{E}{kT}\right).t\right] \tag{I.7}$$

Where

n_0 is the number of trapped electrons at initial time t_0

One assumes that:

- the thermoluminescent material is irradiated at a low enough temperature to prevent electrons from being released from the trap,
- the electrons in the conduction band have a short lifetime,
- all charges released from the trap are recombined at the luminescent center,
- the luminiscence efficiency of the recombination center does not depend on temperature,
- the concentrations of traps and recombination centers do not depend on temperature,
- no electrons are retrapped after being released from the trap.

According to the previous assumptions, at a constant temperature, the TL intensity is directly proportional to the detrapping rate, dn/dt.

$$I(t) = -c\left(\frac{dn}{dt}\right) = cpn \tag{I.8}$$

Where

c is a constant that can be set to unit

The exponential decay of phosphorescence is represented by Eq. (I.8).

Remembering Eq. (I.7), we get:

$$I(t) = n_0 s \, exp\left(-\frac{E}{kT}\right) exp\left[-st \exp\left(-\frac{E}{kT}\right)\right] \tag{I.9}$$

Heating the material at a constant rate of temperature, $\beta = dT/dt$, we get from Eq. (I.6):

$$\int_{n_0}^{n} \frac{dn}{n} = -\left(\frac{s}{\beta}\right) \int_{T_0}^{T} exp\left(-\frac{E}{kT'}\right) dT'$$

$$\ln(n) - \ln(n_0) = -\left(\frac{s}{\beta}\right)\int_{T_0}^{T} exp\left(-\frac{E}{kT'}\right)dT'$$

And again

$$n = n_0 \exp\left[-\frac{s}{\beta}\int_{T_0}^{T} \exp\left(-\frac{E}{kT'}\right)dT'\right] \quad \text{(I.10)}$$

Using now Eq. (I.8)

$$I(T) = n_0 s \exp\left(-\frac{E}{kT}\right) exp\left[-\frac{s}{\beta}\int_{T_0}^{T} \exp\left(-\frac{E}{kT'}\right)dT'\right] \quad \text{(I.11)}$$

The peaks of first-order are asymmetric and their ascending range is significantly broader than the descending range [18, 19].

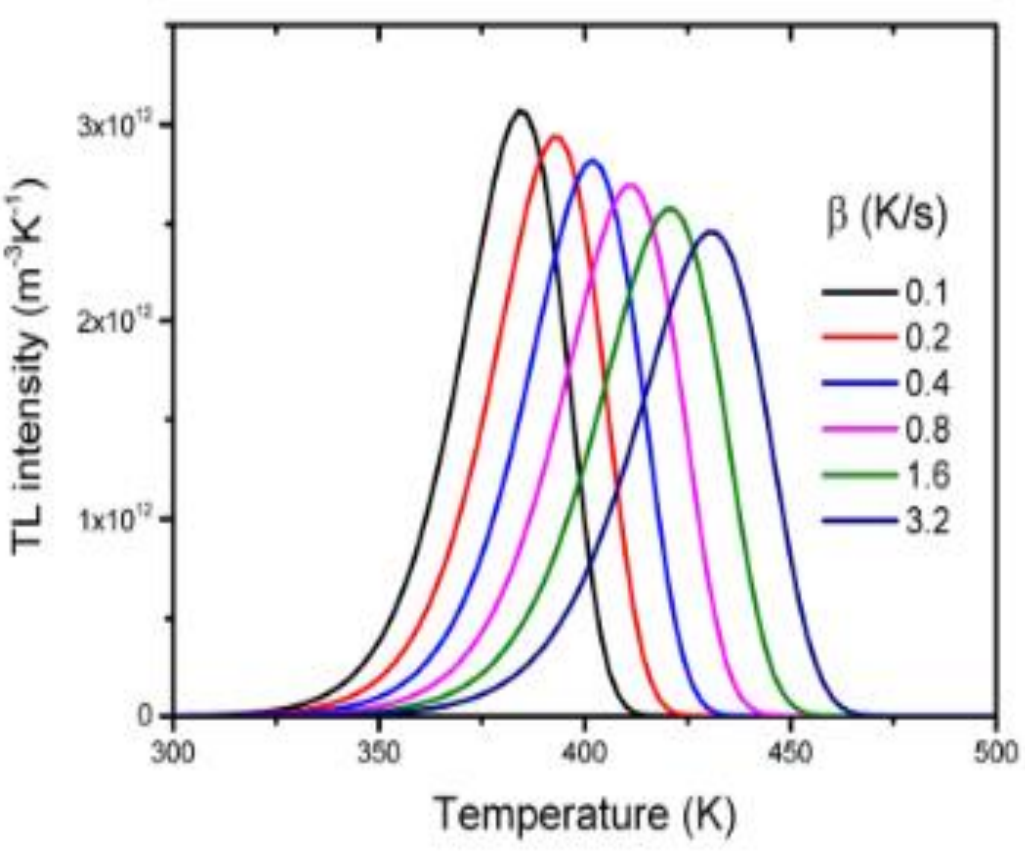

Figure I. 7. Calculated TL glow peaks using Randall-Wilkins model for $n_0 = 10^{14}\, m^{-3}$, $s = 10^{11}\, s^{-1}$ and various trap depth E values [20].

Figure I.7 shows TL glow peaks calculated using First-order-kinetics model for fixed values of n_0 and s, while the linear heating rate β and activation energies E vary.

I.3.2.3 Garlick-Gibson model: Second-order kinetics

In 1948, Garlick and Gibson extended their researches and considered the case where an excited electron can either recombine with a hole in a recombination center or retrap into one of the empty electron traps.

One assumes that the retrapping is relatively strong. So, the number of trapped electrons can be expressed by:

$$\frac{dn}{dt} = -n^2 s' \exp(-\frac{E}{kT}) \tag{I.12}$$

Where $s' = s/N$

Eq. (I.12) leads to the Garlick-Gibson equation under second-order kinetics

$$I(T) = \frac{n_0^2 s' \, exp\left(-\frac{E}{kT}\right)}{\left[1+\frac{n_0 s'}{\beta}\int_{T_0}^{T} exp\left(-\frac{E}{kT'}\right)dT'\right]^2} \tag{I.13}$$

The feature of this equation is that the glow is nearly symmetric [21, 22]. Figure I.8 reveals the variation in TL peak shape as the kinetic process changes.

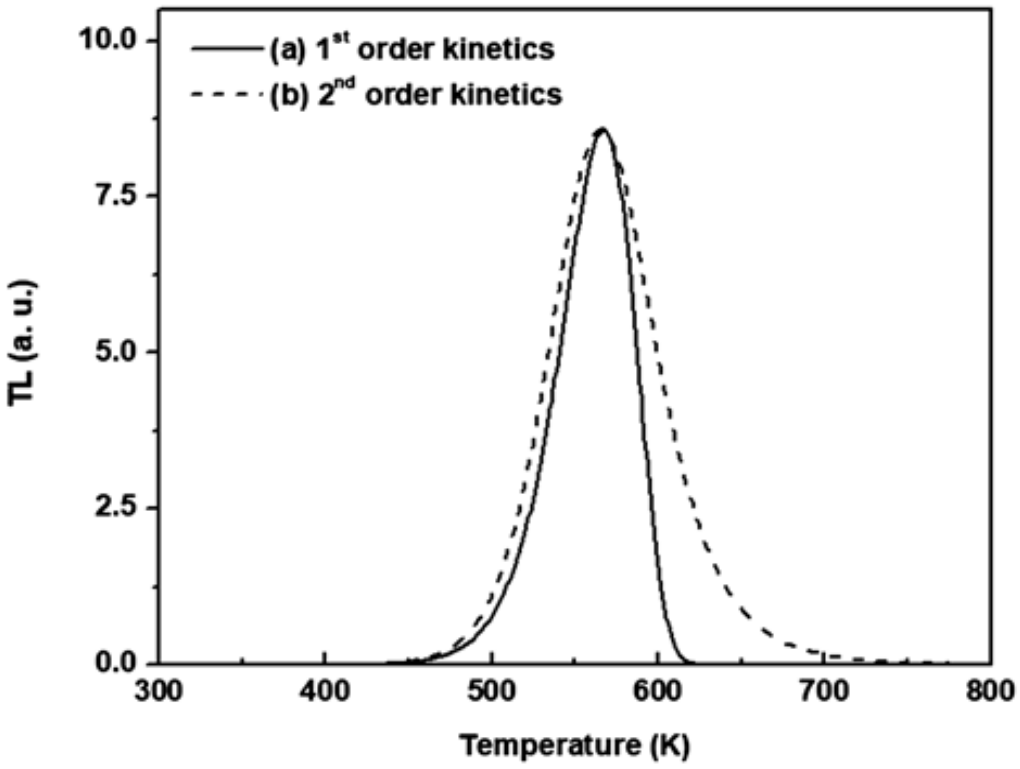

Figure I. 8. Variation in the shape of glow peak depending on the kinetic process [23].

I.3.2.4 May-Partridge model: General-order kinetics

If neither the first-order kinetics (rate of recombination greater than rate of retrapping) nor the second-order kinetics (rate of recombination and retrapping equal) conditions are met, general-order kinetics may be applied to the glow peak. May and Partridge presented the following general order kinetic model for TL glow peaks [24-26]:

$$\frac{dn}{dt} = -n^b s'' \exp(-\frac{E}{kT}) \tag{I.14}$$

where

$s'' = \frac{s}{N} n_0^{b-1}$ and b is the kinetics order ranging between 1 and 2 ($1 < b \leq 2$).

The appearing quantity s in the case of first order equation has a precise physical meaning: it should be multiplied by a transition probability factor to represent the number of times per second that a bound electron interacts with the lattice phonons. In the case of second and general order, the quantities s' and s'' are called pre-exponential factors.

By introducing a linear heating rate $\beta = dT/dt$, and from Eq.(I.14), the TL intensity, I, can be written as

$$I(T) = n_0^b s'' \, exp\left(-\frac{E}{kT}\right)\left[1 + \frac{s'' n_0^{b-1}(b-1)}{\beta}\int_{T_0}^{T} \exp(-\frac{E}{kT'})dT'\right]^{-\frac{b}{b-1}} \tag{I.15}$$

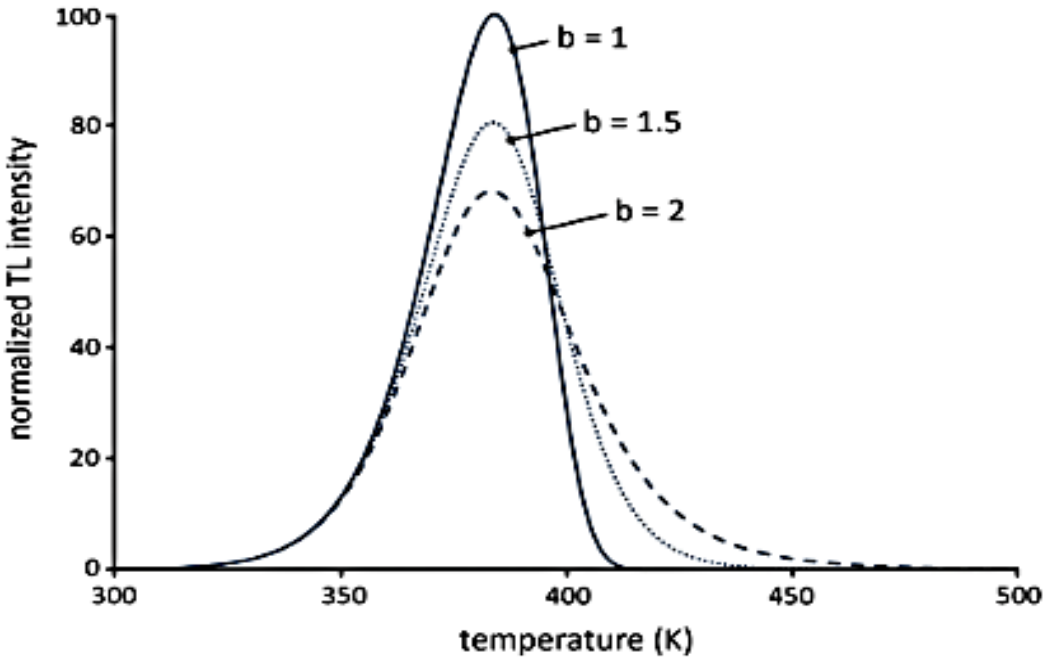

Figure I. 9. *First, second and general-order kinetics glow curve shape for* $E = 1eV$, $N = n_0 = 1m^{-3}$, $s = 10^{12}s^{-1}$ *and* $\beta = 1K/s$ *[27].*

For b = 2, Eq. (I.15) is transformed into the second order kinetics equation. The frequency factor and the initial trapped charges concentration act like an effective frequency factor, which is a fundamental property of Eq. (I.15) [26].

The shape of glow peaks for first, second and general order kinetics for given values of E, N, n_0, s and β are depicted in Figure I.9.

I.3.3 Experimental methods of TL trapping parameters determination

The TL characteristics of any material are typically labeled by a few parameters (trapping parameters) such as the TL process's order of kinetics, activation energy or trap depth, and frequency factor. Many approaches are used to determine these experimentally. However, there is little evidence that the TL methods can provide consistent quantitative information, particularly on trap depth and frequency factor. In practice, a multi-peak TL glow curve is frequently encountered, and it is necessary to isolate the peak under study from the overlapping neighboring peaks before beginning any analysis.

I.3.3.1 The initial rise (IR) method

This is the simplest method for estimating the depth of trap and is independent of the order of kinetics involved. The method is based on the following assumptions : i) in the early rising temperature range, i.e. $T<<T_m$, the rate of change of trapped carrier population is negligible (and thus intensity is strictly proportional to *exp (-E/kT)*, ii) the frequency factor essentially remains constant, and iii) there is no overlap of glow peaks belonging to different trapping levels. As a result, this method would imply finding

$$E_{ir} = -k\frac{d(\ln I)}{d\left(\frac{1}{T}\right)} \tag{I.16}$$

If the plot of $\ln I$ vs. $1/T$ is made over this initial rise region where $T<<T_m$, a straight line with slope E_{ir}/k is obtained, from which the activation energy is easily found. The initial rise technique can only be used when the glow peak is well defined and clearly separated from the other peaks [28].

I.3.3.2 Various heating rates (VHR) method

The method of various heating rates for evaluating the activation energy is based on two different heating rates for a first-order peak that represents a peak-shaped asymmetric curve

with the fall-off side significantly narrower than the low-temperature side. By deriving Eq. (I.11) to zero, one gets the maximum condition:

$$\frac{\beta_1 E}{kT_{m1}^2} = s.exp\left(-\frac{E}{kT_{m1}}\right)$$

(I.17)

$$\frac{\beta_2 E}{kT_{m2}^2} = s.exp\left(-\frac{E}{kT_{m2}}\right)$$

From which, the activation energy can be calculated by eliminating s as:

$$E = k\frac{T_{m1}T_{m2}}{T_{m1}-T_{m2}}\ln\left[\left(\frac{\beta_1}{\beta_2}\right).\left(\frac{T_{m2}}{T_{m1}}\right)^2\right] \quad \text{(I.18)}$$

Another method is to try various heating rates and plot $\ln\left(\frac{T_m^2}{\beta}\right)$ versus $\frac{1}{T_m}$ which should result in a straight line with slope E/k. Gartia et al., proposed the two heating rates method for any order of kinetics ($1.1 \leq b \leq 2.5$) basing on the variation of I_m with b. This variation is significantly faster than the T_m with b variation [12, 29].

$$E = \frac{kT_{m1}T_{m2}}{T_{m1}-T_{m2}}\ln\frac{I_{m1}}{I_{m2}} \quad \text{(I.19)}$$

I.3.3.3 Peak shape (PS) method

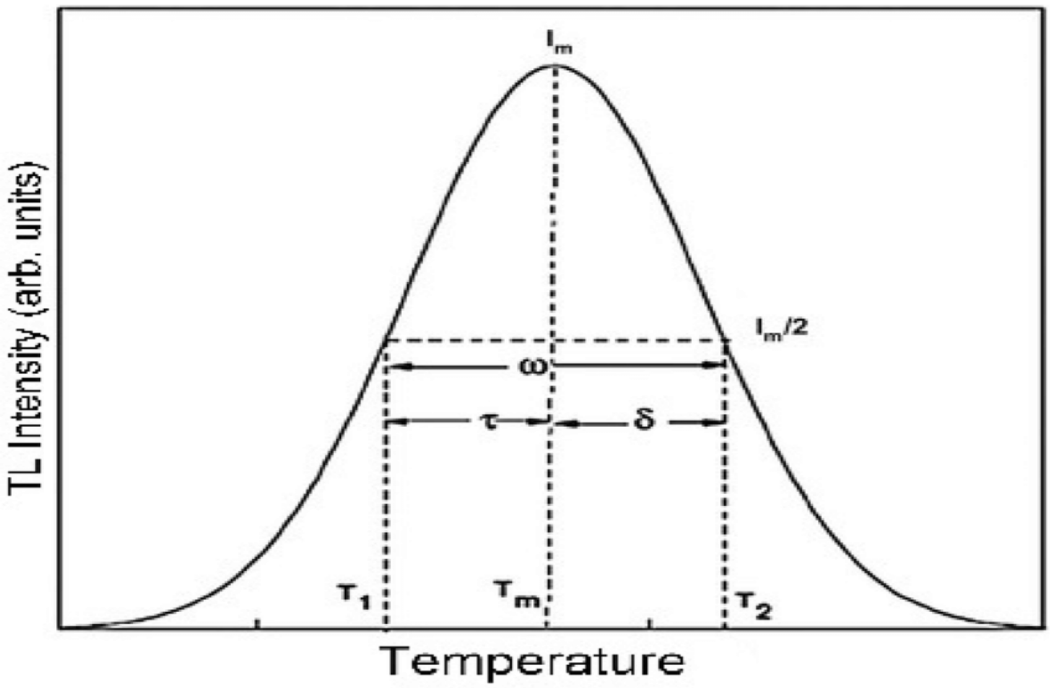

Figure I. 10. A single peak's parameters [30].

Chen described a method for calculating activation energy in cases where the order is not necessarily first or second but can be a non-integer value. This method is based on determining the maximum and half-intensity temperatures, as depicts Figure I.10.

where

T_m, T_1, T_2 are the maximum peak temperature and the temperatures on either side of the maximum temperature, corresponding to half intensity,

$\tau = T_m - T_1$: is the half-width of the peak on the low temperature side,

$\delta = T_2 - T_m$: is the half-width towards the glow peak's fall-off,

$\omega = T_2 - T_1$: is the peak's total half-width,

$\mu_g = \frac{\delta}{\omega}$: is the symmetry factor.

Chen's method entails finding the temperature at maximum, for given values of *b*, *s*, *E*, β using a computer.

The values that were used were

$$0.7 \leq b \leq 2.5$$

$$10^5 s^{-1} \leq s \leq 10^{13}$$

$$0.1eV \leq E \leq 1.6eV$$

$$\beta = 0.5°C/s$$

Once the value of T_m corresponding to I_m has been determined, the values T_1 and T_2 can be calculated numerically by solving the following equation:

$$I(t) = \frac{I_m}{2}$$

Chen proposed a general formula for calculating activation energy as:

$$E_\alpha = c_\alpha \left(\frac{kT_m^2}{\alpha}\right) - b_\alpha(2kT_m) \qquad \text{(I.20)}$$

where α is τ, δ or ω and the values of c_α and b_α can be summarized as :

$c_\tau = 1.51 + 3.0(\mu_g - 0.42)$ $\qquad$ $b_\tau = 1.58 + 4.2(\mu_g - 0.42)$

$c_\delta = 0.976 + 7.3(\mu_g - 0.42)$ $\qquad$ $b_\delta = 0$

$c_\omega = 2.52 + 10.2(\mu_g - 0.42)$ $\qquad$ $b_\omega = 1$

$\mu_g = 0.42$ $\qquad$ for first-order kinetics

$\mu_g = 0.52$ $\qquad$ for second-order kinetics

According to Chen's graph the values of μ_g range from 0.36 to 0.55 for b values ranging from 0.7 to 2.5, see Figure I.11.

Once the activation energy has been determined, the frequency factor can be calculated using the following equation for general-order kinetics [12, 30]

$$s = \left(\frac{\beta}{T_m^2}\right)\left(\frac{E}{k}\right)\frac{1}{1+(b-1)\left(\frac{2kT_m}{E}\right)}exp\left(\frac{E}{kT_m}\right) \quad \text{(I.21)}$$

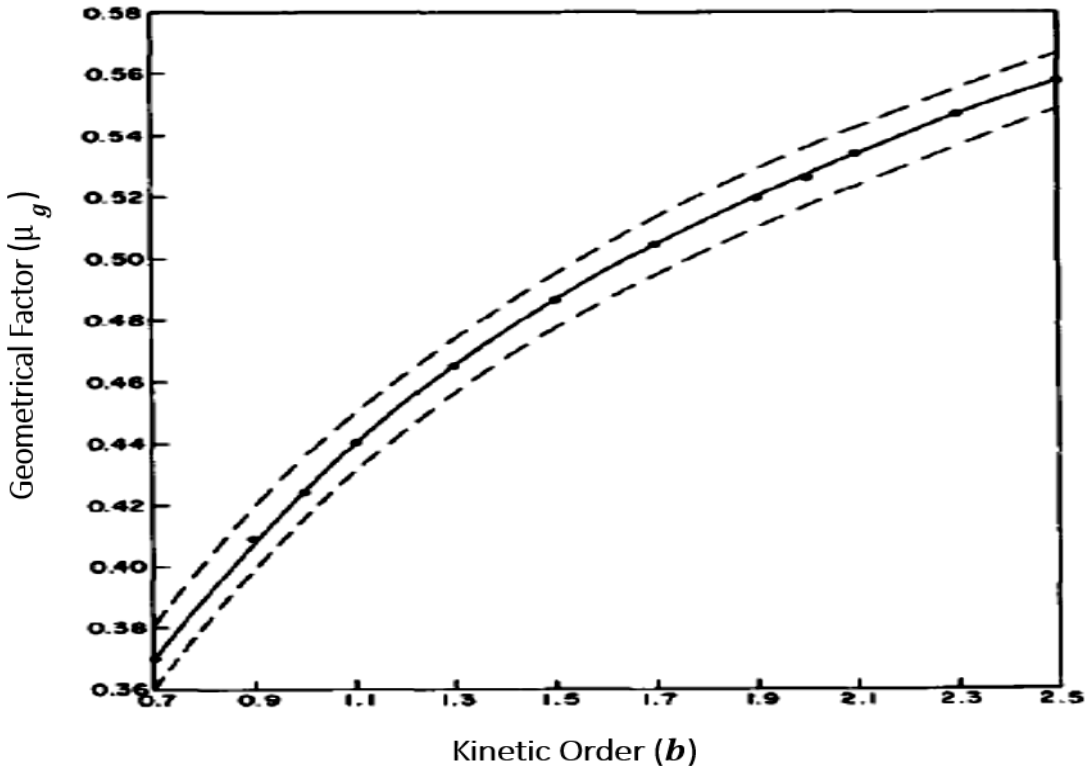

Figure I. 11. Calculated symmetry factor as a function of the given kinetics order [30].

I.3.3.4 Isothermal decay method

The isothermal decay technique is not strictly speaking a TL-based method, but it is a general method for determining E and s. The TL response is recorded as a function of time while the sample is kept at a constant temperature that is slightly below the peak's maximum temperature and holding it there for a predetermined period of time.

May and Partridge proposed using the isothermal decay method in general for any order. It is possible to find the order b in this case.

By integrating Eq.(I.14), the following expression can be obtained

$$\frac{n^{1-b}-n_0^{1-b}}{1-b} = -s''exp\left(-\frac{E}{kT}\right)t \quad \text{(I.22)}$$

With substituion

$$a = n_0^{1-b}$$

$$c = -(1-b)s''\exp\left(-\frac{E}{kT}\right) \quad \text{(I.23)}$$

$$\text{n} = (a+ct)^{\frac{1}{1-b}} \quad \text{(I.24)}$$

and since $I = -dn/dt$, one obtains:

$$I = -\frac{c}{1-b}(a+ct)^{\frac{b}{1-b}}$$

That is

$$I^{\frac{1-b}{b}} = (a+ct)\left[s''exp\left(-\frac{E}{kT}\right)\right]^{\frac{1-b}{b}}$$

That can be writen

$$I^{\frac{1-b}{b}} = A + B.t \quad \text{(I.25)}$$

where

$$A = a\left[s''exp\left(-\frac{E}{kT}\right)\right]^{\frac{1-b}{b}} \quad \text{(I.26)}$$

$$B = c\left[s''exp\left(-\frac{E}{kT}\right)\right]^{\frac{1-b}{b}} \quad \text{(I.27)}$$

The *I(t)* function given by Eq. (I.25) is a linear function of time; thus, a plot of the left side versus time yields a straight line when the best *b* value is determined by iterative procedure using different values of *b* to best fit Eq. (I.25) [12].

I.3.3.5 Computerized glow curve deconvolution (CGCD)

Since 1980, computerized glow curve deconvolution (CGCD) has been widely used to deconvolve a complex thermoluminescent glow curve into individual peak components. After determining each component, the trapping parameters can be calculated. This method, which is

widely used for many dosimetric materials, can provide a clear estimate of the TL signal. The easiest part of a CGCD analysis is achieving a good fit to the experimental glow curves.

The experimental TL glow curve has strongly overlapping peaks, the CGCD analysis must be used with caution. The main issue is that the fundamental TL kinetics equations, namely the Randall-Wilkins equation for first-order kinetics and the Garlick-Gibson equation for second-order kinetics, give the glow peak TL intensity as a function of: n_0, E, s, T. It is then necessary to identify appropriate criteria for defining and evaluating the resolution of overlapping TL peaks.

For resolving a composite glow curve into its components, some approximated functions have been proposed, including the Podgorsak-Moran-Cameron approximation (PMC), Gaussian peak shape, asymmetric Gaussian functions, and others reviewed by Horowitz and Yossian [31].

The PMC approximation is the only one which transforms the aforementioned parameters into: I_m, E, T_m, T [32]. The benefit of this transformation is having only two free parameters I_m and T_m, which can be obtained directly from the experimental glow curve.
Using Eq. (I.15) of the general-order kinetics and the following approximation:

$$\int_{T_0}^{T} exp\left(-\frac{E}{kT'}\right) dT' = \frac{kT^2}{E}\left(1-\frac{2kT}{E}\right) exp\left(-\frac{E}{kT}\right) \tag{I.28}$$

The condition at maximum is:

$$\frac{\beta E}{kT_m^2} = Z_m s.\, exp\left(-\frac{E}{kT_m^2}\right) \tag{I.29}$$

Kitis proposed for general-order kinetics new analytical expression for describing a glow peak that have the same accuracy as the basic TL kinetic equation of the general-order kinetics while retaining the advantage of the PMC equation as [12, 33]:

$$I(T) = I_m.\, b^{\frac{b}{b-1}}.\, exp\left(\frac{E}{kT}.\frac{T-T_m}{T_m}\right) \times \left[(b-1).(1-\Delta).\frac{T^2}{T_m^2}.\, exp\left(\frac{E}{kT}.\frac{T-T_m}{T_m} + Z_m\right)\right]^{-\frac{b}{b-1}} \tag{I.30}$$

where

$$\Delta = \frac{2kT}{E},\ Z_m = 1 + (b-1).\Delta_m,\ \Delta_m = \frac{2kT_m}{E}$$

I.4 Optically stimulated luminescence (OSL)

OSL is the light emitted by certain crystals that have previously been exposed to ionizing radiation when they are stimulated by light (visible or infrared). OSL emission from natural

crystals is not entirely understood since it is dependent on the nature and concentration of impurities, as well as the crystal's defects. Because each mineral might have a distinct OSL response, even aliquots of the same sample must be calibrated separately [34].

Since the 1950s, OSL was proposed as a dosimetry tool for the first time by Romanovskiĭ et al, [35] when working with different sulfide materials, it was noted that when they were exposed to infrared light, they emitted a luminescence [36].

I.4.1 Theory of OSL

The situation of OSL is the same as TL phenomenon. During OSL readout by photons, such as infrared (IR) light, electrons raise from the trap to the conduction band, where they find counterpart holes in the center and recombine to generate OSL photons. Figure I.12 depicts the energy levels of OSL phenomenon in a simple representational view [14, 15].

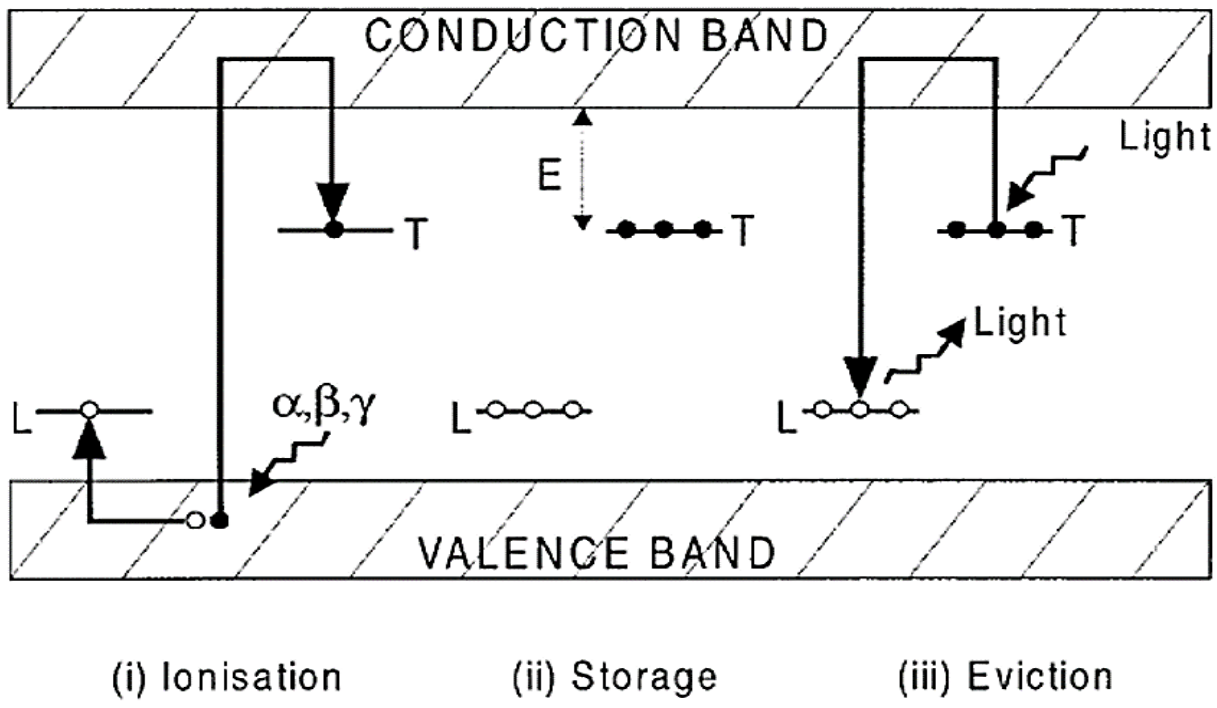

Figure I. 12. Energy level presentation for optically stimulated luminescence [16].

The electrons are evicted from electron traps by shining light (blue, red,...).

Many types of traps exist within the crystal as shallow-depth traps that are unstable at room temperature, medium-depth traps can be released when exposed to visible light, and deep-depth traps that are extremely difficult, if not impossible, to empty once filled. The behavior

and interplay of these various trap types have an impact on the fading, reuse, and readout of dosimeters [37].

I.4.2 OSL stimulation modalities

Unlike TL, OSL has several experimental approaches of stimulation:

I.4.2.1 ‘‘Continuous-wave OSL’’ (CW-OSL) in which the stimulation light intensity is constant and the signal of OSL is monitored continuously throughout the stimulation period [38]. In this case, the only distinction between OSL and stimulation light is based on wavelength separation ($\lambda_{OSL} \neq \lambda_{stim}$). Figure I.13 presents CW-OSL stimulation with its corresponding decay curve.

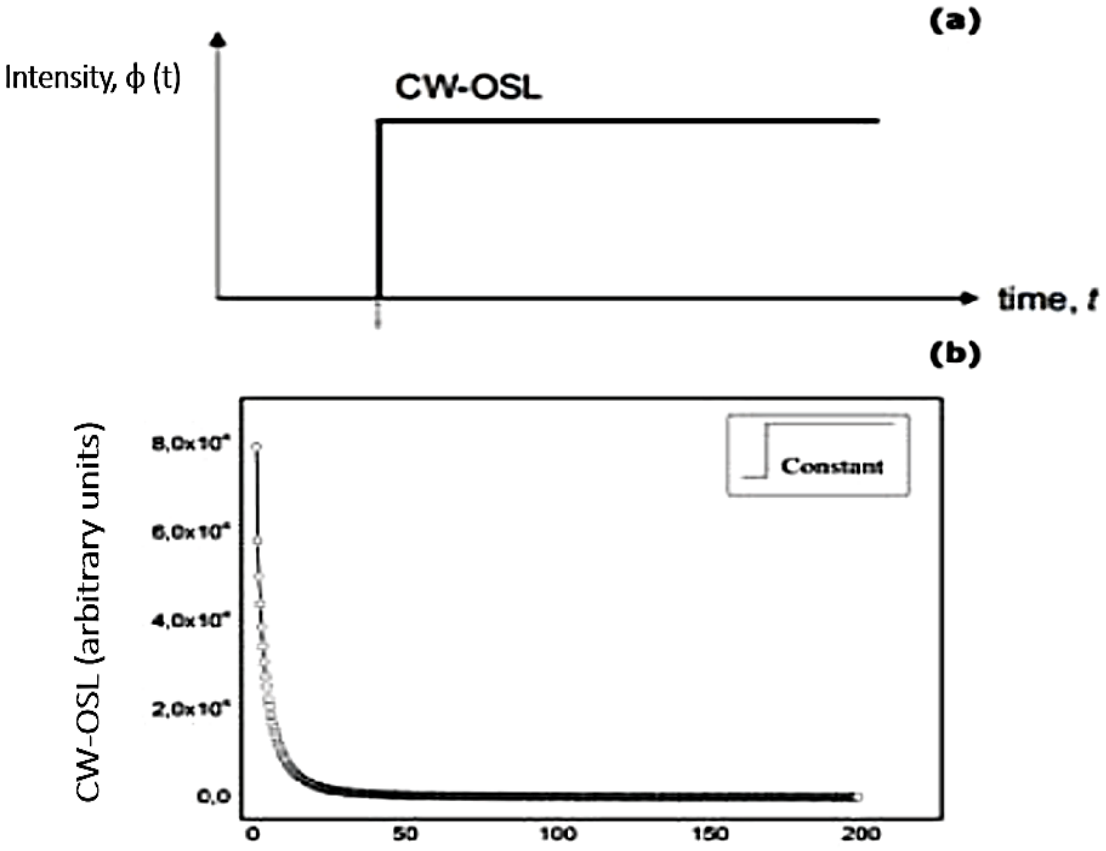

Figure I. 13. (a) CW-OSL stimulation mode, (b) its typical decay curve [40].

Due to its simplicity and frequently satisfactory performance, CW-OSL is the most widely used stimulation method in dosimetry and luminescence dating [39].

I.4.2.2 ‘‘Linear-modulation OSL’’ (LM-OSL) method in which the stimulation intensity is ramped linearly during measurements [41]. In this technique, the OSL curves are observed in form of peaks showed in Figure I.14. The position of peaks depends on the rate of linear ramping in intensity of the stimulation light and the photoionization cross-section of the trap being emptied. The component with the largest cross-section value appears first, just as the 'fast' component in CW-OSL. The intensity peaks observed in linearly modulated optically stimulated luminescence (LM-OSL) are synonymous with, but not necessarily identical to, the CW-OSL ‘fast’, ‘medium’, and ‘slow’components [38].

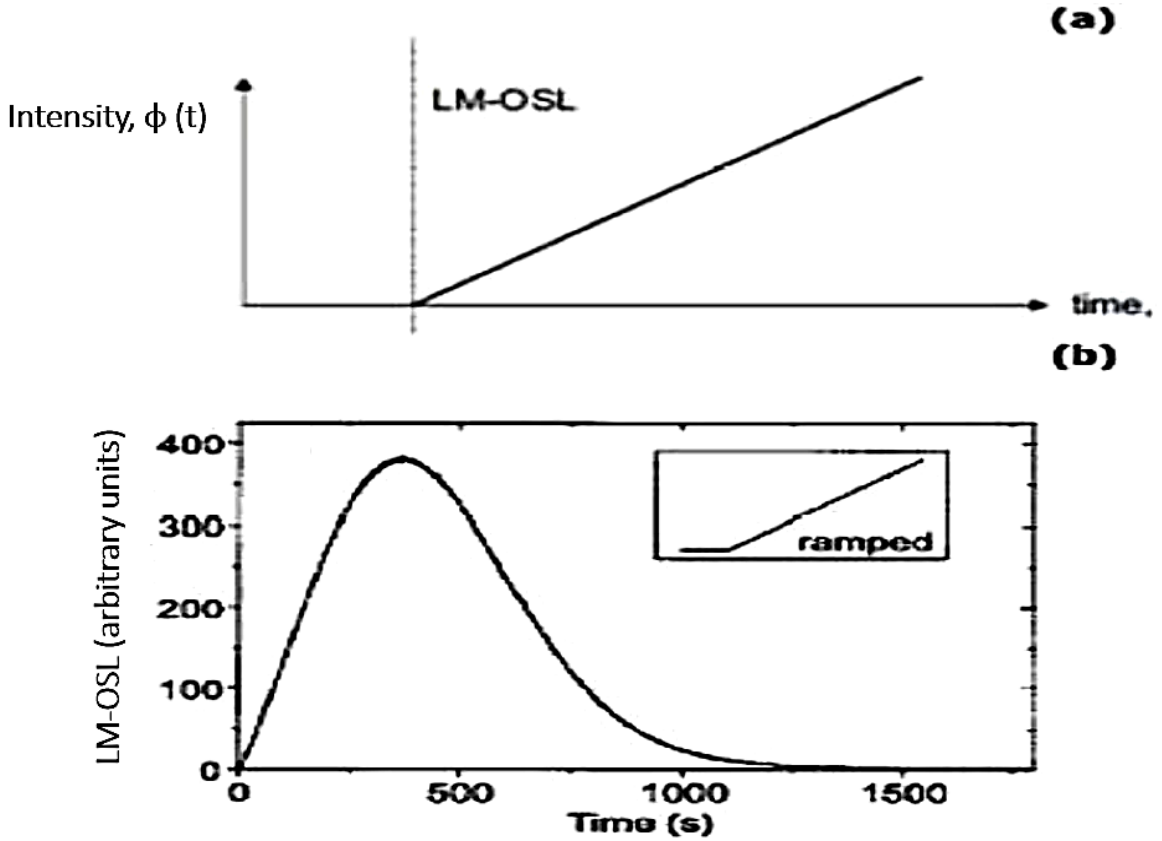

Figure I. 14. (a) LM-OSL stimulation mode, (b) its typical signal [40].

I.4.2.3 ‘‘Pulsed OSL’’ (POSL), a pulsed light source is used and the signal of OSL is monitored only between pulses, as depicts Figure I.15. Since emitted luminescence is measured when the stimulation light is turned off, the need of optical filters to distinguish between emission and stimulation light is reduced. POSL distinguishes between emission and stimulation light using time resolution rather than wavelength resolution as in CW-OSL and LM-OSL [39].

The intensity of optical stimulation is separated in two parts: emission during the excitation pulse and emission following the excitation pulse. The efficiency of the POSL

process is reflected by the ratio of luminescence emitted after and during the pulse. In POSL stimulation mode, just the OSL emission between pulses is detected. The POSL approach is highly sensitive to the material's luminescence lifetime [39].

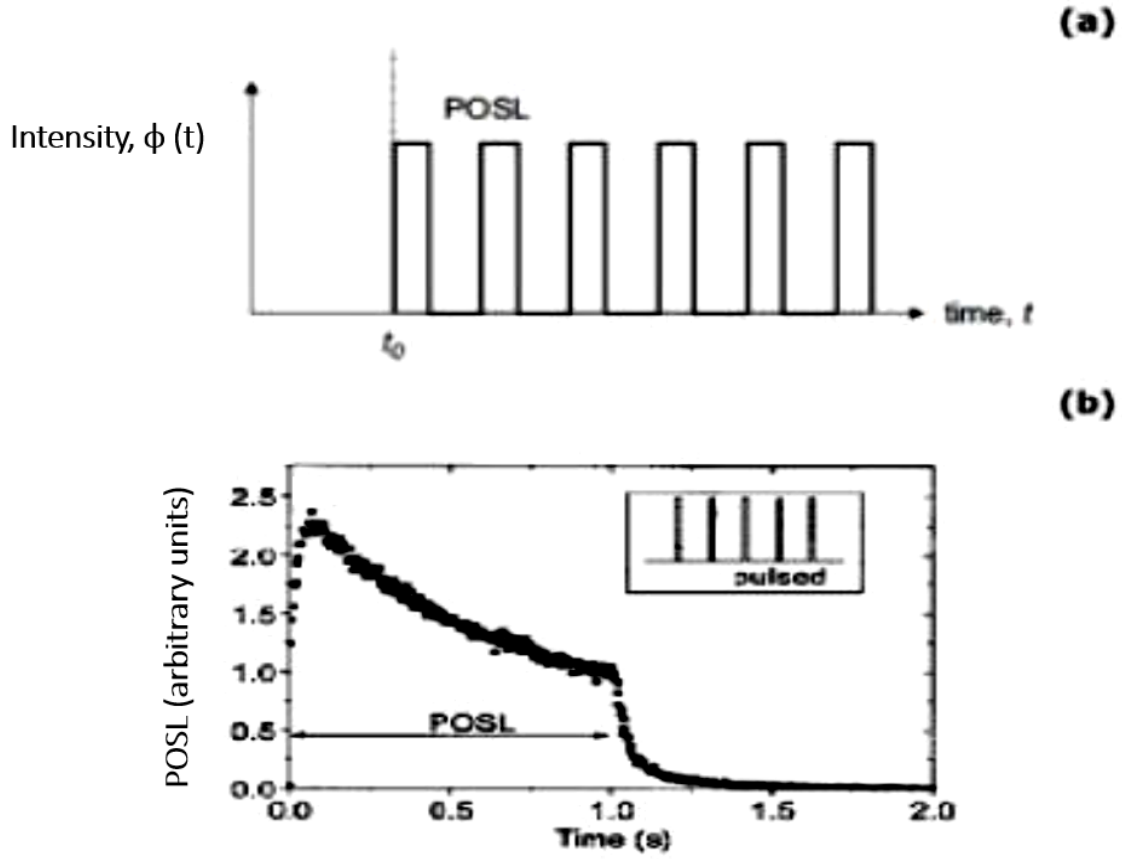

Figure I. 15. (a) POSL stimulation mode, (b) its typical signal [40].

I.4.3 Equations governing the OSL processes

I.4.3.1 CW-OSL governing equations

A series of non-linear, coupled rate equations can be used to represent charge transitions between energy levels during irradiation and subsequent optical stimulation of a dosimeter. To arrive at analytical expressions, several simplifying assumptions for the evolution of the OSL intensity with time during optical stimulation and, ultimately, the dependence of the OSL signal on the absorbed dose must be introduced.

The most basic corresponds to a system with one type of electron trap and one type of hole trap. This is known as the one-trap/one-recombination model. Additional complexities can be introduced gradually to gain an understanding of the role of additional electron traps and/or recombination centers.

I.4.3.1.1 The idealized one-trap/one-recombination OTOR model

Figure I.16 depicts the simplest mathematical model for CW-OSL, which consists of one electron trap *T* and one recombination center *R*.

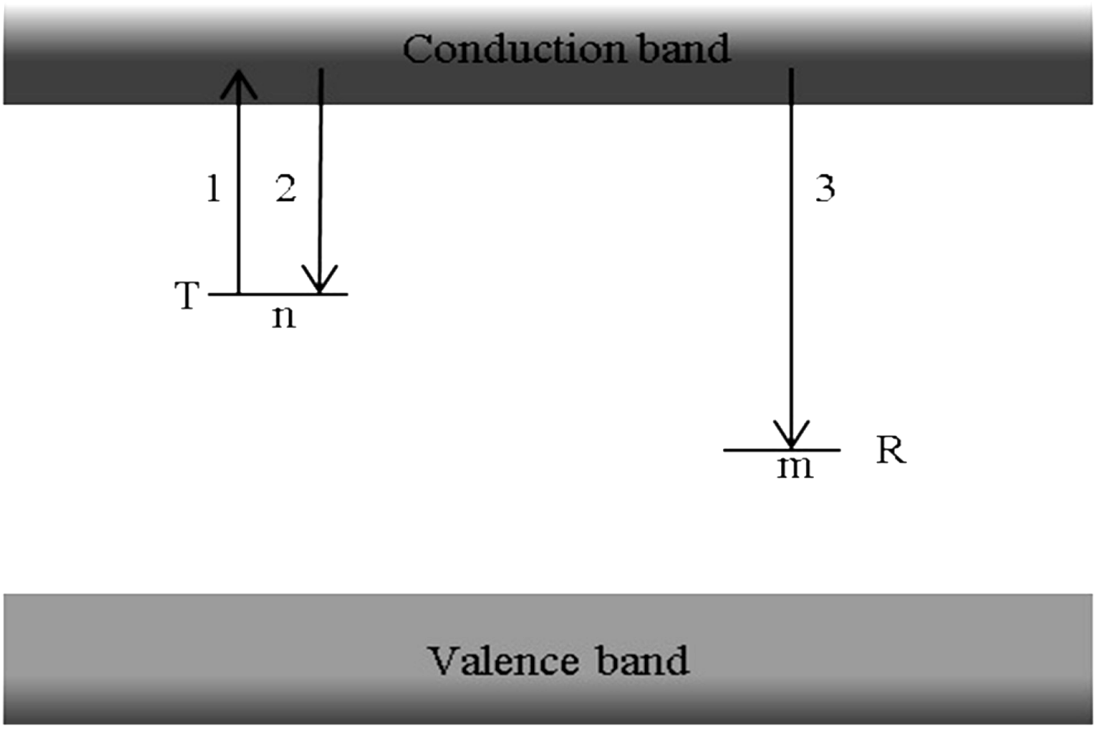

Figure I. 16. A simple one-trap/one-recombination center model. Transitions 1, 2 and 3 stand for optical stimulation, retrapping and recombination, respectively [42].

When a sample is exposed to light, electrons are stimulated from the electron trap at a rate p given by:

$$p = \Phi\sigma \tag{I.31}$$

where

Φ is the stimulating light intensity

σ is the photoionisation cross section.

Transitions to the valence band do not occur during optical stimulation of the electrons from the traps, and at any time *t* during the optical stimulation period, the charge neutrality condition becomes $n_c + n = m$, from which the rate of change of the various concentrations can be written as:

$$\frac{dn_c}{dt} = -\frac{dn}{dt} + \frac{dm}{dt}$$

Optically stimulated electrons from an electron trap to the conduction band (transition 1 in the above figure) can be retrapped (transition 2) or proceed to the recombination center, where they produce luminescence (transition 3). The rate equations that describe these processes are expressed as Eq. (I.2) and (I.3). At this point, the so-called quasi-equilibrium assumption is introduced, namely

$$\left|\frac{dn_c}{dt}\right| \ll \left|\frac{dn}{dt}\right|, \left|\frac{dm}{dt}\right| \tag{I.32}$$

This approximation, which states that the concentration of free electrons in the conduction band n_c must be stable, is used to make rate equations such as Eq.(I.2) tractable.

Under the assumption of negligible retrapping and $n_c \ll n, m$, the intensity of the emitted OSL is given by:

$$I_{OSL} = -\frac{dn}{dt} = np \tag{I.33}$$

First-order kinetics is described by Eq. (I.33), in which the rate of trap emptying is proportional to the concentration of trapped electrons. We can deduce from Eq.(I.33) that the time-dependence of luminescence intensity is:

$$I_{CW-OSL}(t) = n_0 p\, exp(-pt) = I_0\, exp(-pt) = I_0 \exp(-\frac{t}{\tau_d}) \tag{I.34}$$

where τ_d is a constant of CW-OSL decay.

As a result, when a constant stimulation light intensity is applied to the sample, the OSL intensity decays exponentially. Eventually, all of the traps are depleted, and the OSL drops to zero.

Non first-order decay may result from retrapping, trap interactions, and multiple centers of recombination [42].

I.4.3.1.2 Multiple traps and centers model

A non-exponential OSL decay can be observed which was interpreted in terms of contributions from three distinct traps with various photoionization cross sections at used stimulation wavelengths. Later, the obtained data were interpreted by fitting the decay curves to three exponential decay curves sum with varying values for the constant of OSL decay referred to as the ‘fast’, ‘medium’ and ‘slow’ components. Figure I.17 represents the OSL decay curve from quartz with two components: slow and medium, representing two types of optically sensitive traps.

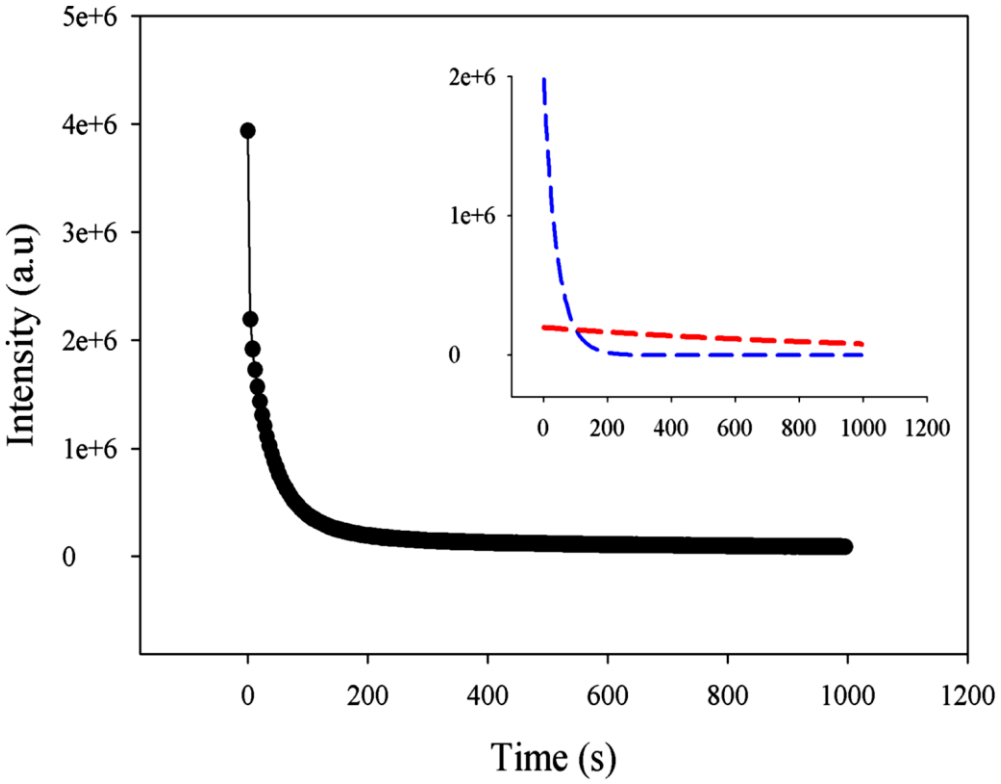

Figure I. 17. A quartz OSL decay curve with the slow component (blue) and the medium component (red) [42].

In the case of two optically sensitive traps with concentrations of trapped charge n_1 and n_2 and stimulation rates p_1 and p_2, it is easy to show that:

$$\frac{dm}{dt} = -\left(\frac{dn_1}{dt} + \frac{dn_2}{dt}\right) \tag{I.36}$$

and

$$\begin{aligned} I_{OSL} &= n_{10}p_1.exp(-tp_1) + n_{20}p_2.exp(-tp_2) \\ &= I_{10}.\exp(-t/\tau_{d1}) + I_{20}.exp(-t/\tau_{d2}) \end{aligned} \tag{I.37}$$

Employing the superposition principle with no trap interaction, it is obvious that this can be expanded to three or more optically sensitive traps, each of which empty during stimulation at a different characteristic rate.

I.4.3.1.3 Generalized model

Real materials have multiple traps and centers, some of which are shallow, some of which are "optically sensitive" (i.e., the charge can be optically stimulated at the wavelength

used from the trap), and some of which are deep. Some recombination centers are radiative, while others are not. Effects of charge transfer may occur between some centers but not others. Charge transfer processes may or may not involve the conduction band (as previously assumed). Real materials, in other words exhibit far greater complexity of behavior than has been suggested so far.

McKeever et al., presented the model shown in Figure I.18 as a first attempt to develop a realistic OSL model. The model consists of: shallow trap (1) where electrons can be trapped during optical stimulation (arrow pointing downward) and can be optically or thermally released (arrow pointing upward); dosimetry trap (2) where electrons are stimulated optically; deep trap (3) where electrons can be trapped that remain localized once trapped; radiative recombination center (4) where trapped electrons and holes can recombine and produce OSL; and non-radiative recombination center (5) in which recombination can take place without generating an OSL photon.

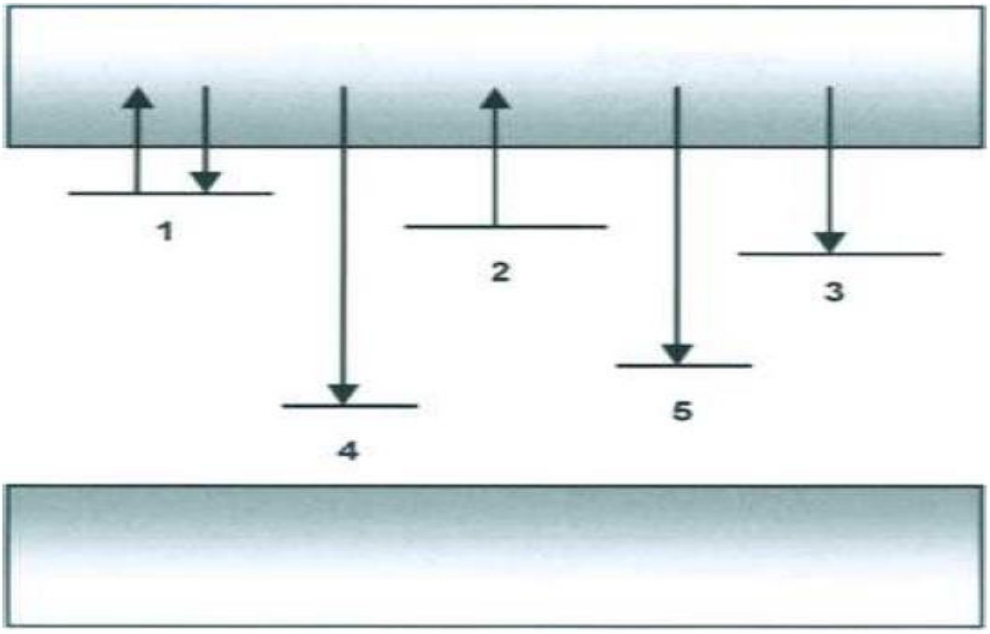

Figure I. 18. A model that combines all of the elements shown separately in Fig. I.16 [43].

It should be noted that the single shallow trap indicated here can be thought of as representing all of the shallow unstable traps that are expected to be found in real materials, each with its own lifetime of trapped charges and characterized thermal decay. The same applies to both types of recombination centers. Similarly, deep traps can be thought of as all deep traps that can capture charge during optical stimulation and thus competing luminescence centers.

As a result, while the model described is simplistic, it includes many of the characteristics that might be found in a real material.

Six coupled, non-linear equations make up the rate equations that describe the charge flow into and out of the different traps and centers shown above. These equations are unsolvable, even for this still oversimplified model. The rate equations must be numerically solved under a variety of conditions in order to acquire further understanding of the potential behavior of such a system. At this point, the parameter range is open-ended, meaning that an endless number of values and value combinations are possible.

To determine the number of traps and recombination centers required and to limit the range of possible values for the trapping and recombination parameters, one would need to carefully examine the available experimental data if one were attempting to simulate a specific material. Yet for now, only intelligent guesses must be made. Even still, this admittedly inadequate approach provides insights into possible experimental results obtained with a real material. Bøtter-Jensen et al. (1994) and McKeever et al. (1997) used a similar procedure to study how the shape of the OSL decay curve changes with delivered dose, intensity of stimulation, pre-irradiation annealing procedure, and temperature. Temperature-dependent effects on OSL curve shapes can be noticed when measuring at different temperatures. Perhaps the most widely recognized result is genetically known as "thermal assistance," which is reflected by the observation that more OSL is stimulated for the same excitation intensity at higher temperatures than at lower temperatures. Shallow traps can generate this observation, but thermal assistance has an important feature in that it increases not only OSL efficiency but also the rate of OSL decay during CW-OSL measurement. [43]. In these instances, the CW-OSL decay rate, $p = 1/\tau_d$ is temperature-dependent:

$$p = p_0 . exp\left\{-\frac{\Delta E}{kT}\right\} \tag{I.38}$$

where, ΔE is the thermal activation energy.

I.4.3.2 LM-OSL governing equations

I.4.3.2.1 First and general-order kinetics

So far, the description of OSL has been based on CW-OSL, or OSL induced by a constant intensity of a light source with a constant wavelength. An alternate approach was proposed in which the stimulation source intensity is linearly ramped and the OSL is measured during the ramp. When this stimulation mode is adopted, the OSL is observed as peak series, each of which corresponds to charge release optically from various trap types. Thus, traps with a large photoionization cross-section at the wavelength utilized during measurements are the

first to empty and appear as a peak an OSL plot vs stimulation time. Smaller photoionization cross-section traps take longer time to empty, giving rise to OSL peaks that manifest later. As a result, LM-OSL may provide better discrimination of traps with different rates of de-trapping, such as those that are fast, slow, or medium, when compared to CW-OSL.

The shape of LM-OSL curves can be mathematically described considering the one-trap/one-recombination model. In this model, the electrons are trapped in a localized state until being stimulated into the conduction band by photon absorption of energy $h\nu_{ex}$. The liberated electron can then recombine at a trapped hole center to emit photon of wavelength $h\nu_{em}$.

For first-order kinetics where the retrapping is negligible, the de-trapping rate is provided by Eq. (I.31), and the intensity of corresponding luminescence (CW-OSL) by Eq. (I.34), where the decay time-constant is $\tau_d = 1/\sigma\Phi$. However, if the intensity ramps linearly from 0 to a maximum value Φ_m as follows:

$$\Phi(t) = \gamma t \tag{I.39}$$

Then Eq. (I.33) is now replaced by:

$$\frac{dn}{dt} = -\sigma\gamma t n \tag{I.40}$$

From which a Gaussian function is obtained:

$$n = n_0 exp\left(-\frac{\sigma\gamma}{2}t^2\right) \tag{I.41}$$

The LM-OSL intensity can be given by:

$$I_{OSL} = n_0\sigma\gamma t.\, exp\left(-\frac{\sigma\gamma}{2}t^2\right) \tag{I.42}$$

Because the concept of superposition is applied to first-order kinetics, and if K traps of type i exist, the equation is rewritten as follows:

$$I_{OSL} = \gamma t \sum_{i=1}^{K} n_{0i}\sigma_i.\, exp\left(-\frac{\gamma\sigma_i}{2}t^2\right) \tag{I.43}$$

The sample's experimental curve of LM-OSL in which several traps are simultaneously emptying but at different rates may be described as a sum of LM-OSL first-order curves. Figure I.19 shows example LM-OSL curves simulated for various product values γσ for fixed values of n_0.

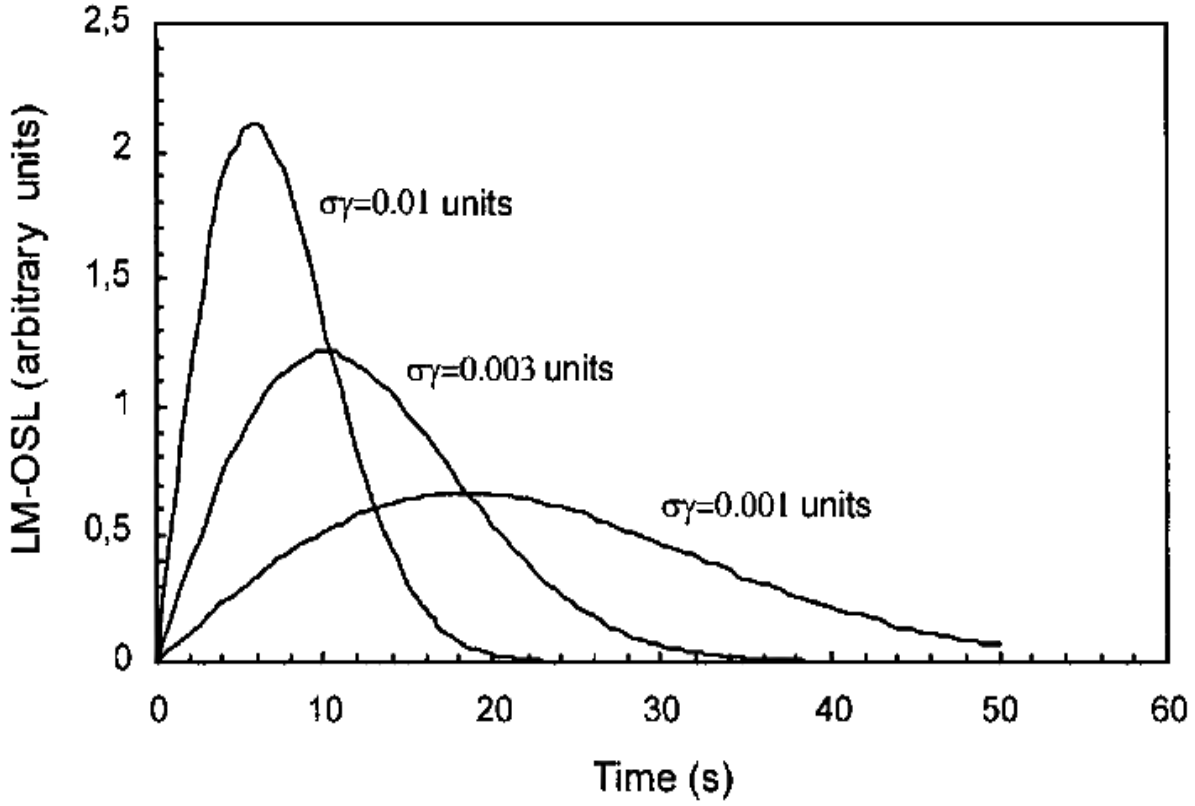

Figure I. 19. LM-OSL curves for 1st order kinetics simulated using various product values γσ [43].

The LM-OSL peaks arise at shorter durations as the photoionisation cross-section σ rises for constant ramp rates γ. Similarly, with fixed σ, the peaks arise at shorter durations for increasing ramp rate. At t = 0, all peaks begin. For a system with first-order kinetics and multiple peaks, the net LM-OSL curve is simply the addition of peaks as those shown [43].

It should be noticed that regardless of the σ and γ values used, each peak begins at t=0. For a single trap, the LM-OSL curve has the shape of a linearly increasing function (proportionally to the linear increase in the power of stimulation) with a Gaussian decrease in the intensity of LM-OSL intensity as the trap is depleted. The time for reaching the maximum is given by the following formula:

$$t_{max} = \sqrt{\frac{1}{\sigma\gamma}} \tag{I.44}$$

and the maximal intensity of the LM-OSL is :

$$I_{OSL}^{max} = \frac{n_0}{t_{max}} . exp\left(-\frac{1}{2}\right) \tag{I.45}$$

Thus, based on the γ known value and the t_{max} observed value, the ionisation cross-section at the experimental wavelength used can be determined. The LM-OSL peak position is also seen to be wavelength dependent (by the wavelength dependence of σ) and linear modulation ramp rate γ dependent. When a general-order kinetics model is adopted, in which the re-trapping rate of the released charge is greater than the recombination rate, it yields:

$$\frac{dn}{dt} = -\frac{\sigma\gamma t n^b}{n_0^{b-1}} \tag{I.46}$$

where b is a dimensionless positive number: $b > 0,\ b \neq 1$. The solution of Eq. (I.46) is as follows:

$$I_{OSL} = n_0\sigma\gamma t\left[(b-1)\frac{\sigma\gamma t^2}{2} + 1\right]^{b/(1-b)} \tag{I.47}$$

Contrary to the first-order kinetics case, the superposition does not apply when many types of traps exist, therefore an experimental curve of LM-OSL cannot be easily characterized as the sum of various non first-order processes. A general-ordered LM-OSL peak reaches its maximum at time t_{max}, where:

$$t_{max} = \sqrt{\frac{2}{\sigma\gamma(b+1)}} \tag{I.48}$$

where the maximum intensity is:

$$I_{OSL}^{max} = \left(\frac{2n_0}{b+1}\right)\left(\frac{1}{t_{max}}\right)\left(\frac{2b}{b+1}\right)^{b/(1-b)} \tag{I.49}$$

The luminescence intensity is considered to be directly proportional to the rate of de-trapping, dn/dt, in the descriptions of the first-order LM-OSL and CW-OSL curves. These results reveal that the rate of de-trapping is directly related to the stimulation intensity. Thus, with $p = \sigma\Phi$ and from Eq. (I.34) we can see that $[d\ln(I_{CW-OSL})/dt] \propto \Phi$.

A mathematical transformation was provided by Bulur, that converts CW-OSL curves to LM-OSL curves. First, declare a variable u as follows:

$$u = \sqrt{2tP} \tag{I.50}$$

where P is the LM-OSL total measurement period in experiments, and u is the time dimension. The result of multiplying by u/P and substituting Eq. (I.42) into the expression of CW-OSL (Eq. (I.34)) is as follows:

$$I_{OSL} = \frac{n_0 \sigma \Phi u}{P} exp\left(-\frac{\sigma \Phi}{2P} u^2\right) \quad \text{(I.51)}$$

This has the same form as the LM-OSL expression (Eq. (I.42)). Comparing the expressions (I.34) and (I.51) we see that u agrees with t , and clearly $\Phi/P = \gamma$.

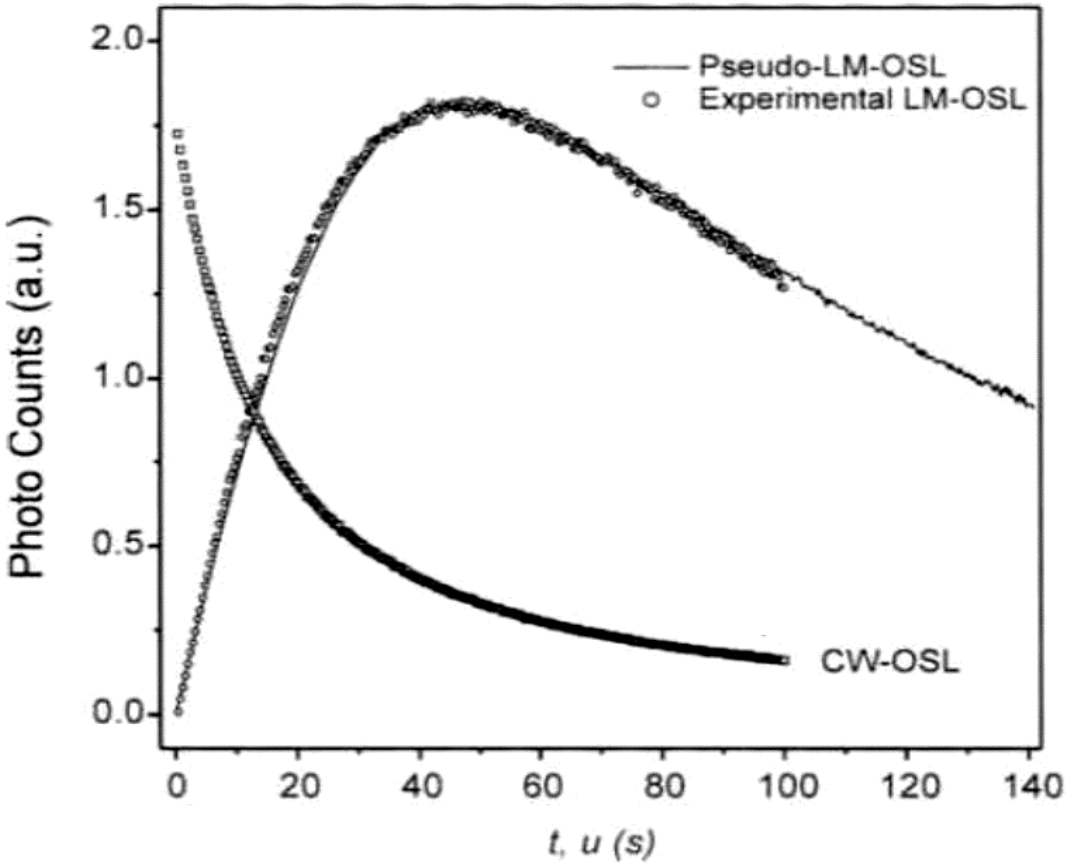

Figure I. 20. Na-feldspar CW-OSL, pseudo LM-OSL, and experimental LM-OSL curves produced using IR-stimulation [43].

Figure I.20 shows an example of a CW-OSL curve, the transformed (pseudo), and experimental LM-OSL curves from IR-stimulated Na-feldspar, using a ramp time of 100 *s* in the experiments and in the calculation of transformation using Eq. (I.49) [43].

I.4.4 CW & LM-OSL advanced methods in trapping parameters evaluation

I.4.4.1 Differential Evolution (DE) algorithm to OSL decay curves deconvolution

Bluszcz and Adamiec present a differential evolution algorithm (DE) and its application to OSL decay curve deconvolution to first-order components. Their basic assumption is that under stimulation of constant intensity, quartz OSL intensity is provided by the sum exponential decay components as:

$$I(t) = I_{01}.exp^{-\lambda_1 t} + I_{02}.exp^{-\lambda_2 t} + \cdots \quad \text{(I.52)}$$

where the aim is the determination of the components number *m*, also the value estimation of both, the decay constants λ_k, and the magnitude I_{0k} of each component. The CW- and LM-OSL decay curves can be measured. The LM-OSL curve is represented as:

$$I(t) = I'_{01}t.exp^{-(1/2)\gamma_1 t^2} + I'_{02}t.exp^{-(1/2)\gamma_2 t^2} + \cdots \quad \text{(I.53)}$$

Since the two results present the same object under different conditions of stimulation, there should be some correlation between the parameters associated with each component. As Bluszcz and Adamiec point out, OSL intensities are commonly measured indirectly by counting luminescence photons over intervals of finite time, i.e. in those intervals, the integrals of Eq. (I.52) or (I.53) are recorded. The counting time interval can be of constant length or can vary from the shortest (beginning of the OSL decay) to the longest (end of the OSL decay), this choice allows optimizing the OSL curve resolution when the counting intervals total number is limited. For mathematical simplicity in LM-OSL case, it was assumed that all periods of counting were of equal length τ, and that the measurements data consisted of N numbers that were photon counts collected within the interval of $(0,N_\tau)$ in N equal periods. It is also assumed that the experimental data did not include any background counts for similar reasons. In practical situations, the background can be taken into account by subtracting it from experimental data prior to analysis or by the add of a linear component (permitting a constant or a linearly increasing in CW-OSL or LM–OSL cases, respectively). Of course, a good knowledge of the instrument background is always recommended. The CW-OSL and LM-OSL have in this case the following forms, respectively:

$$I_i = \sum_{k=1}^{m} a_k\left(e^{\lambda_k \tau} - 1\right)e^{-\lambda_k \tau_i},\ i = 1,2,\dots,N \quad \text{(I.54)}$$

and

$$I_i = \sum_{k=1}^{m} b_k \left(e^{\gamma_k \tau^{2(i-1)}} - 1\right) e^{-\frac{1}{2}\gamma_k \tau^2 (i-2)i},\ i = 1,2,\dots,N \quad \text{(I.55)}$$

Although the two models have quite different shapes, they are both $(\lambda_k\ , a_k)_m$ and $(\gamma_k\ , b_k)_m$ parameters dependent in the same way, i.e. they are linear combinations of exponential terms. Despite having more complex forms, general models with various lengths of counting intervals and stimulation steps still rely on their parameters in a same way. For this reason, simpler model provided by Eq. (I.54) was discussed while retaining the proposed

approach generality. The models' reliance on a_k (or b_k) parameters is linear, whereas λ_k (or γ_k) parameters is nonlinear. This feature was considered while optimizing a fitting strategy. Thus, the assumption that the problem is to find automatically components number statistically justified m, along with the parameter's best two sets (λ_k) and (a_k) was adapted using the weighted least squares (LS) method to fit N values seriesn_i, which represent the number of measured OSL photons. Further, photon number having Poisson variances was assumed, i.e. For the i^{th} interval with n_i counts number, the weight is equal to τ^2/n_i.

$$\chi^2 = \sum_{i=1}^{N} \frac{\tau^2}{n_i} \left(\frac{n_i}{\tau} - \sum_{k=1}^{m} a_k (e^{\lambda_k \tau} - 1) e^{-\lambda_k \tau_i} \right)^2 \quad \text{(I.56)}$$

The χ^2 value has been minimised for the $2m$ parameters (λ_k) and(a_k). The chi-square distribution of this minimised value has $\nu = N - 2m$ freedom degrees. A component adding (a fixed or adjustable linear component of background in the model that simply increases the linear parameters number and decreases the freedom degree number of the χ^2 value) to the fitted model reduces the χ^2 value by $\Delta\chi^2$ and its freedom degree number by 2. As a result, the new value of χ^2 has $N - 2m - 2$ freedom degrees whereas the $\Delta\chi^2$difference has 2 freedom degrees. The justifiability of $m + 1^{th}$ component adding is tested using the ratio F:

$$F = \frac{\Delta\chi^2/2}{\chi^2/(N-2m-2)} \quad \text{(I.57)}$$

If the determined F-value is higher than F_α critical value for a level of given significance α (such as 0.05 or 0.01), then the newly added component can remain in the model. If not, we need to revert to the previous component with the m component. This criterion allows us to select the components number that the experimental data justifies. This procedure is simply automated using a computer program. The following steps may be included in the proposed algorithm.

1. Set the number of components m to 1 and try to minimise the $\chi^2(m)$ value.
2. Increase m by 1 and try to minimise the $\chi^2(m+1)$ value.
3. Use Eq. (I.56) to $\Delta\chi^2 = \chi^2(m) - \chi^2(m+1)$ and Fstatistics calculation.
4. If $F > F_\alpha$, go to step 2 otherwise.
5. Get back to the component m and stop. Output the optimal λ_k and a_k values as well as other statistics.

Because of the model's exponential dependency on λ_k parameters, minimizing the χ^2value necessitates an iterative method for non-linear regression, which have common

weakness. In order to reach the minimum, these methods require a point of starting in a parameter space. Frequently, the nearest local minimum is settled rather than the desired global one. When the procedure of minimization is not carried out frequently, this weakness kind can be tolerated, nd the user can fix it by choosing a better point of starting. When there is a big experimental data number to be evaluated and the procedure is time demanding, human intervention is impractical or perhaps technically infeasible.

A starting point can be found for the Levenberg–Marquardt (LM) minimization method using self-organising algorithms for optimization differential evolution (DE) based. The differential evolution method examines a parameter space stochastically for a quasi-optimal solution, in this instance, the χ^2 global minimum. In a parameter space of n-dimensions, the solution is represented as a vector, where n is a number of χ^2 parameters and the parameter values make up the vector's coordinates. In the most basic situation, the ith coordinate of the vector solution is the ith parameter. DE begins with a random selection of NP vectors V_i ($i = 1, 2, 3, \ldots, NP$) from the given search space. "Generation" refers to the collection of NP vectors. This generation develops into generations of descendants by three main evolutionary operations that are mutation, combination and finally selection. The operation of mutation involves adding a weighted difference of 2 additional vectors chosen at random from the current generation to a given vector. Let $\boldsymbol{A}$ be a mutating vector, $\boldsymbol{B}$ and $\boldsymbol{C}$ be two randomly chosen vectors such that:

$$\boldsymbol{A} \neq \boldsymbol{B} \neq \boldsymbol{C} \tag{I.58}$$

Following which the mutated vector is obtained as

$$\boldsymbol{A'} = \boldsymbol{A} + F.(\boldsymbol{B} - \boldsymbol{C}) \tag{I.59}$$

where F is a factor of weighting that governs the mutation scale.

When there is a combination between vectors $\boldsymbol{A}$ and $\boldsymbol{B}$, a subvector C inherits a randomly chosen coordinate from vector $\boldsymbol{B}$ and each of its remaining $n - 1$ coordinates from either $\boldsymbol{A}$ with $(1 - CR)$ probability or from $\boldsymbol{B}$ with a CR probability. The operation of combination is denoted as:

$$\boldsymbol{C} = R(\boldsymbol{A}, \boldsymbol{B}; CR) \tag{I.60}$$

Since the descendant generation's composition is determined by NP competition, in the ith competition the ith vector competes with its subvector V_i, which is the product of the mutation and the combination of the three vectors chosen at random,

$$\boldsymbol{V_i'} = R[\boldsymbol{V_i}, \boldsymbol{V_a} + F.(\boldsymbol{V_b} - \boldsymbol{V_c}); CR] \quad \text{(I.61)}$$

The vector with the lower 2 value among the two competing vectors $\boldsymbol{V_i'}$ and $\boldsymbol{V_i}$ is chosen for the next generation. The DE algorithm invokes an external function for each vector $\boldsymbol{V}$ that returns the value of χ^2 calculated for the fitting experimental data. When the generation completes, the DE algorithm then invokes some other external function to check for the "stop" condition. Three parameters : NP, F and CR, which represent the vector number in the developing population, the mutation scale and the crossover rate (probability), respectively, control the DE in this manner, where NP is recommended to be $5-10$ times the parameter number n, $0 < F \leq 1.2$ and $0 \leq CR \leq 1{,}0$.

Since the models depend on linear and non-linear parameters where the linear portion may be addressed using linear regression techniques, while the non-linear portion can be approximated using DE first before being solved using a non-linear LM regression technique. The solution vector is divided into two parts practically. The first is made up of m decay constants λ_k and is referred to as Λ, while the second is made up of the remaining parameters a_k (background parameters are included where appropriate) and is referred to as A. A hybrid algorithm that employs an evolutionary approach to optimize both vector Λ and linear regression to generate A vector is used to minimiseχ^2. A linear regression calculation of the vector A coordinates is performed within a function that returns the value χ^2. The proposed algorithm is known as HELA, which stands for hybrid evolutionary-linear algorithm. The HELA suggested for the OSL curve's automated and unassisted deconvolution into m components may be expressed as follows:

1. Set a range of variability for the m decay constants, which are the Λ vector coordinates. Then, generate at random NP such Λ_i vectors ($i = 1, 2, 3, \ldots, NP$) to create the initial generation of solutions. Call an external function for each i that returns both χ^2 value and the vector Λ_i whose coordinates are calculated via linear regression.
2. Use evolutionary operators, to get the following generation of the solution. To get the χ^2 value for each vector, use Eq. (I.60) to create an offspring Λ_i' for each vector Λ_i through mutation and crossing-over. From competing pairs Λ_i and Λ_i', choose the one with the lower value of χ^2 for the following generation.

3. Check out the "stop" condition and output the best possible solution. If the condition is not satisfied, appoint the new incumbent generation and move to step 2.
4. use the best possible solution from step 3 as a starting point for the method LM to get the m OSL components parameters.

Randomly generated data containing components of known intensity and decay constant and additional background were tested. In most situations, 15-100 generations were required to achieve satisfactory adaptation. The LM method did not yield better values of χ^2 than the HELA algorithm, in many cases. The HELA method has proven to be highly effective in simulated OSL decay curve decomposition into its components. As a result, the known parameters were successfully retrieved. In practice, the evaluated parameters may be used to estimate the absorbed dose for various components [44].

I.4.4.2 Deconvolution

GCD procedure for TL have recently been used to peak-shaped composite curves of LM-OSL. Kitis and Pagonis investigated the geometrical properties and symmetry factors of peak-shaped curves of LM-OSL, highlighting the differences and similarities between the deconvolution analyses of TL and OSL. These researchers investigated both first- and general-order peaks and revealed the presence of pseudo constants that vary slowly and there use to develop formulas for optical cross-sections for OSL. For first- and general-order analysis, the following expressions were developed in a manner similar to that of TL.

$$I(t) = 1.6487 I_m \frac{t}{t_m} . exp\left(-\frac{t^2}{t_m^2}\right) \tag{I.62}$$

$$I(t) = I_m \frac{t}{t_m} \left(\frac{b-1}{2b}\frac{t^2}{2t_m^2} + \frac{b+1}{2b}\right)^{b/(1-b)} \tag{I.63}$$

In these formulations, t_m represents the time at which the maximum intensity of LM-OSL occurs. Kitis and Pagonis pointed out a significant distinction between TL and OSL deconvolution study. Once the time t_m of LM-OSL's maximum intensity I_m in the experimental OSL curve has been determined, the whole individual OSL curve may be recognized within the composite curve of LM-OSL. This property is essential for computerized curve deconvolution analysis (CCDA), since for any given t_m, there is only one corresponding peak of LM-OSL, contrary to the respective TL peaks property, where each peak's T_m corresponds to unlimited number of possible peaks of TL with various kinetic parameters pairs (E, s) [3].

CHAPTER II

TL & OSL Radiation Dosimetry

II.1 Radiation dosimetry

Radiation dosimetry in the field of medical physics and radiation protection refers to measuring, calculating, and assessing the dose of ionizing radiation absorbed by an object, often the human body. This occurs internally, by ingestion or inhalation of radioactive substances, or externally, by irradiation by radiation sources. Evaluation of internal dosimetry is based on a variety of monitoring techniques, bio-assay or imaging using radiations, while external dosimetry is based on dosimeter measurements or inferred from measurements displayed by other radiation protection devices. It is widely used for radiation protection, it is regularly employed for monitoring occupational radiation workers in areas where radiation exposure is either expected or unexpected. It is possible to measure and calculate the public absorbed dose using a range of indicators, including ambient gamma radiation measurements, radioactive particle monitoring, and radioactive contamination levels. Other significant disciplines of radiation dosimetry include medicine, where the needed absorbed dose in treatment as well as any collateral absorbed dose are monitored, and the environment, where radon monitoring in buildings is used [45].

Luminescence can be employed in dosimetry for estimating the absorbed dose using detectors exhibiting luminescence in various radiation applications.

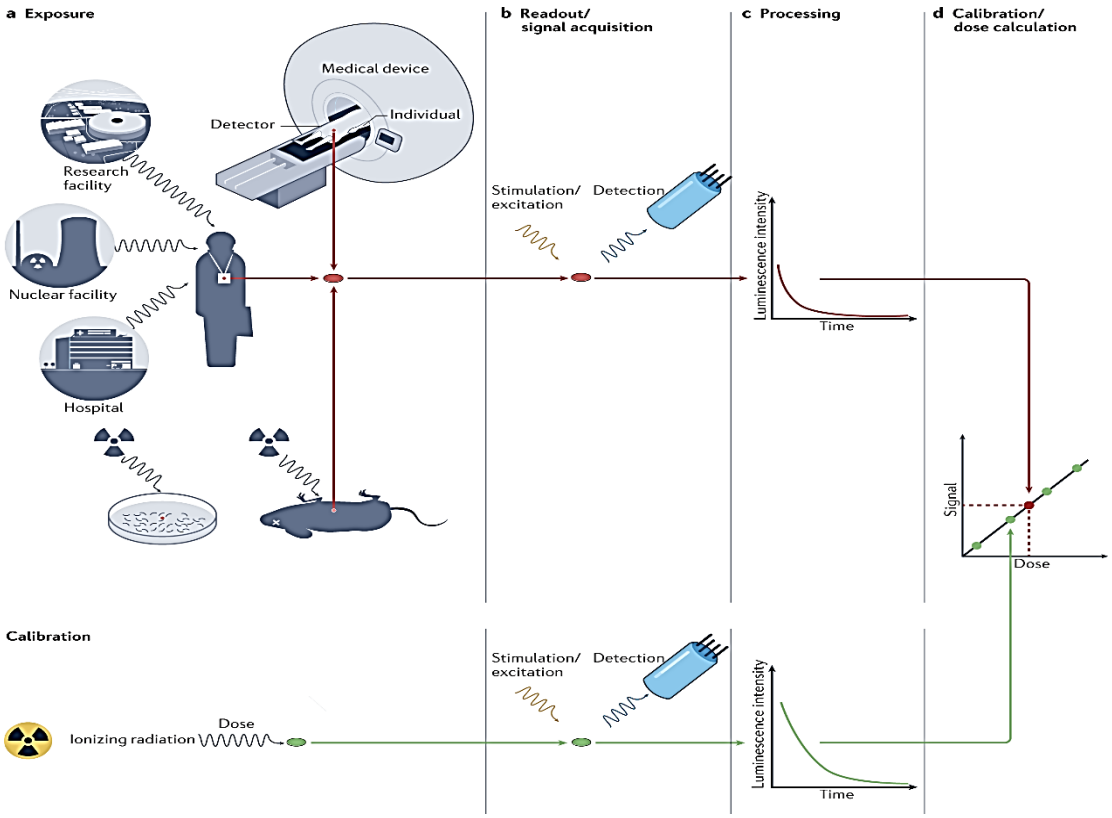

Figure II. 1. Luminescence dosimetry applications: the steps involved [46].

Figure II.1 represents the different steps involving luminescence dosimetry and its applications from exposure to calibration.

The intensity of the luminescence scales with the amount of energy absorbed by the radiation field. Calibration allows the conversion of luminescence intensity to the amount of interest, for instance, the absorbed dose, personal dose equivalent and kerma [46].

II.1.1 Dose quantities and units

II.1.1.1 Kinetic energy released per unit mass: Kerma

Kerma can be defined as the initial kinetic energies sum of all charged particles released by uncharged ionizing radiation (photons and neutrons) per unit mass of a material. It is defined as:

$$K = \frac{dE_{tr}}{dm} \tag{II.1}$$

To assess radiation protection, kerma in air or air kerma K_a is used.

The joule per kilogram (J/kg), referred to as the gray (Gy), is the kerma's international system (SI) unit.

II.1.1.2 Absorbed dose D

Absorbed dose is a basic physical quantity that represents the amount of energy absorbed per unit mass of a material and has been successfully used in applications of "high-dose" in radiation therapy, industrial ionizing radiation applications, and low-dose exposure in radiation protection. It is defined as:

$$D = \frac{d\varepsilon}{dm} \tag{II.2}$$

where $d\varepsilon$ is the average energy supplied by ionizing radiation to the matter in a volume element, dm is the matter's mass in the volume element.

The international system unit of absorbed dose is gray (Gy).

II.1.1.3 Linear energy transfer: LET

LET is the amount of energy transferred by an ionizing particle to the substance traversed per unit distance. It describes the effect of radiation in matter. It is defined as:

$$L_\Delta = \left(\frac{dE}{dl}\right)_\Delta \tag{II.3}$$

A LET high value implies that energy is deposited within a short distance.

Low LET: LET <10 keV/μm.

Examples: beta radiation, secondary electrons of X and gamma-rays.

High LET: LET >10 keV/μm.

Examples: heavier ions, alpha radiation and secondary charged particles produced by neutrons.

II.1.1.4 Equivalent dose H_T

Research in radiobiology has shown that at the same values of absorbed dose, biological damage can vary according to the radiation type. For the same absorbed dose, alpha particles or neutrons, for example, cause greater biological harm than X or gamma radiation. The equivalent dose is adjusted to account for the radiation type effectiveness [47].

$$H_T = \sum_R w_R D_{T,R} \tag{II.4}$$

where $D_{T,R}$ is the absorbed dose in tissue T by radiation type R,

w_R is the radiation weighting factor defined by regulation.

The tabulated values in the table below are estimated with Relative Biological Effectiveness RBE study and according to report 103 from the International Comission on Radiological Protection ICRP.

Table II. 1. Radiation weighting factor w_R values according to ICRP report 103 [48].

Radiation type R	**Radiation weighting factor, w_R**
Photons	1
Electrons	1
Protons	2
Alpha particles, fission fragments, heavy ions	20
Neutrons	$w_R = \begin{cases} 2.5 + 18.2e^{-((\ln(E_n))^2/6)}, & E_n < 1MeV \\ 5.0 + 17.0e^{-((\ln(2E_n))^2/6)}, & 1MeV \le E_n \le 50MeV \\ 2.5 + 3.25e^{-((\ln(0.04E_n))^2/6)}, & E_n > 50MeV \end{cases}$

The equivalent dose H_T is expressed in sievert (Sv).

II.1.1.5 Effective dose E

The effective dose proposal's overall goal is to establish a quantity that can be directly related to the probability of harm to the human body from exposure to ionizing radiation in the low dose range where only stochastic effects (have a dose-increasing probability without a threshold) occurred. This quantity must be applicable under a wide range of exposure conditions, including external and internal radiation exposure, as well as partial and whole body irradiations [47].

$$E = \sum_T w_T H_T = \sum_T w_T \sum_R w_R D_{T,R} \quad \text{(II.5)}$$

where w_T is defined as the tissue weighting factor.

The values of w_T tissue weighting factor are represented in Table II.2.

Table II. 2. Tissue weighting factor w_T values according to ICRP report 103 [48].

Tissue	w_T
Bone-marrow (red), colon, lung, stomach, breast, remainder tissues	0.12
Gonads	0.08
Bladder, oesophagus, liver, thyroid	0.04
Bone surface, brain, salivary, glands, skin	0.01

The effective dose E is expressed in sievert (Sv).

II.2 TL and OSL applications in radiation dosimetry

Although the earliest theoretical work on TL was published in the 1940s by Randall and Wilkins and subsequently by Garlick and Gibson, the first practical uses of thermoluminescence were proposed in the 1950s by Daniels suggesting the relation between rocks' natural TL and radioactivity from uranium (U), thorium (Th) and potassium (^{40}K) contained in almost all rocks in trace form. In the middle of the 1950s, Antonov-Romanovskiĭ made the first mention of the potential use of optical stimulation rather than thermal stimulation for measuring absorbed dose

in samples for dosimetric purposes [49]. Irradiation and readout procedures of a luminescent detector are represented in Figure II.2.

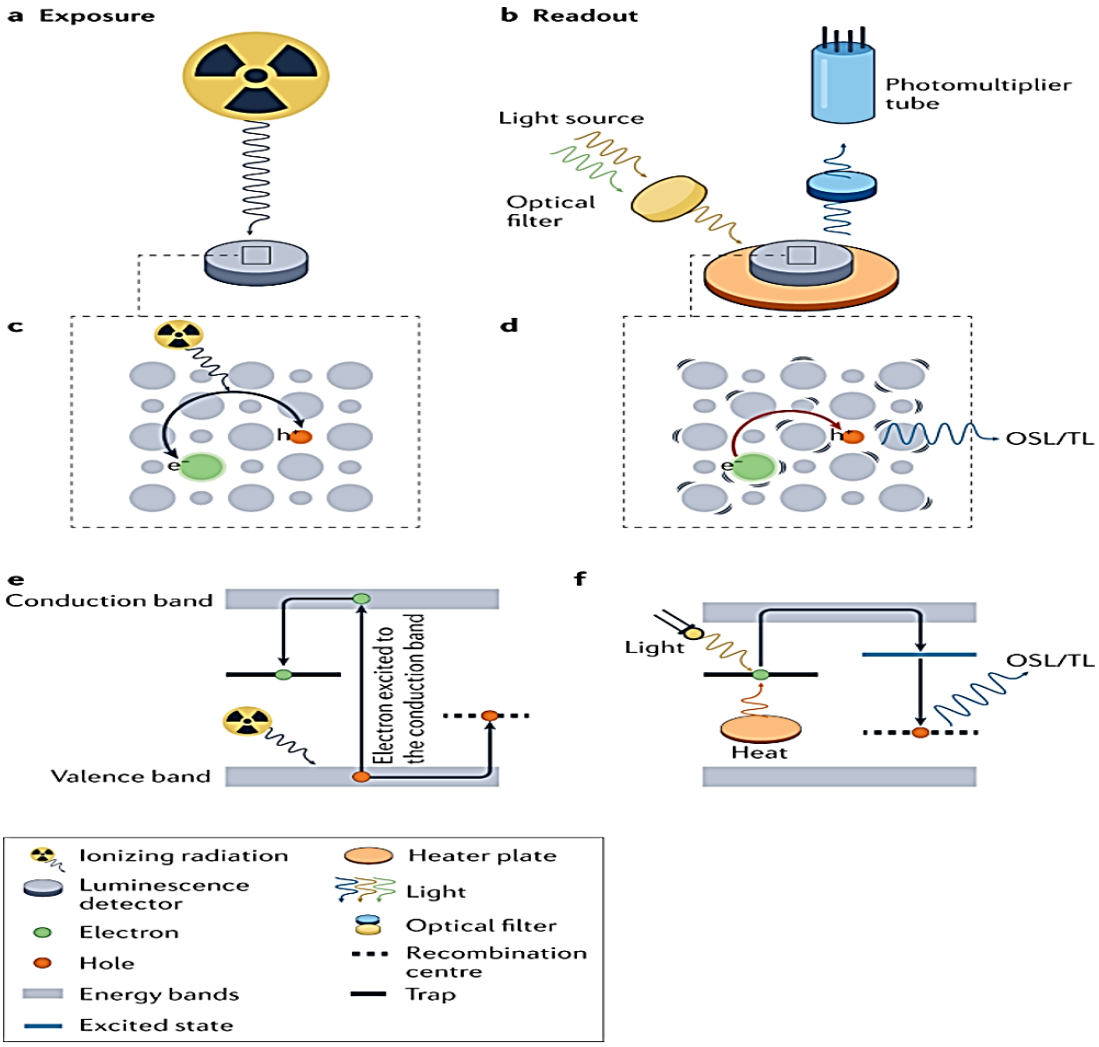

Figure II. 2. A luminescence detector's exposure (irradiation) and readout procedures are represented [46].

Excluding the stimulation source, OSL and TL share the same mechanism. Hence, both techniques can serve the same dosimetric purposes. It is feasible to measure doses as low as those caused by the natural environment over several days, or doses as high as those supplied within a nuclear reactor [50, 51]. However, the application of OSL for diverse dosimetry applications, began in the middle of 1990s. The reason was that sensitive OSL phosphors were not available until the development of Al_2O_3:C and its appropriateness for personal dosimetry. OSL dosimeters have found increasing use in many fields of dosimetry.

Since then, thermoluminescence (TL) and optically stimulated luminescence (OSL) as radiation dosimetry methods of ionizing radiation have been established and have gained a number of useful applications in various fields, including personal, environmental, accident/retrospective, medical dosimetry and high dose dosimetry. TL and OSL techniques can be also used in archaeological and geological dating, [49, 50].

II.2.1 Personal dosimetry

The main purpose of personal monitoring/individual monitoring is to measure or assess radiation doses received by individuals during occupational exposure. Workers in the nuclear industry, radiotherapy technicians in hospitals, industrial radiography workers, γ-irradiators of high intensity and nuclear powered vessels' naval personal.

Figure II. 3. Personal dosimeter examples [54].

Furthermore, the objectives of personal monitoring for external exposures include:

1. Providing information on individuals exposed to external radiation when working with radioactive substances and/or radiation generating devices,
2. Results of personal monitoring give insight into routine exposures, help in work planning, enable workplace control and offer information on exposures in incidental situations,

3. It is envisaged that such monitoring will restrict such personal's exposure to within prescribed limits based on recommendations from international and national organizations.
4. For purposes of compliance, evaluate the effective dose and, if necessary, equivalent doses,
5. Furthermore, these results help those in charge of radiation safety in maintaining doses as low as reasonably attainable (ALARA) [52, 53].

Different personal dosimeters including TL, OSL and RPL are shown in Figure II.3 above.

II.2.2 Environmental dosimetry

Over the past decades, regulatory bodies in many countries have become increasingly aware of growing public concern about the potential environmental impacts of "man-made" radiation exposure, including:

1. Controlled gaseous radionuclide releases from nuclear power plants during normal operations,
2. Disposal of low level waste (LLW),
3. Reprocessing of nuclear fuel,
4. Nuclear power plant accidents and activities related to the nuclear industry.

Figure II. 4. Station of environmental TLDs used in Instituto de Engenharia Nuclear-IEN for environmental kerma assessment [56].

TLD and OSLD systems are installed near nuclear sites in many different countries to monitor both pre-operational (background) levels and above natural background levels that may be associated with the operation of those facilities, as shows Figure II.4 while assessing environmental kerma [55].

II.2.3 Medical dosimetry

One of the most important applications of TL and OSL dosimetry is in the medical physics field for its use in diagnostic radiology, radiotherapy and nuclear medicine. TLDs (thermoluminescent dosimeters) have gained popularity in this field due to their excellent characteristics. TL phosphors are commonly used for clinical dosimetric studies such as depth-dose curves of the central axis, in-phantom measurement, surface dose measurement, *in-vivo* dosimetry (IVD) and high energy photon and electron beams' quality assurance. OSL dosimeters (OSLDs), like TLDs, can be utilized as passive dosimeters in medical physics for a variety of applications such as *in-vivo* dosimetry (IVD) and dosimetry of charged particle high Linear Energy Transfer (LET). Al_2O_3:C as an exmaple of OSL dosimeter is shown in Figure II.5 and is used for brachytherapy.

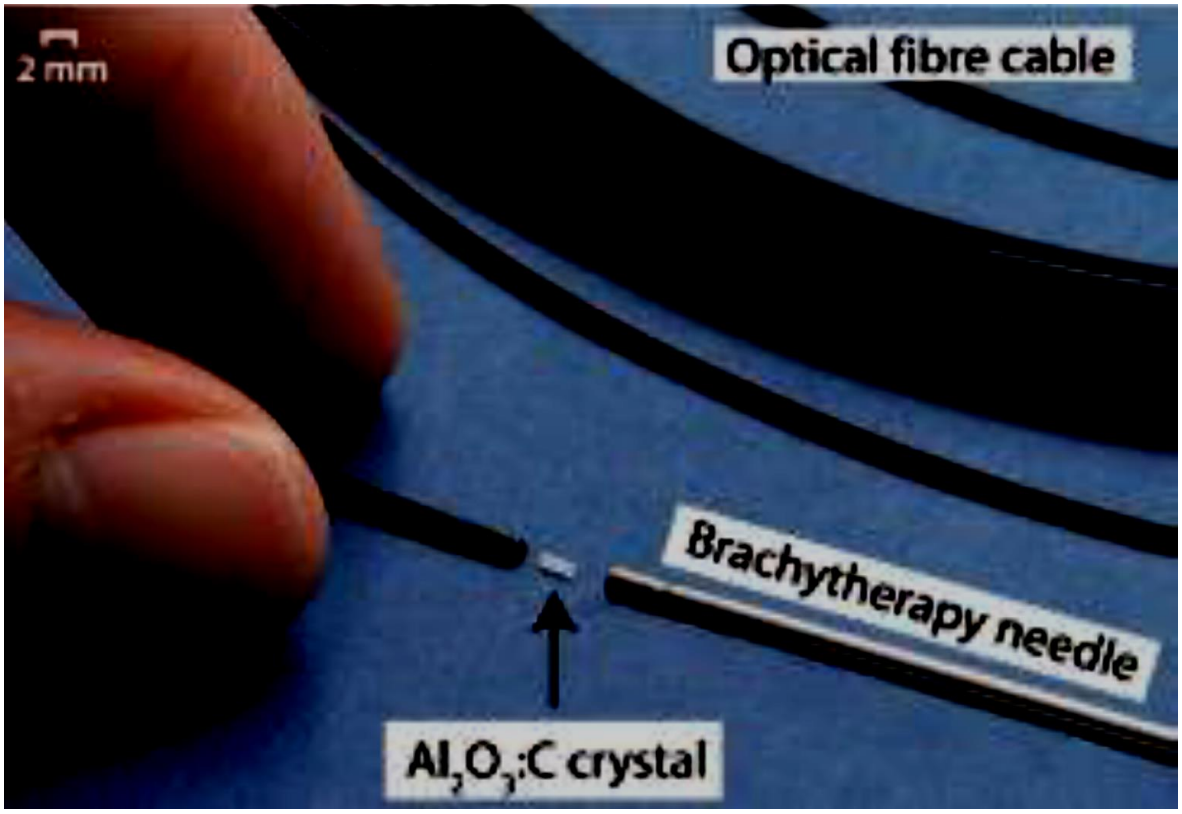

Figure II. 5. Example of OSL dosimeter used in brachytherapy [58].

The TLD and OSLD materials must be tissue equivalent and very sensitive. The latter is required for laboratory measurements that need for the TLD and OSLD materials to be as small as possible. Aside from these features, the TLD and OSLD should not be toxic [57].

II.2.4 Retrospective dosimetry

In the absence of data from direct radiation monitoring, reconstructions of luminescence doses using materials from population's immediate environment or from persons near the incident/accident may be employed to validate the values derived from computational methods. The TL method has effectively been employed for dose assessment in the aftermath of the atomic bombings in Hiroshima and Nagasaki, Japan, as well as radioactive fallout resulting from nuclear testing at the Nevada test site in the United States and Chernobyl accident in Ukraine. Additionally, the OSL method has been employed for retrospective dosimetry by analyzing environmental samples from the area of the Chernobyl disaster [51].

II.2.5 Space dosimetry

The space radiation environment is a complex mixture of charged particles that span a variety of energy ranges and fluxes, including: protons, electrons, α-particles of medium and high energy and heavy ions of high energy.

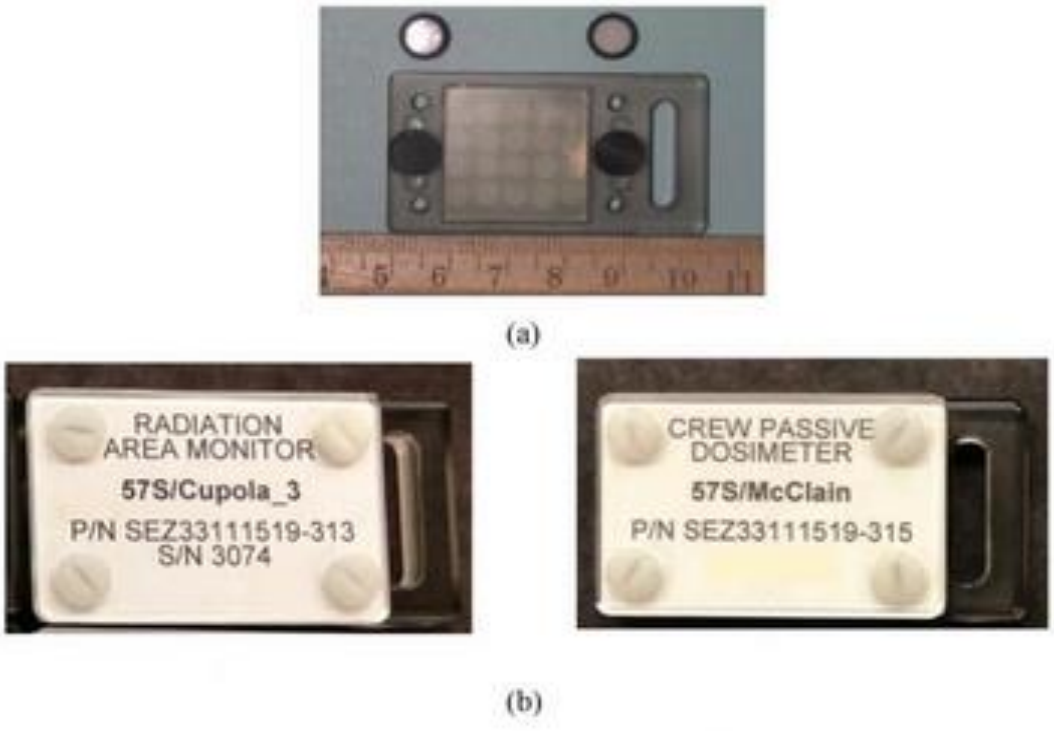

Figure II. 6. (a) NASA's dosimeter and (b) Radiation area monitor and Crew passive dosimeter [54].

Astronauts operating in low earth orbit are subjected to radiation levels that are approximately 100 times greater than the natural radiation level on Earth, and even more when traveling to Mars [39]. The Space Shuttle and International Space Station have many daily activities for the space crew, it is essential to monitor the individual exposures of the crew members to radiations to accurately assess the associated radiation risks. Figure II.6 presents some types of TL and OSL dosimeters used to assess the exposure of individuals to radiations.

The National Council on Radiation Protection & Measurements (NCRP) recommend the use of TL or OSL detectors as passive detectors for the space field's low LET component (i.e. LET area of <10 keV/ mm) [59].

II.2.6 High dose

TLDs and OSLDs are also applied in high dose regimes, high doses (10^2 Gy to 10^6 Gy) are used for materials testing, sterilization of food and other similar applications of irradiation as shows Figure II.7 [50, 60].

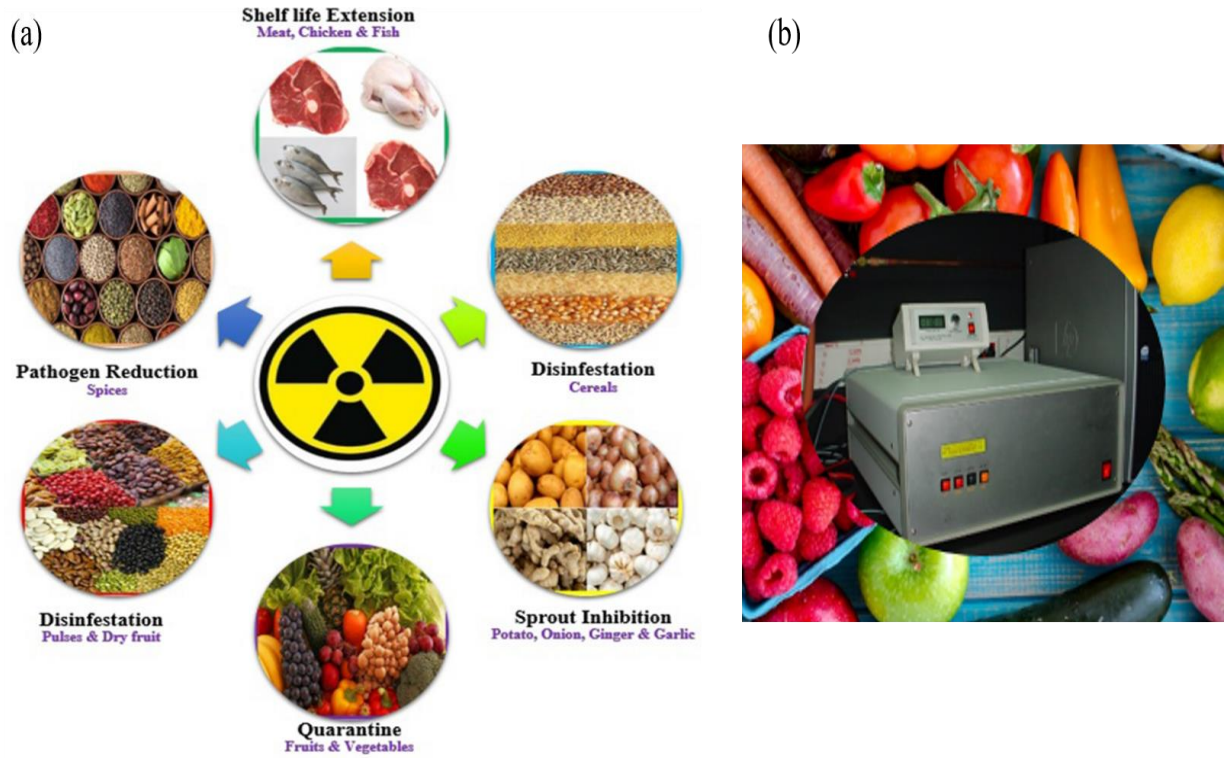

Figure II. 7. (a) Irradiation application in food processing and (b) thermoluminescence analysis by thermoregulator in food irradiation testing [61].

II.3 Basic characteristics of TL and OSL dosimeters

A radiation dosimeter is an instrument, device, or system for measuring or evaluating, directly or indirectly, the amounts exposure, absorbed dose, kerma or their time derivative

(rates), as well as associated amounts to ionizing radiation. A dosimetry system consists of a dosimeter and its reader. A dosimetry system includes a dosimeter and its reader.

In order to operate as a radiation dosimeter, the dosimeter must have at least one physical characteristic that is dependent on the measured dosimetric amount and can be utilized for radiation dosimetry with appropriate calibration. To be effective, radiation dosimeters must offer many desired features including accuracy and precision, dose-linearity, dose rate reliance (dependence), response to energy, directional reliance and spatial resolution.

Clearly, not all dosimeters can meet all criteria. The selection of a radiation dosimeter and its reader must thus be made carefully, considering the measuring situation's requirements [62].

II.3.1 Accuracy and precision

The uncertainty associated with a measurement in radiotherapy dosimetry is frequently expressed in terms of accuracy and precision.

Dosimetry measurements precision specifies the reproducibility of measurements under similar conditions and can be estimated using data from repeated measurements. High precision can be associated with a low standard deviation of the distribution of measurement results. The accuracy of dosimetry measurements is defined as the proximity of the expected and true values of the measured quantity. Measurement results cannot be completely accurate, and this inaccuracy is referred to as 'uncertainty. When dosimetry measurements are optimized, a standard deviation of 2% or less can be obtained with either manual or automatic readers of good quality associated with reliable TL and OSL materials.

- An error has a numerical value as well as a symbol.
- In general, measurement errors can’t be precisely known, but rather estimated as best as feasible, and compensatory corrections are made when possible.
- After applying all known corrections, the expected value for the errors must be zero, and the only quantities to be concerned with are the uncertainties.

II.3.2 Dose-linearity

Ideally, the dosimeter reading M should be linearly proportional to the dosimetric quantity Q. However, non-linearity occurs beyond a certain dose range and should generally be corrected. The linearity range and non-linearity behavior of a dosimeter depend on the type and physical characteristics of the dosimeter. A dosimeter and its reader may be nonlinear on their

own. Non-linear behavior should be corrected in general, and for that, the combination of both dosimeter and its reader may produce linearity over a wider range.

Dose-response function, known as supralinearity index f (D) is the functional dependence of the the recorded TL signal intensity upon the absorbed dose. It is provided by Eq.(II.6) as :

$$f(D) = \frac{S(D)/D}{S(D_1)/D_1} \tag{II.6}$$

where $S(D)$ and $S(D_1)$ are the values of the TL intensity at doses D and D_1, respectively. The dose D_1 is a dose at which the linear dose-response occurs.

As a result, an ideal dosimeter would fulfill $f(D) = 1$ throughout a large dose range, such as $D = 0$ Gy to several mGy. However, $f(D) = 1$ is only found in a few TLD materials across a restricted dose range, up to a few Gy. Supralinearity where $f(D) > 1$ is commonly encountered, whereas sublinearity where $f(D) < 1$ is most frequently encountered when approaching to saturation.

Figure II.8 depicts two typical instances of dosimetry system response characteristics. Curve A initially exhibits linearity with delivered dose, then a supralinear behavior, and eventually saturation. At high doses, Curve B exhibits linearity first, followed by saturation.

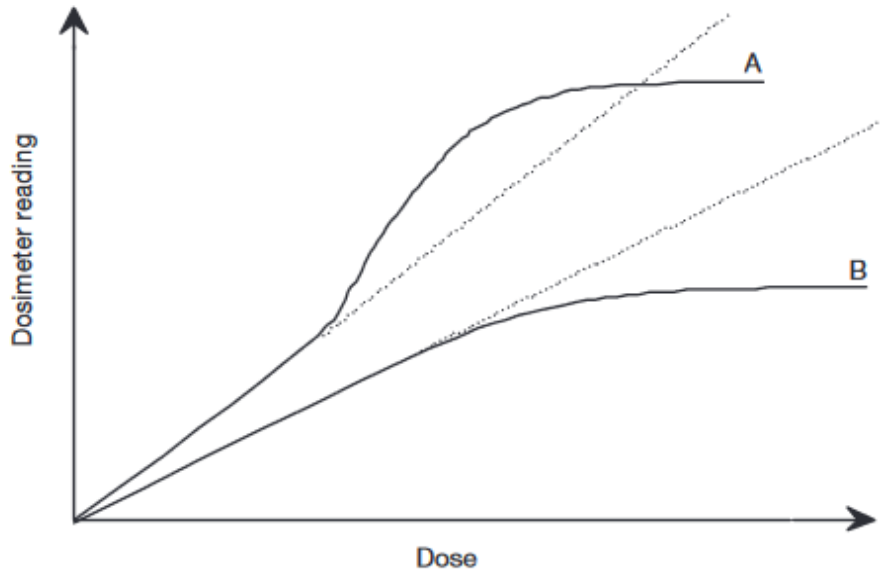

Figure II. 8. Two dosimetry systems' response characteristics [62].

II.3.3 Dose rate dependence

The integrated response of a dosimetry system is measured by integrating systems. The measured dosimetric quantity in such systems should be independent of the rate at which it is

measured. A dosimetry system response M/Q should ideally be constant at two different dose rates ($(dQ/dt)_1$ and $(dQ/dt)_2$).

In reality, the dosimeter readings may be influenced by the dose rate, and appropriate corrections are required.

II.3.4 Energy dependency

A dosimetry system response (M/Q) is generally determined by the quality of the radiation beam (energy). Because dosimetry systems are calibrated at a specific radiation beam quality (or qualities) and used over a much wider energy range, the variation of a dosimetry system's response with radiation quality (referred to as energy dependence) necessitates correction.

The energy response should ideally be flat (i.e. over a certain range of radiation, the calibration system should be independent of energy).

In fact, for most measurement cases, the correction in energy must be incorporated in the estimation of the quantity Q.

II.3.5 Directional dependence

The response of dosimeter is dependent on its variation with the angle of incidence of radiation. Due to their constructional details, physical size and the incident radiation’s energy, the dosimeters usually exhibit directional dependence. In certain applications, the directional dependence is important in some applications, such as in vivo dosimetry while semiconductor dosimeters are used.

II.3.6 Spatial resolution and physical size

Since the dose is a point quantity, the dosimeter should be able to determine it from a very small volume (To characterize the dose at a specific point, a 'point dosimeter' is required.). In a reference coordinate system, the position of the point where the dose is determined (i.e. its spatial location) should be well defined. TL and OSL dosimeters have very small dimensions and their use approximates a point measurement to a great extent.

II.3.7 Sensitivity

II.3.7.1 solid dosimeters: identification

Sensitivity variations within a batch of TL and OSL dosimeters are unavoidable. There are two methods for limiting the impact of these variations:

- One method involves irradiating all of the dosimeters in the same geometrical conditions, reading them, and attributing to each of them a sensitivity factor S_i equal to $R_i/\overline{R}$ to each of them, where R_i is the TL readout from dosimeter number i and $\overline{R}$ is the mean of all values of R_i. Sensitivity factors must be checked regularly to consider a loss of material occurring when TL and OSL dosimeters are not handled carefully.
- Another method for achieving similar accuracy is to divide the TL and OSL dosimeters into sensitivity groups without identifying them individually (for example, groups of dosimeters with a response variation of less than $\pm$ 1 or $\pm$ 2 from the group mean) and increase the number of dosimeters used for each measurement point. When using an automatic reader, this method is ideal because readouts take a very short time. For the same reasons as above, the distribution of sensitivity within a group can vary with time and should therefore be checked with frequency according to the desired accuracy of the measurement.
-

II.3.7.2 Powder: response with mass

When using TL powders, the quantity of powder used and the readout conditions should be accurately defined, with necessary corrections made.

Since the response variations with mass of TL and OSL material depend upon the heating kinetics, they should be established for the readout conditions used. When most of TL and OSL materials are read out with linear heating kinetics, the signal is proportional to the mass: either a linear correction with samples of various weight should be made, or those of equal weight should be used.

II.3.8 Signal stability after irradiation

The choice of TL and OSL dosimeter is by considering the stability of the signal after irradiation. Its particularly important to assess whether the trapped charges during the irradiation have not been lost due to unwanted exposure to heat (thermal fading), light (optical fading) or other factors (anomalous fading) before the readout. This can be expressed by the decrease of the TL and OSL dosimeter response depending on the delay between irradiation and readout.

The thermal fading can be reduced considerably for most of dosimeters by an appropriate preheating, which allows the elimination of that part of signal (low temperature peaks). Thermal fading should be evaluated on each individual reader with the material that is intended to be used in practice.

The optical fading is avoided by manipulating the dosimeters in incandescent light illuminated room and wrapping them in opaque containers or envelopes, when utilized for in vivo dosimetry in treatment rooms illuminated with fluorescent light.

Since anomalous fading occurs much more slowly than thermal or optical fading, it is much more difficult to detect it. Perhaps as a result, it has not yet been proved to be a problem for in vivo dosimetry [62, 63].

CHAPTER III

State of the Art of TL&OSL Materials

III.1 Historical development of TL/OSL materials

A phosphor for use in dosimetry should possess the following characteristics : 1) high efficiency of luminescence; 2) trapped charge carriers' long storage stability and hence the signal stored at normal temperature; 3) simple structure of glow curve; 4) chemical stability and resistance to extreme environmental conditions such as humidity and temperature; 5) preferably, a response near tissue equivalence; 6) linear response to dose over a wide range; 7) The emission spectrum of TL should be appropriate for the detector system; 8) simple procedure of annealing for reutilization, with no sensitivity loss with reutilization and repeated annealing; 9) must possess a good shelf life (i.e., its sensitivity should not decrease after utilization for a long time); 10) not affected by any external agents such as mechanical, electrical or any other kind; 11) ease of synthesis in terms of equipment and economy; 12) must have a high photo-ionization cross section for a given wavelength of stimulation [64].

Since the 1950s, a key area of research in luminescence dosimetry has been the search for new materials for thermoluminescence and optically stimulated luminescence dosimetry exhibiting good linearity over wide dose range, high sensitivity, luminescence signal stability and excellent reproducibility. Historically, OSL material development has consistently focused on materials explored for TL that fade with exposure to light [3].

As TL/OSL expands into applications outside personal and environmental monitoring, the concept of an 'ideal' material will also need to be revised to reflect new applications.
Since then, there has been an increase in reviews of TL and OSL material. Although lots of materials exhibit promising TL & OSL features, few are used for routinely dosimetry assessment or commercially available.

Doped fluorides (LiF, CaF_2), oxides (BeO, MgO, Al_2O_3), sulfates ($CaSO_4$) and borates ($Li_2B_4O_7$ and MgB_4O_7) are the most common TL dosimetric materials. In OSL case, only BeO and Al_2O_3:C are used in commercial systems of dosimetry and represent highly sensitivity to ionizing radiation [65].

Figure III.1 shows examples of TL and OSL dosimeters cited above with different shapes in carrousel of Risø TL/OSL reader.

Figure III. 1. Example of TL&OSL dosimeters [65].

III.2 Main TL & OSL materials

III.2.1 Lithium fluoride LiF

LiF has been the most commonly used thermoluminescence (TL) dosimetry material for decades because it is close tissue equivalence ~8.2, wide range of doses, high sensitivity and negligible fading. LiF has been reported to exhibit luminescence emission even with light stimulation (470 nm) showing weak OSL response. Many research groups have been working to improve the OSL properties of LiF material. Two commercially available phosphors are LiF: Mg, Cu, P (TLD-700H) and LiF: Mg, Ti (TLD-100). Because of its adequate sensitivity, low fading and good reproducibility, LiF: Mg, Ti is commonly employed. Although LiF: Mg, Cu, P is 30-50 times sensitive than LiF: Mg, Ti, but when annealed above 513 K, it loses its TL sensitivity, resulting in high residual signal. With TL sensitivity higher than LiF: Mg, Cu, P, stable structure of TL glow curve, and stable TL sensitivity up to 553 K temperature of annealing, LiF: Mg, Cu, Na, and Si has been created to deal with these shortcomings. Because the choice of an appropriate dopant might alter the OSL characteristics of the phosphor, a significant response towards optical stimulation of LiF: Mg, Cu, Na, Si phosphor has recently been found [66, 67].

LiF dosimeters are often available as powders with grain sizes ranging of 70-180 µm, or as chips made up of pressed microcrystals collection shaped into a round disk of 3-4 mm diameter, or a square of 3-4 mm dimensions with a thickness of 0.1-0.8 mm.

Pure LiF is characterized by a cubic structure with lattice parameter $a = 4.028$ Å. The insertion of Mg dopant causes a substitution of Li atom by Mg atom. Similar to other alkali halides, the TL process in LiF is caused by the recombination of interstitial halogen atoms thermally released from traps with vacancy center F [68]. Figure III.2 depicts LiF:Mg defects that may be attributed to Mg dopant in many scenarios.

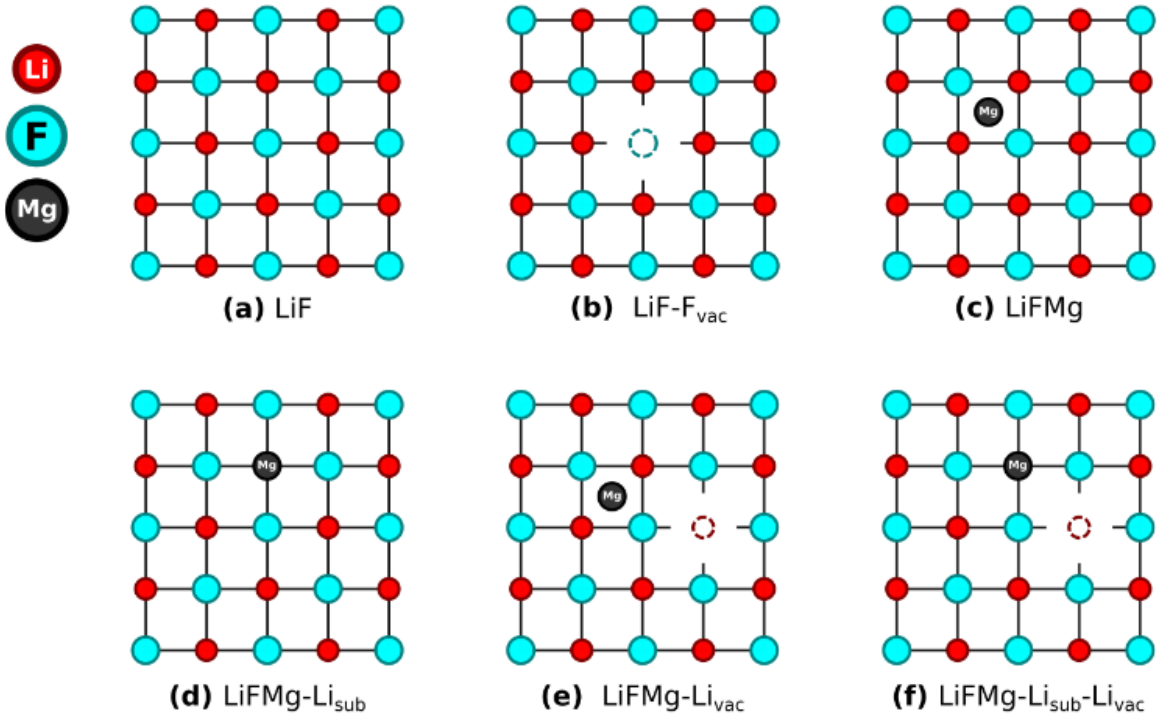

Figure III. 2. Simplified illustrated structure for initial configurations. An unfilled circle indicates vacancies. **(a)** pure LiF, **(b)** LiF with vacancy of F atoms, **(c)** LiF with a Mg interstitial, **(d)** LiF with a Mg substitutional, **(e)** LiF with a Li vacancy + a Mg interstitial and **(f)** LiF with a Li vacancy + a Mg substitutional [68].

The insertion of Ti atoms into LiF :Mg host matrix stabilizes the traps present in LiF and other caused by Mg atoms [68].

III.2.2 Calcium fluoride CaF_2

CaF_2 is an insulator with a large-band gap, commonly used material in many TL dosimetric applications, whether it is natural or activated by different dopants including Mn,

Tm, and Dy, known as TLD-400, TLD-300 and TLD-200, respectively. Aside from its suitable TL dosimetric characteristics such as high sensitivity, linearity over a wide dose range, and high TL response stability, another interesting property is its light sensitivity, which allows this material to be employed as an OSL material [69, 70]. CaF_2 dosimeters of various types are commercially available in powder or sintered pellet form.

CaF_2 has a face-centered cubic structure as depicted in Figure III.3, with a lattice parameter $a = 5.45$ Å. Self-trapped holes (V_k centers), color centers (F centers) and Ca^{2+} vacancies contribute to the luminescence emission in natural CaF_2 material [71].

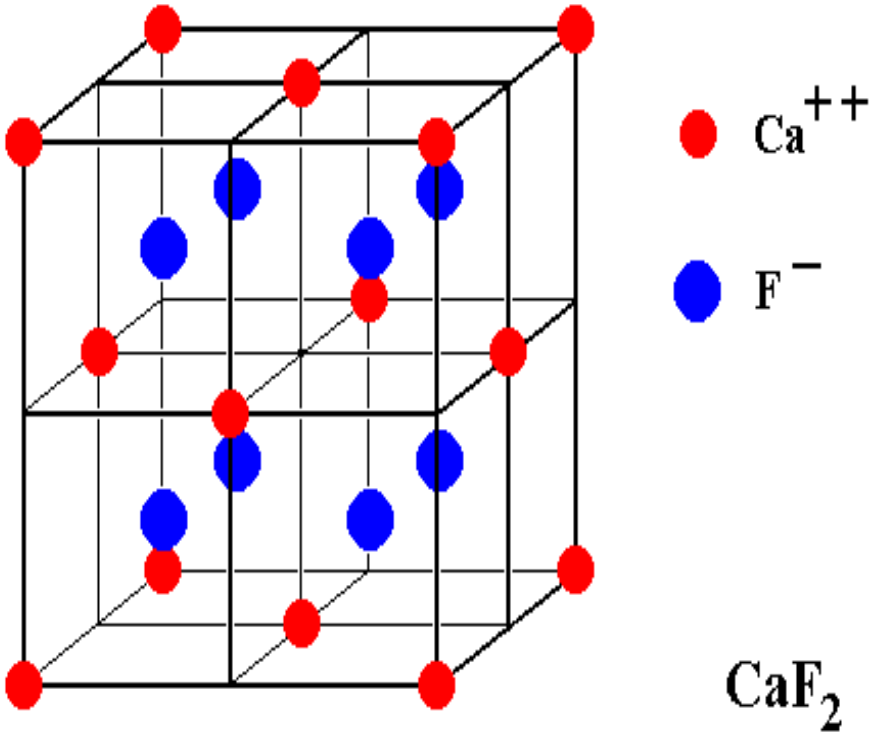

Figure III. 3. CaF_2 structure [72].

III.2.3 Beryllium oxide BeO

BeO has been investigated as a potential TL material and has been used in TL dosimetry applications due to its dielectric properties, thermal conductivity, chemical stability, high thermal resistance to shocks low cost, high sensitivity to ionizing radiation and linearity of TL dose response. BeO has been proposed as an alternative dosimeter material that might compete with LiF owing to its near tissue equivalency. Its TL glow curve shows three peaks located at 50, 192 and 340 °C, employing a heating rate of 5 °C/s, with the 192 °C peak considered as

the main peak used for dosimetry purposes. Light sensitivity of these TL peaks was found, and light fading might be an issue in TL dosimetry applications. Since then, BeO has been indicated to be suitable for OSL dosimetry. The OSL signal's excitation spectrum of BeO was obtained as a single broad peak at around 435 nm in the range 420-550 nm. The possible relationship between the OSL signal and the TL peaks in the glow curve was investigated. It's worth noting that the highly light-sensitive peak in the TL glow curve around 192 °C has no effect on the OSL signal. The recorded OSL signal was found to be generated by a trap close to 340 °C. Its dose response was also studied to determine whether the material might be used for radiation dosimetry. Up to 10 Gy, the dose response was found to be linear [73]. BeO is commercially available as ceramic square or disc chip known as Thermalox 995.

BeO has a wurtzite structure (see Figure III.4) with a hexagonal crystal structure with lattice parameters $a = b =$ 2.696 Å, $c =$ 4.379 Å [74]. Its band gap is of 10 eV. F, F^+ (anion vacancies in various charge states) and V (hole-trapped centers based upon cation vacancies) centers are present in BeO material, improving its luminescence properties [75].

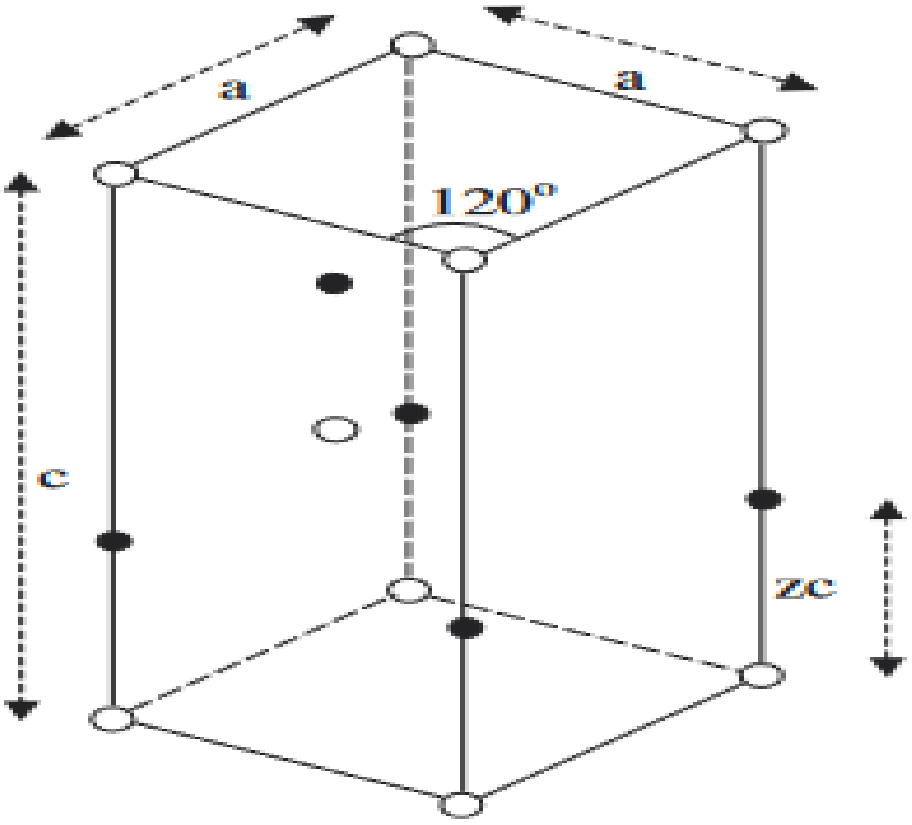

Figure III. 4. The BeO unit cell in the hexagonal wurtzite structure. Black spheres are anions, whereas open spheres indicate cations [74].

The principal impurities in BeO are Si, B, Ca, Mg, and Al elements, which have been shown to be responsible for the signals of TL and OSL [73].

III.2.4 Magnesium oxide MgO

MgO has long been recognized as a thermoluminescent material because of its high chemical stability, effective atomic number equal to 10.8, linearity of dose up to 10^2 Gy, and promising OSL properties. This material is now of interest mostly from its prospective application in neutron dosimetry and as UV dosimeter. MgO is available as pellets for ease of handling.

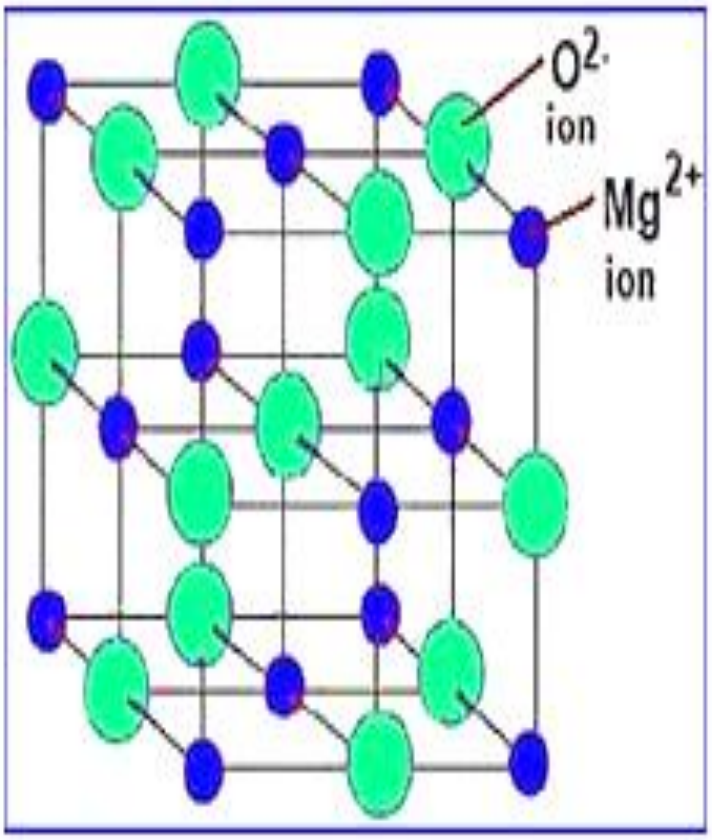

Figure III. 5. Crystal structure of MgO nanoparticle [78].

The MgO material has a cubic lattice structure as depicts Figure III.5, with a large band gap ~ 7.8 eV. The presence of F and V-type centers In such applications, transition metal ions (V, Ni, Ti, Al, Mn, Cr, Fe) as dopants play an important role in the mechanism of luminescence.

In recent years, research on Tb-doped MgO synthesis has led to the creation of new luminescent centers that enhance its properties in personal and medical dosimetry, and MgO has attracted attention as a radiation dosimeter [76, 77].

III.2.5 Aluminium oxide Al_2O_3

Al_2O_3 is one of the earlier materials studied for possible use in dosimetry since the 1960s. Al_2O_3 offers great mechanical property as well as high chemical, optical, thermal stability when exposed to radiation and excellent charge-transfer mechanisms. When compared to thermoluminescence, research has revealed that Al_2O_3 has a high optical sensitivity, indicating certain benefits, including luminescence efficiency, sensitivity, stability, and control over the luminescence emitted, which is promising for application in the OSL technique.

Other Al_2O_3 advantages include low effective number equal to 11.28, linearity within a large dose range, low cost and ease of handling, make it an excellent candidate for luminescence dosimetry in radiation dose control.

The TL glow curve of pure Al_2O_3 dosimeter shows two well-separated peaks, one is below 100 °C and the other is at ~208 °C using a heating rate of 5 °C/s. The dosimetry peak is the second stable peak. To enhance Al_2O_3 luminescent characteristics, doping with different impurities (notably C, Na, Mg, Sr, Li and rare earth ions) results in the development of new recombination and trap centers, improving its ionizing radiation sensitivity. As a well-known fluorescent activator, Sb^{3+} ion has gotten a lot of attention for improving luminescence properties in a variety of host materials. Al_2O_3 :C Al_2O_3 TL-OSL dosimeters are commercially available in form of powder or disk shaped dosimeters of 4 mm diameter and of 1 mm thickness [79, 80].

Only α-Al_2O_3 structure is employed for dosimetric purposes. α-Al_2O_3 has a rhombohedral crystal structure shown in Figure III.6, with $a = b = 4.762$ Å, and $c = 12.999$ Å. It is one of the earlier materials studied for possible use in dosimetry because of the presence of F_2, F_2^{2+}, F and F^+ centers that act as luminescence sites exhibiting TL properties [64].

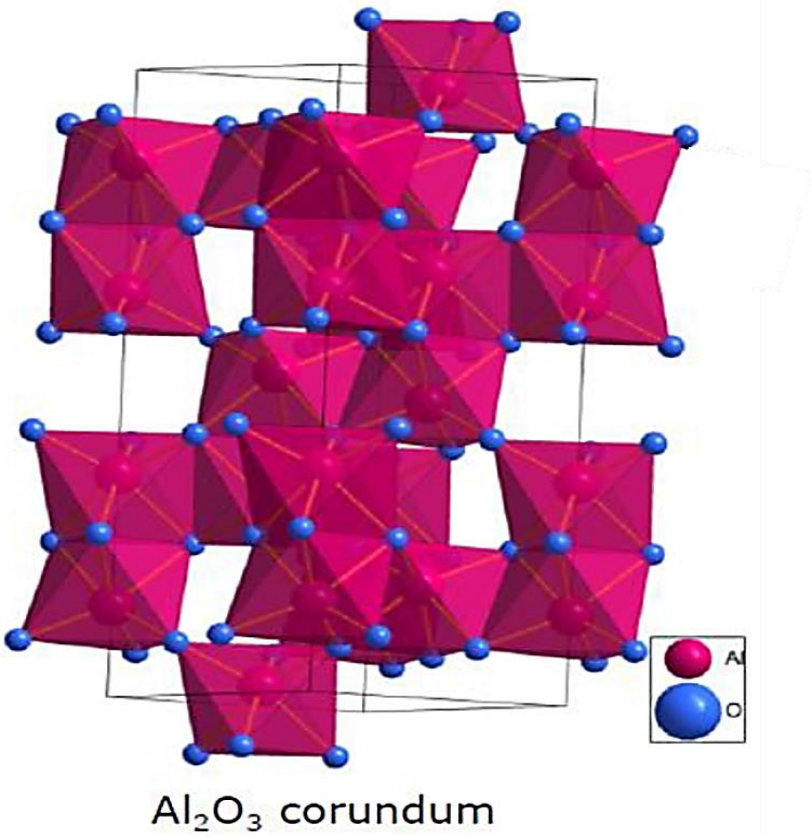

Figure III. 6. α-Al_2O_3 Crystal Structure [64].

III.2.6 Calcium sulfate $CaSO_4$

$CaSO_4$ is a commercially available thermoluminescent material for radiation dosimeters. It is one of the materials under investigation for dosimetry applications as it offers high TL sensitivity response at low doses, low fading ($< 5\%$) and radiation damage inertness. Its sensitivity to light reduced its popularity as a TL dosimeter. This inspired researchers to use its shortcoming of being light-sensitive to its potential as an OSL dosimeter. Mn and rare earth ions are the most common dopants used for improving the TL and OSL characteristics of $CaSO_4$. It is commercially available in disk and square shaped detectors [81, 82].

The crystal structure of $CaSO_4$ is orthorhombic (see Figure III.7), with lattice parameters $a = 14.065$ Å and $c = 12.506$ Å. The main point defect present in pure $CaSO_4$ is an intrinsic O^- center and when it is doped with some rare earth ions sauch as Dy, another defect appears and is directly attributed to its TL emission which is the Ca^{2+} vacation [83, 84].

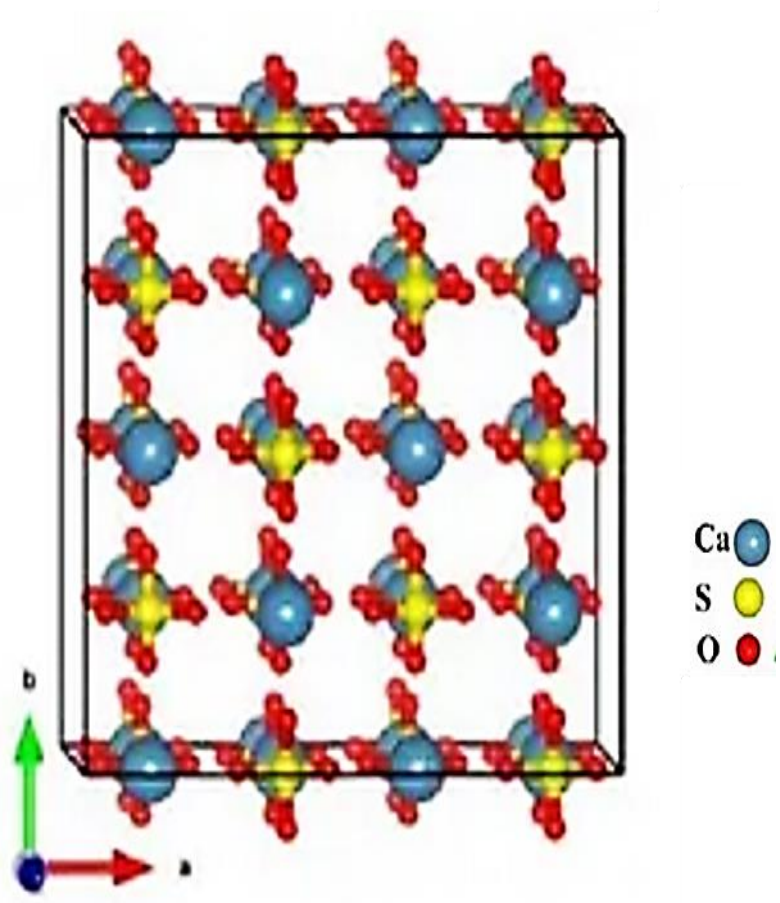

Figure III. 7. $CaSO_4$ crystal structure [82].

III.2.7 Lithium tetraborate $Li_2B_4O_7$

$Li_2B_4O_7$ with ~9.8 eV band gap is a tissue equivalent material with Z_{eff}= 7.37 possessing the properties such as high chemical stability, good optical transparency and high point of melting, that make it a suitable host material for producing luminescence. $Li_2B_4O_7$ is available commercially in form of powder and chips.

$Li_2B_4O_7$ is characterized by a tetragonal structure shown in Figure III.8, with $a = b = 9.475$ Å and $c = 10.283$ Å lattice parameters, belonging to $I4_1cd$ space group. Besides of its intrinsic defects (Li and O vacancies), extrinsic defects can also contribute to luminescence emission. A variety of dopants or codopants are used to increase the TL and OSL sensitivity of $Li_2B_4O_7$. The effect of different dopants: Cu, Ag, P, Mn, Ce and La have been studied [85, 86].

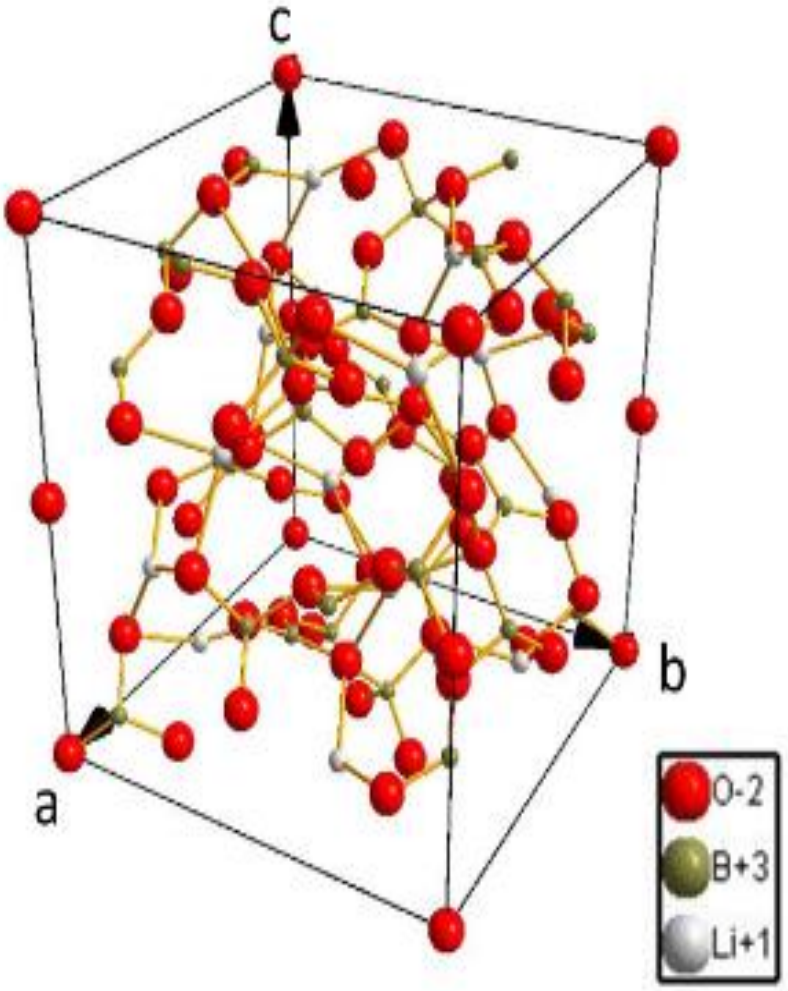

Figure III. 8. The lithium tetraborate unit cell [87].

III.2.8 Magnesium tetraborate MgB_4O_7

MgB_4O_7 is a composite that has been widely used in TL dosimetry since the early 1980s, dute to its low effective atomic number 8.2, high sensitivity to charge particles and photons with linear response over a wide absorbed dose range, mGy-100 Gy, and a large band gap of around 9.5 eV, making it an insulator [88]. MgB_4O_7 is available commercially in powder or disk shaped dosimeter.

The crystal structure of MgB_4O_7 is orthorombic (see Figure III.9), belonging to Pbca space group, with lattice parameters $a = 7.792$ Å, $b = 8.527$ Å, $c = 13.651$ Å [88].

The O Frenkel defect is an intrinsic defect that creates an O vacancy in the host of MgB_4O_7, it has been doped with ions such as Li, Ce, Mn, Na, Gd, Dy, Tb and Tm by many researchers to improve its TL and OSL signal intensities. The Ce, Na co-doped MgB_4O_7

exhibits a linear OSL dose-response curve in the range of 1-100 Gy with a low minimum detectable dose of 0.73 mGy and good reusability feature up to 20 cycles with 4.5% of deviation [89].

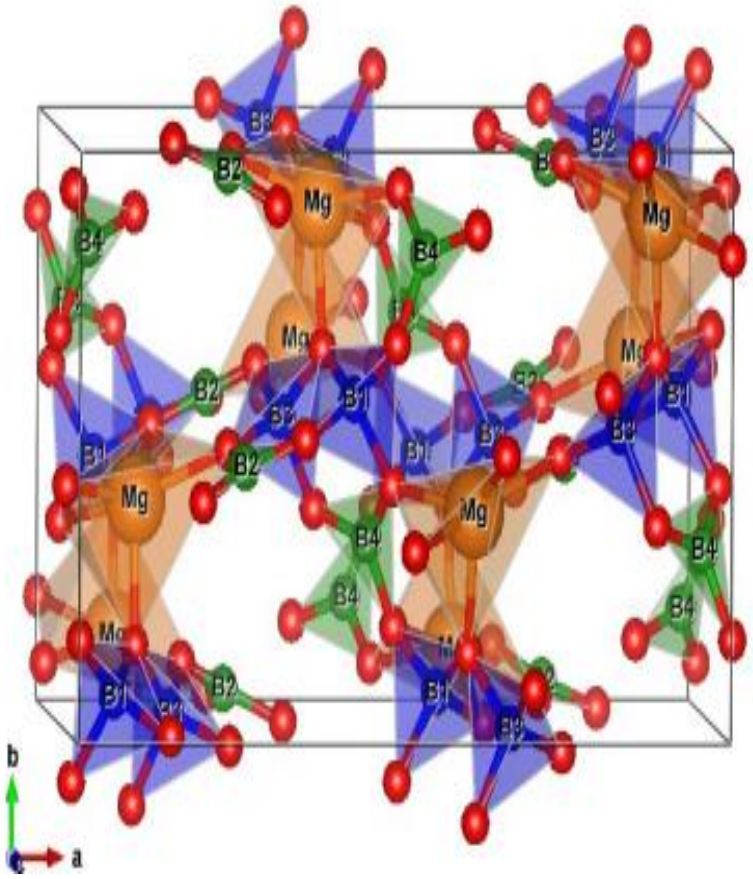

Figure III. 9. MgB_4O_7 crystal structure reproduced using VESTA program [90].

III.3 TL glow and OSL decay curves of main TL-OSL materials and their applications

The TL glow curves of the aforementioned dosimeters with various dopants were recorded at 1°C.s^{-1} after irradiation of detectors using a beta $^{90}Sr/^{90}Y$ source of 50 mGy dose, indicating a change in the shape of the TL peaks from each dosimeter. The OSL decay curves of Al_2O_3:C and BeO were measured using green and blue stimulation, respectively.

As shown in Figure III.10, each TL-OSL material is characterized by its own glow and time of decay.

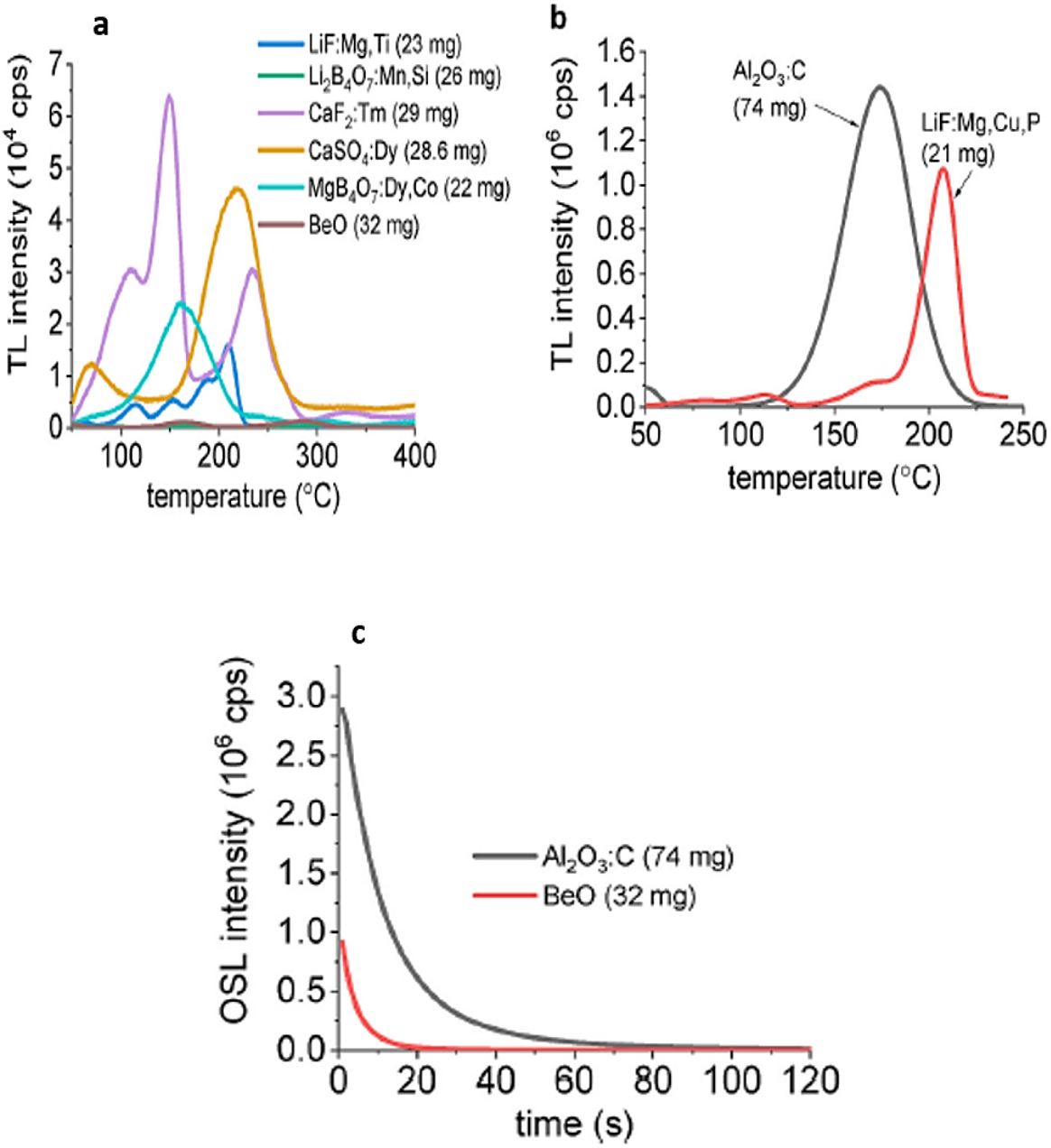

Figure III. 10. (a) TL curves of some TL materials, (b) TL curves of LiF:Mg,Cu,P and Al_2O_3:C and (c) OSL decay curves of Al_2O_3:C and BeO [65].

Table III.1 represents a summary of different TL-OSL materials and their respective applications in dosimetry fields.

Table III. 1. Summary of TL&OSL materials and their applications in dosimetry [65].

Material	*Technique*	Z_{eff}	*Comments*	*Applications*
LiF : Mg, Ti	*TL*	*8.2*	*Linear up to 1 Gy*	*Personal, area monitoring and medical dosimetry.*
$CaF_2 : Mn$	*TL*	*16.9*	*Linear up to 10 Gy*	*Personal and environmental dosimetry.*
BeO	*TL/OSL*	*7.2*	*Linear up to 1 Gy*	*Personal, environmental and medical dosimetry.*
MgO	*TL*	*10.8*	*Linear up to* 10^4 *Gy*	*Personal and medical dosimetry*
$Al_2O_3 : C$	*TL/OSL*	*11.3*	*Linear up to 1 Gy*	*Personal, environmental and medical dosimetry.*
$CaSO_4 : Dy$	*TL*	*15.6*	*Linear up to 10 Gy*	*Personal dosimetry.*
$Li_2B_4O_7 : Cu$	*TL*	*7.3*	*Linear up to* 10^3 *Gy*	*Personal and medical dosimetry.*
$MgB_4O_7 : Ce, Na$	*TL/OSL*	*8.2*	*Linear up to* 10^2 *Gy*	*Personal and medical dosimetry.*

III.4 New materials development strategies

A variety of materials have been studied for potential use in TL-OSL dosimetry. Nonetheless, only a few of them achieved a commercial material status, being manufactured in large quantities and employed in a commercial system. KCl, NaCl, $MgAl_2O_4$, $SrAl_2O_4$, SrB_4O_7, TiO_2, ZnO, $BaSO_4$ and MgS are some examples of synthetic materials exhibiting TL/OSL characteristics have been mentioned in the literature possessing high sensitivity towards ionizing radiations, good linearity over a wide dose range and dependence upon energy [91].

CHAPTER IV

Elaboration and characterization of Antimony (Sb) doped Alumina (Al_2O_3) TL&OSL dosimeter (Al_2O_3:Sb)

IV.1 Objective

Due to its excellent luminescent properties mentioned in chapter III, wide band gap of ~8 eV and ease and low cost synthesis by sol-gel technique, Al_2O_3 was chosen as raw material for the development and elaboration of new and effective TL/OSL dosimeter by using Antimony (Sb^{3+}) which is known as luminescent activator as dopant.

The purpose of this research is the elaboration via sol-gel route, characterization using various analysis techniques including TGA for thermal stability analysis, XRD for crystalline structure analysis, FTIR for chemical bonds and SEM-EDX for morphology and elemental analysis and test of α-Al_2O_3 doped by Sb ions for high radiation detection and dosimetry. We aim to determine the right amount of the dopant according to the higher TL and OSL intensities recorded. A study was conducted on TL and OSL responses of the developed α-Al_2O_3:$Sb_{1\%}$ as a function of dose within a range of 0-80 Gy and energy ranging from 5 keV to 18 MeV in order to determine the most suitable working conditions.

IV.2 Experimental techniques

IV.2.1 Elaboration technique

Various methods are currently used to produce and synthesize ceramics and thin films. The sol-gel process (wet chemical process) is the most popular and used widely in industry. In this process, molecular precursors are dissolved in water or alcohol and then heated and stirred to form gels. Figure IV.1 depicts the different steps involving sol-gel process.

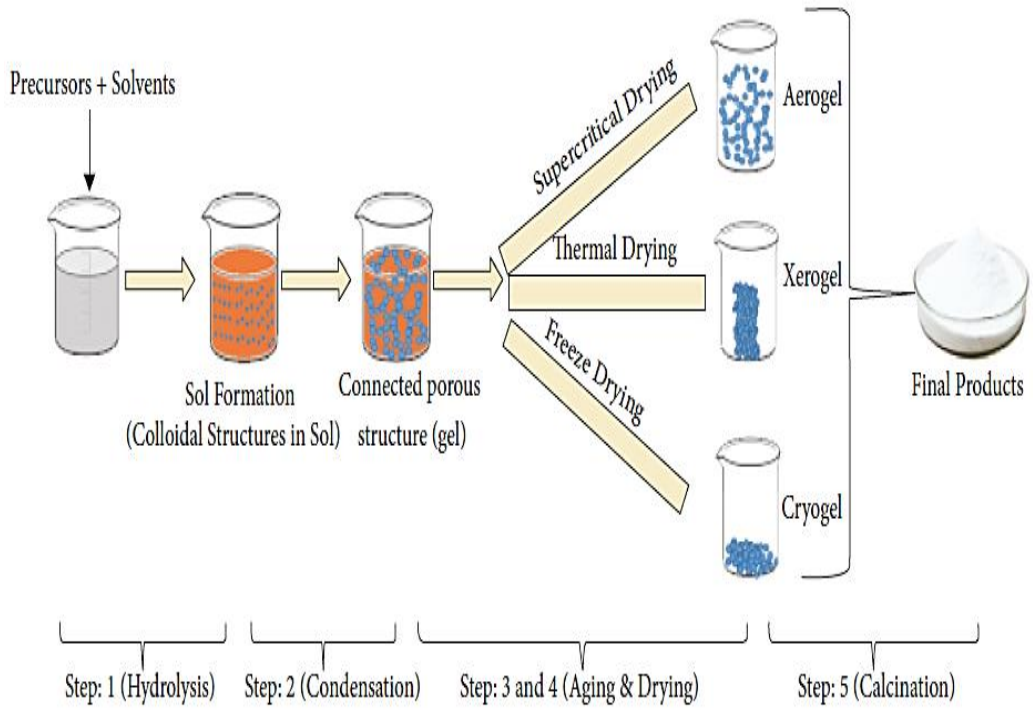

Figure IV. 1. Schematic of the different stages of sol-gel process [92].

Due to their wet (or damp) state, the resulting gel needs to be dried appropriately based on the desired characteristics and intended use. After drying, the gel produced is ground into powder and then calcined.

The key benefits of this process are products with high purity, narrow particle distribution and homogeneous nanostructure' achievement at low temperatures [92].

IV.2.2 Characterization techniques

To study the thermal stability of elaborated amorphous material, crystalline structure, chemical bonding groups, morphology/elemental composition and thermal and optical luminescent properties of both pure and doped α-Al_2O_3 material, TGA, XRD, FTIR, SEM/EDX and TL/OSL respectively, were used in course of this work.

IV.2.2.1 Thermogravimetric Analysis (TGA)

TGA is a useful tool for determining material thermal stability. This method involves monitoring variations in a specimen's weight as its temperature rises. The TGA can be used to measure the moisture and volatile components of samples. The device is made up of a very sensitive scale for measuring the changes in weight and a programmed furnace for controlling the sample's heat as represents Figure IV.2 [93]. SDT Q600 V20.9 Build 20 TGA analyzer was used with 10 °C/min heating rate under a nitrogen flow.

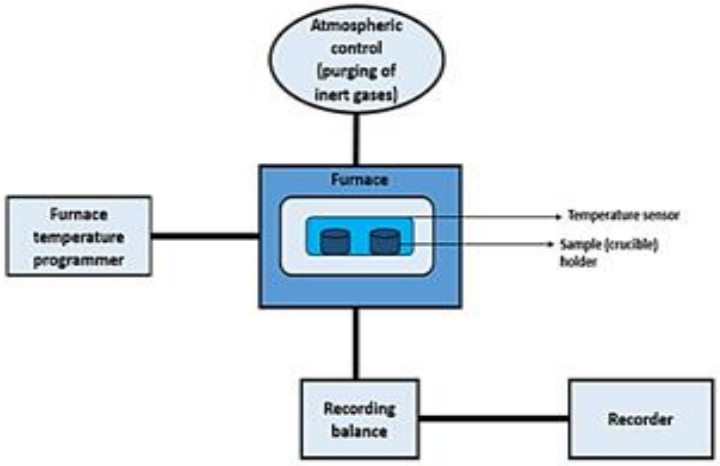

Figure IV. 2. (a) Schematic diagram of TGA.

IV.2.2.2 X-Ray Diffraction analysis (XRD)

The X-Ray diffraction (XRD) analysis is a non-destructive method that offers information about crystalline structure and chemical composition of materials. It is based on constructive interference that occurs between monochromatic X-rays and crystalline sample.

X-rays are electromagnetic waves with shorter lengths produced by decelerating electrically charged particles with sufficient energy. The generated X-rays are concentrated by collimation and directed at the sample. When the incident rays interact with the sample a diffracted ray is produced, detected, processed and finally counted. The intensity of the scattered diffracted rays at various angles of material is plotted for displaying a diffraction pattern with material corresponding peaks [94, 95]. Based on peak positions, intensities, widths and shapes, several parameters can be identified including:

- Crystalline phases using PDF (Powder Diffraction File),
- Preffered orientations (hkl),
- Crystallite size based on the full width at half maximum (FWHM), and Scherrer equation given by:

$$D = 0.9\frac{\lambda}{\beta \cos\theta} \quad \text{(IV.1)}$$

where, D is the average crystallite size (nm),

λ is copper K_α emission radiation wavelength ($\lambda = 1.54060$ Å),

β represents the XRD peak's full width at half maximum,

θ is the position of diffraction peak.

The inter-atomic spacing (d-spacing) which is the distance between atoms' parallel planes of can be calculated by Bragg's law:

$$2d_{hkl} \sin\theta = n\lambda \quad \text{(IV.2)}$$

θ is the incidence and reflection angle,

n is the diffraction order.

Figure IV.3 represents XRD principle according to Bragg-Brentano geometry.

The crystalline structure of as-elaborated samples was carried out with Panalytical X'Pert-PRO MPD diffractometer using Bragg-Brentano geometry (θ-θ) and X-ray generator of 40 mA and 30 kV. The diffraction patterns were recorded at 25°C over 10-90° angular range with 0.02° step size.

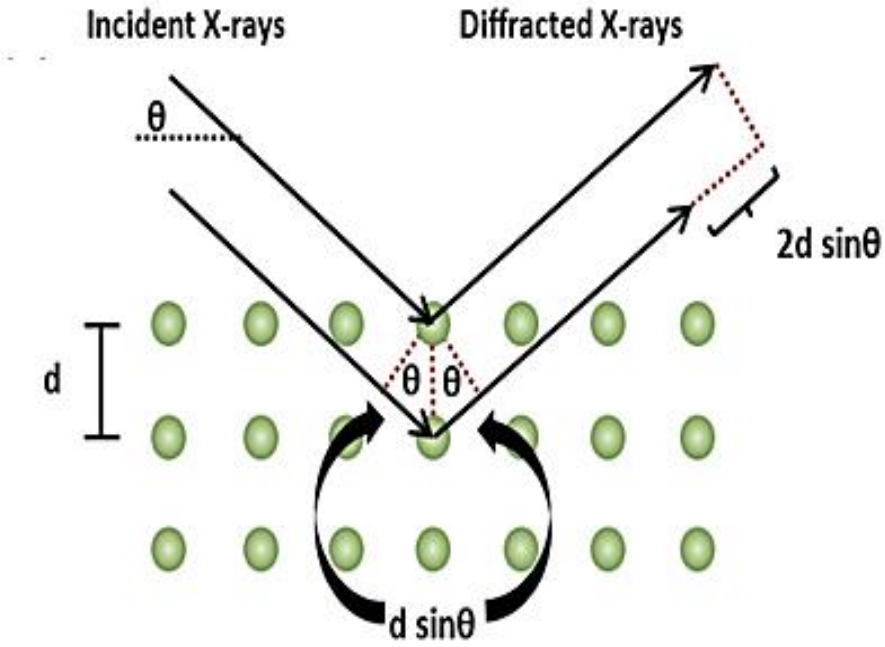

Figure IV. 3. XRD Principle.

IV.2.2.3 Fourier Transform Infrared (FTIR) spectroscopy

FTIR spectroscopy is a widely used technique for identifying functional groups in materials using infrared radiation beams. This characterization technique is rapid, accurate and sensitive. In FTIR analysis, samples are exposed to infrared (IR) radiation, the sample absorbs part of the IR radiation while transmitting some of it. The IR radiations impact then the molecular vibrations within the sample [96].

Before conducting IR spectroscopy study, 13 mm thin sample pellets were prepared by mixing about 150 mg of KBr powder with about 1 mg of sample, following that, the sample pellet is crushed and placed in a die for making pellets. A force of 12 tons is applied for a few minutes using an ICL manual hydraulic press to make a transparent sample pellet.

The principle of FT-IR spectroscopy working is detailed in Figure IV.4.

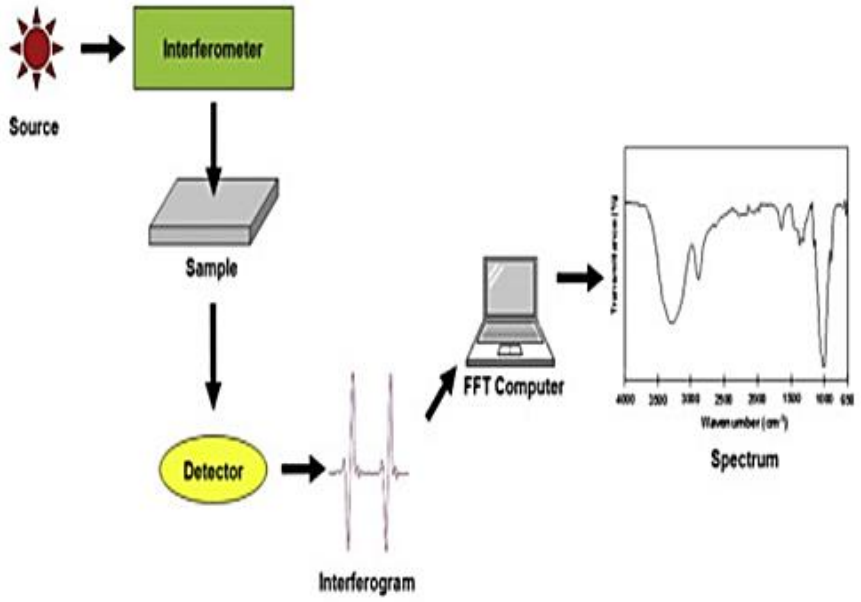

Figure IV. 4. FTIR working principle.

A Perkin-Elmer Fourier Transform infrared spectrometer was used to record the FTIR spectra of pure and Sb-doped Al_2O_3 for a field investigation of 4000-400 cm^{-1}.

IV.2.2.4 Scanning Electron Microscopy (SEM) and Energy Dispersive X-ray (EDX) spectroscopy analysis

SEM is a commonly used technique for scanning the surface of a specimen using a high electron beam energy released from an electron source. When the beam of electrons hits the specimen's surface, many signals are emitted. When processed, such signals can generate an image of the specimen. When SEM is coupled with an EDX detector, X-rays can also serve as a signal to provide elemental and chemical information about the specimen as shows Figure IV.5 [97].

The SEM-EDX analysis were conducted With a JEOL JSM-7001F device under an acceleration voltage ranging from 4 to 12 kV.

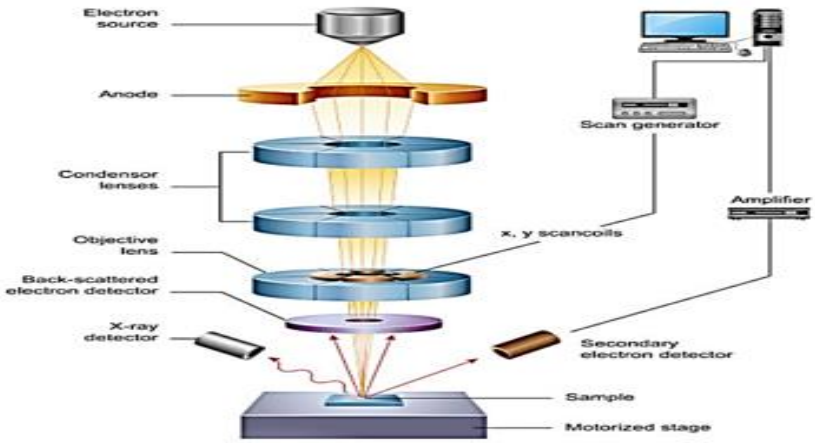

Figure IV. 5. Principle of SEM-EDX.

IV.2.3 TL and OSL signals reading

The Risø National Laboratory TL/OSL model DA-20 luminescence reader was used, which consists of three main parts shown in Figure IV.6 [98, 99]:

1) Light detecting system
2) Thermal and optical luminescence stimulation system
3) In situ irradiation sources: beta ($^{90}Sr/^{90}Y$), alpha (^{241}Am) and X-rays (50 kV/1 mA filament tube).

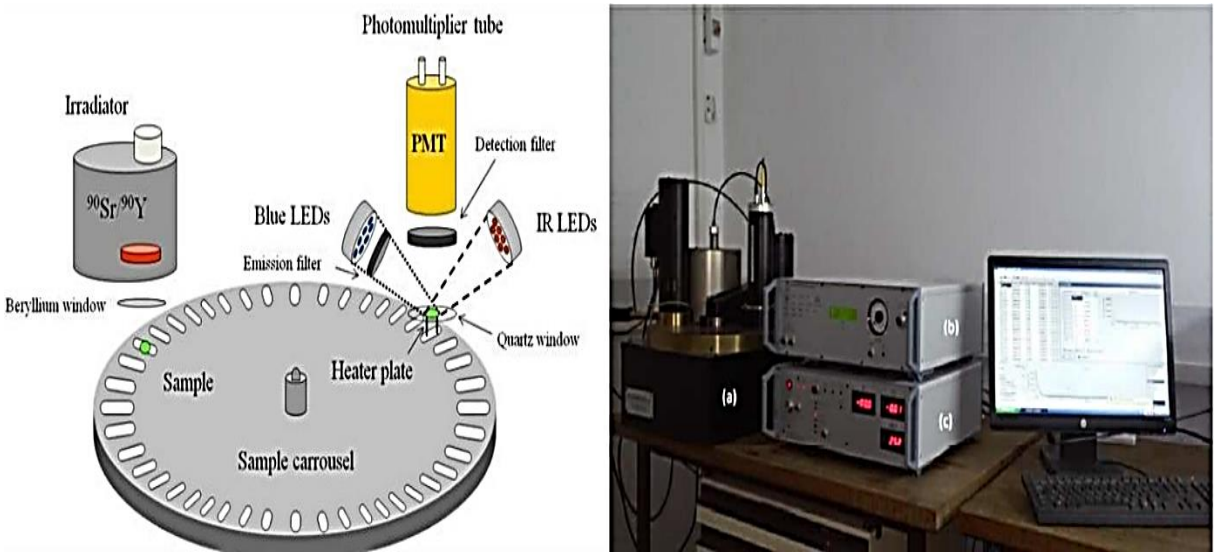

Figure IV. 6. TL/OSL equipment (left) and Risø TL/OSL reader (right), (a) reader, (b) controller, (c) X-ray generator controller.

Table IV. 1. Risø TL/OSL reader main characteristics.

Photomultiplier	CsSb crystal with a maximum detection efficiency of 200 to 400 nm and solid detection angle of 0.4 sr.
Blue Leds	NICHIA type NSPB-500AS with 470 nm peak emission and total power of 80 mW/cm^2.
Heater plate	Kanthal material with 700°C maximum temperature and from 0.1 to 10°C/s heating rates.
X-rays generator	Varian VF-50J X-ray tube (50 kV, 1 mA) with a tungsten target.
Sample holder	Stainless steel discs and cups of 5 mm diameter.

The different characteristics of Risø TL/OSL reader are tabulated in Table IV.1.

TL measurements were conducted between 0-450 °C at a linear heating rate of 5 °C/s. OSL measurements were carried out for a stimulation time of 500 s using blue LEDs with a 470 nm wavelength and continuous-wave stimulation mode (CW-OSL).

The dose-response was investigated under X-ray irradiation using dose ranges of 6-80 Gy for both TL and OSL dosimetry. Linear regression was used on obtained data for line of best fit calculating.

The R-squared, a statistic generally used to assess the linearity behavior of TL and OSL dose responses.

For energy dependence checking of the elaborated dosimeter, $Al_2O_3:Sb_{1\%}$ samples were exposed to an X-ray dose of 10 Gy from different sources supplying maximum energies ranging from 5 keV to 18 MeV. After exposure, the obtained TL signals were compared in terms of intensity. After exposure, the collected intensities of TL signals were compared.

IV.3 Elaboration of pure and Sb-doped Al_2O_3 nanoparticles

IV.3.1 Raw materials

Table IV.2 presents the raw materials used in course of this work for pure Al_2O_3 and Sb-doped Al_2O_3.

Table IV. 2. Raw materials used for the elaboration of pure and Sb-doped Al_2O_3

Product	Molecular formula	Purity %	Origin
Aluminium chloride hexahydrate (ACH)	$AlCl_3.6H_2O$	99%	Sigma Aldrich, USA
Citric acid monohydrate (CA)	$C_6H_8O_7.H_2O$	99.5%	Sigma Aldrich, USA
Antimony chloride	$SbCl_3$	99%	Sigma Aldrich, USA
Diethanolamine (DEA)	$C_4H_{11}NO_2$	99%	Sigma Aldrich, USA
Distilled water	H_2O	99.9%	GFL 2104 Double distillation water unit L-DAC

IV.3.2 Samples preparation

For a pure Al_2O_3 preparation, 4.828 g of ACH was dissolved in 100 ml of distilled water to obtain 0.2 M. The mixture was kept at room temperature with continuous magnetic stirring. Once ACH was dissolved, 4.203 g of CA was added as a chelating agent to ensure the mixing of cations at the molecular level. Solution stabilization was ensured by adding a few drops (2-3) of DEA under continuous magnetic stirring. The solution was kept at 80 °C for 1 h. The mixture was then heated at 120 °C for 1 hour while stirring to produce a transluscent viscous

gel. The produced gel was then heat-treated at 200 °C for 4 h until completely dried. The obtained powder was crushed using a mortar and pestle, followed by annealing at 1100°C for 6 h. For a 1 wt% ratio of [Al/Sb], 0.01 g of $SbCl_3$ was poured into the beaker separately until the precursor was dissolved for Sb-doped Al_2O_3 preparation. The prepared Sb-doping solution was added to the pure Al_2O_3 solution under the same elaboration conditions. The steps involving the synthesis of Al_2O_3 and Sb-doped Al_2O_3 are shown in Figure IV.7.

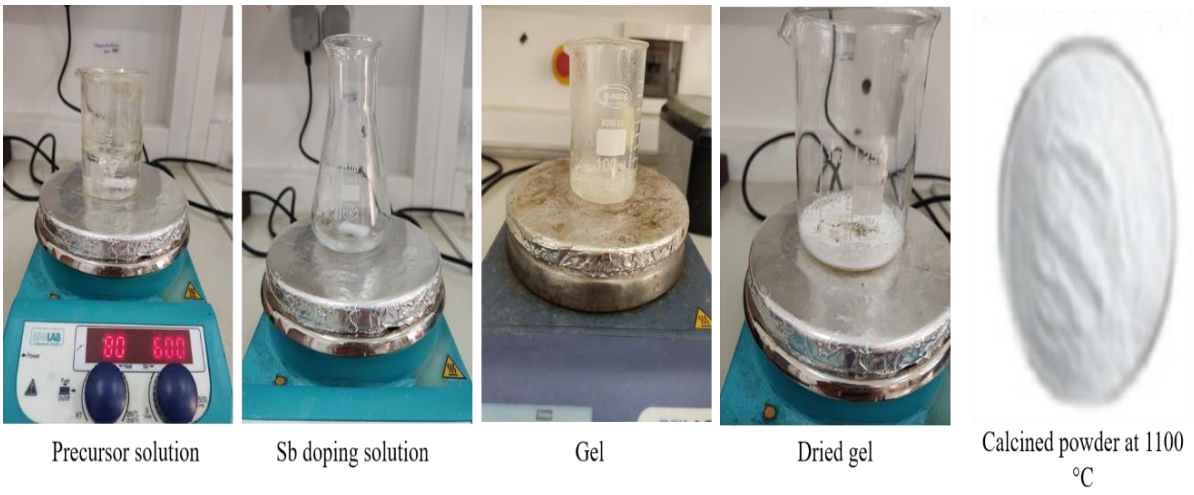

Figure IV. 7. Sol-gel synthesis of Al_2O_3 :Sb.

IV.4 Samples characterization

IV.4.1 TGA-DTG analysis

The TGA-DTG curves of amorphous Al_2O_3 powder are shown in Figure IV.8. In the temperature range RT-160 °C, a peak with a weight loss of 10.8 % at 135 °C appears, which is attributed to physically bound absorbed water removal. An intense peak, with a weight loss about 21.6 % appears at 215 °C in 160–320 °C temperature range indicating the DEA gradual evaporation since its boiling point is at 268 °C [100]. Two pics appear with a loss in weight ~ 33.7 % in temperatures ranging from 320 to 540 °C, the first sharp peak at 394 °C that may be associated to α-C-OH citric acid bond breaking up [101]. The second pronounced slope peak located at 470 °C that can be attributed to chloride groups decomposition [102]. In 540-1070 °C temperature region, three events occur, with weight loss of 10.1 %, two events located at 880 and 930 °C corresponding to the transitions of amorphous Al_2O_3 to γ-Al_2O_3 and γ-Al_2O_3 to α-Al_2O_3, respectively. The third event at 1060 °C is due to α-Al_2O_3 nanocrystals growth [103, 104].

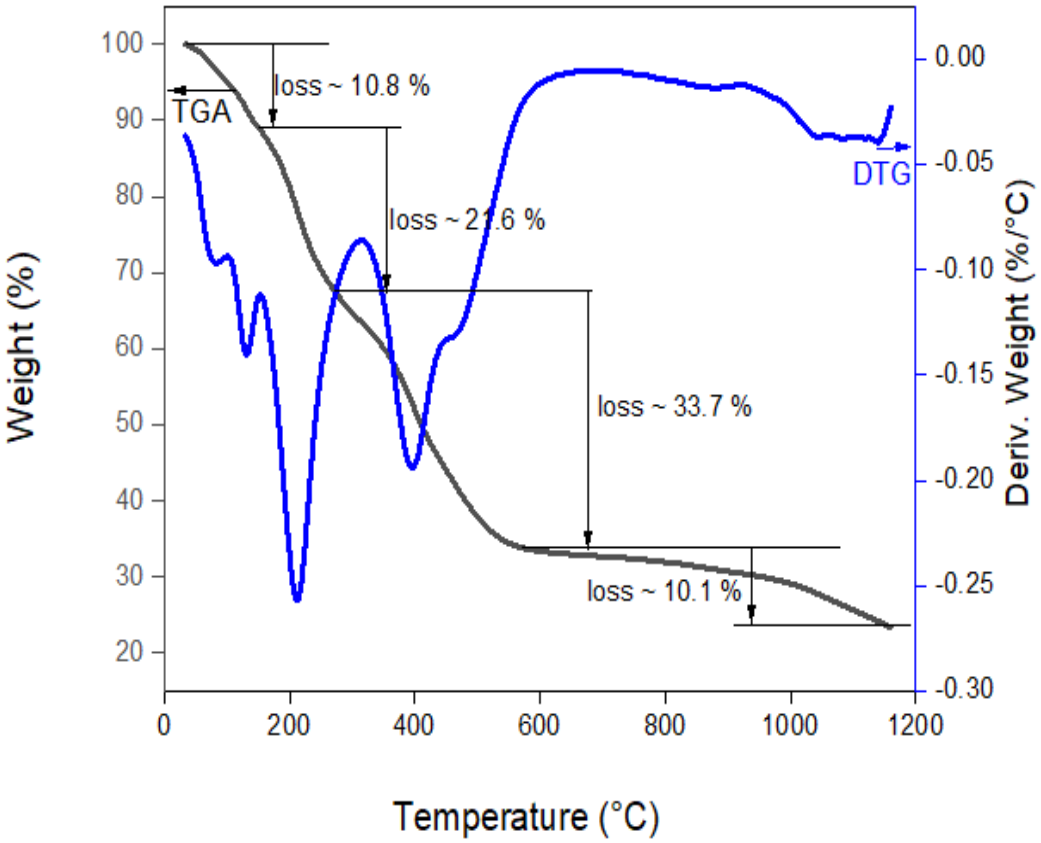

Figure IV. 8. TGA and DTG analysis curve of amorphous Al_2O_3.

IV.4.2 XRD analysis

The XRD patterns of pure and 1% Sb-doped Al_2O_3 are shown in Figure IV.9. Main diffraction peaks were observed at 2θ angle degrees of 25.68°, 35.30°, 37.93°, 43.54°, 52.78°, 57.77°, 66.82°, 68.51°, and 77.29°, which corresponded to crystal planes of (012), (104), (110), (113), (024), (116), (214), (300), and (1010), respectively. These peaks may be indexed to the rhombohedral structure of the α-Al_2O_3 phase (ICSD file No. 01-071-1127), with a = b = 4.7406 Å and c = 12.9326 Å unit cell parameters. The α-Al_2O_3 phase remains unchanged, and no additional peaks indicating the presence of a secondary phase have been observed. The Sb ions' low concentration is incorporated and uniformly dispersed into the host matrix of Al_2O_3 with calculated unit cell parameters a = b = 4.74058 Å and c = 12.936258 Å. No change was observed in the lattice dimensions, which implies that the Al atoms (1.18 Å) have been substituted by the Sb atoms (1.33 Å).

The average crystallite size was determined using Eq.(IV.1) and was about 44 and 39 nm for pure and Sb-doped Al_2O_3, respectively.

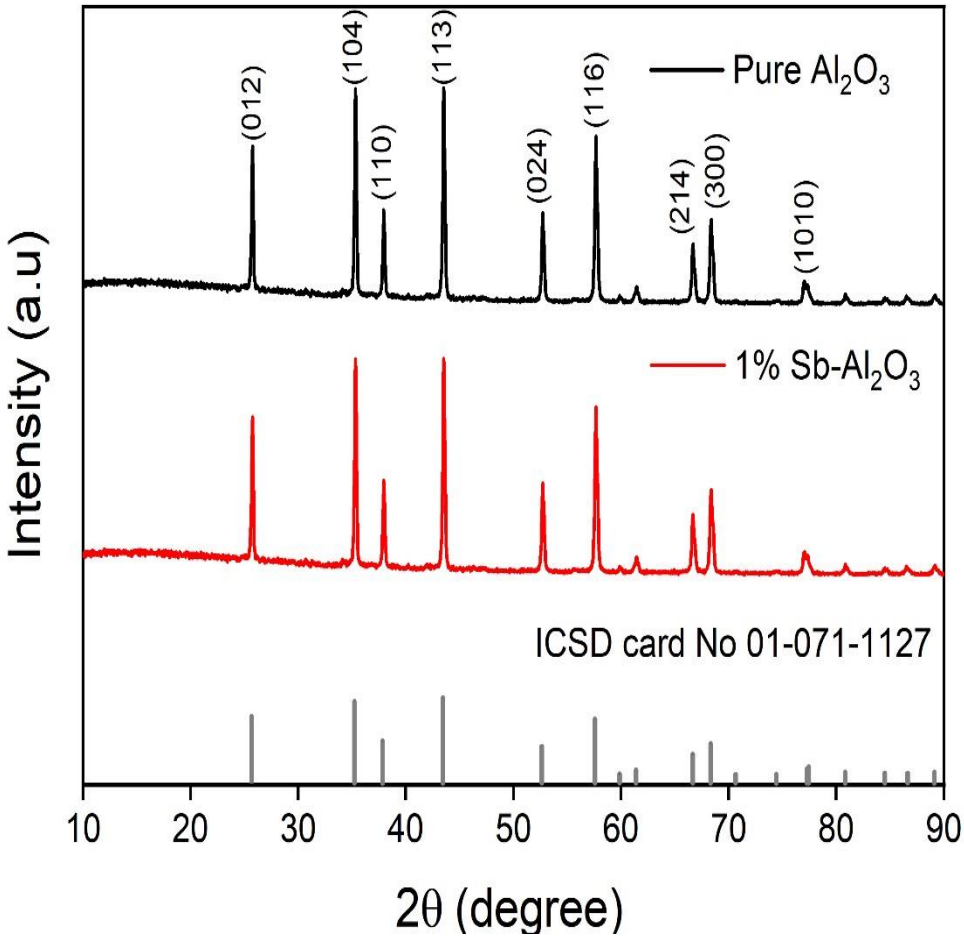

Figure IV.9. XRD patterns of pure, Al_2O_3:$Sb_{1\%}$ and ICSD card No.01-071-1127.

IV.4.3 FTIR analysis

The FTIR analysis of pure and Sb-doped Al_2O_3 is shown in Figure IV.10. The observed absorption band in the wavelength region 3520-3340 cm^{-1} that is related to the stretching bonds of O-H [105]. The absorption band at 2960 cm^{-1} belongs to the C-H stretching bond [105, 106]. The 1290 cm^{-1} absorption band is associated with bending and stretching vibrational modes of Al–O. The absorption bands at ~750 and 510 cm^{-1} correspond to the octahedral and tetrahedral groups of Al_2O_3 [107], respectively. The 1% Sb-Al_2O_3 FT-IR spectrum reveals absorption bands at ~1030 and 730 cm^{-1}, indicating the existence of Sb-O bonds [108]. The absorption band at 445 cm^{-1} corresponds to the AlO_4 tetrahedral sites [109]. The presence of Sb dopant reduces the intensity of the octahedral and tetrahedral Al_2O_3 groups. Sb doping influences the intensity of O-H and C-H stretching bonds.

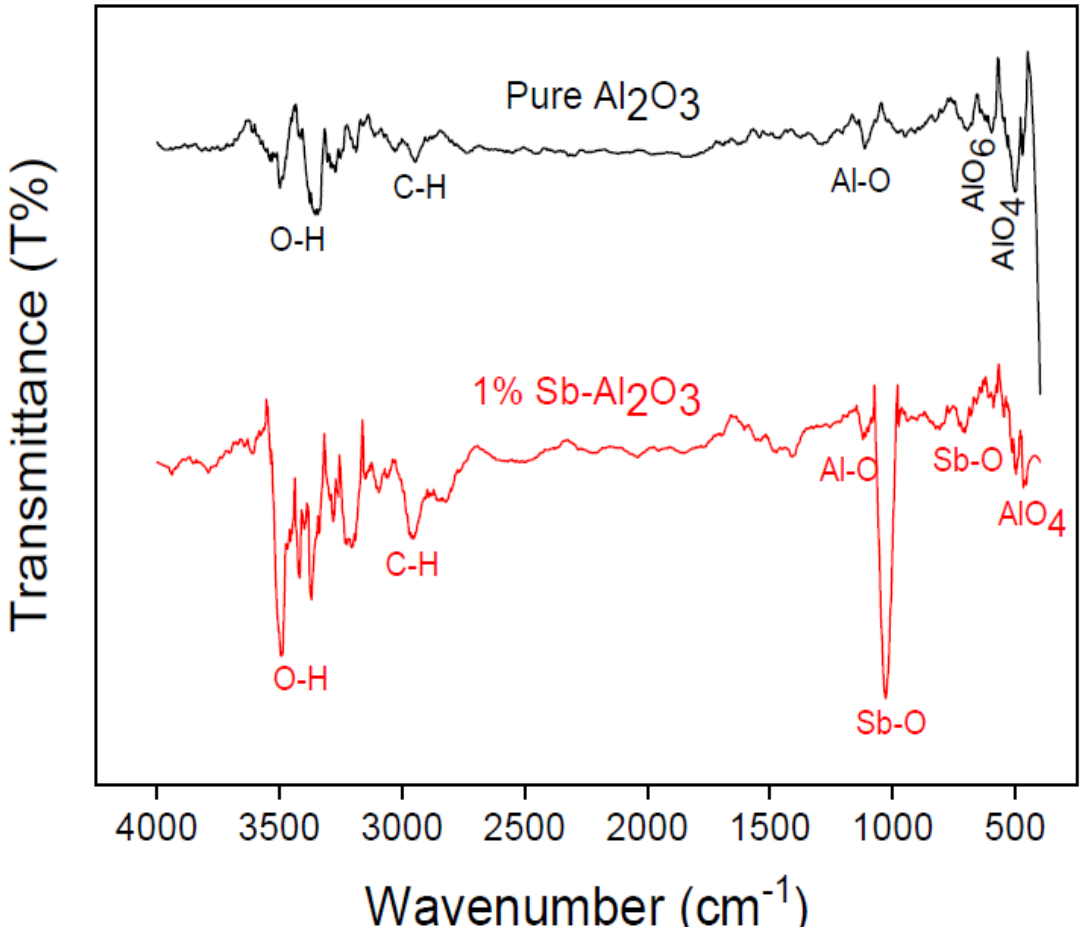

Figure IV.10. Pure and 1% Sb-doped Al_2O_3 FTIR analysis.

IV.4.4 SEM-EDX analysis

SEM images of pure and 1% Sb-doped Al_2O_3 are shown in Figure IV.11. Figure IV.11a shows a non-uniform distribution of particles with a packed structure consisting of small crystals of varied shapes and sizes separated by voids between grains. Sb doping did not affect the Al_2O_3 morphology. This can be due to the low concentration of Sb (1 wt%). The pure and Sb-doped samples had the same shapes and sizes Figure IV.11b. EDX analysis detected and confirmed the presence of Sb dopant. The amount of major elements was determined and was found 53.05 wt% for Al and 38.04 wt% for O in the Sb-doped Al_2O_3 sample. The Sb amount was found to be ~1,30 wt %. Other elements are detected as traces can be correlated with their existence in the source of precursors.

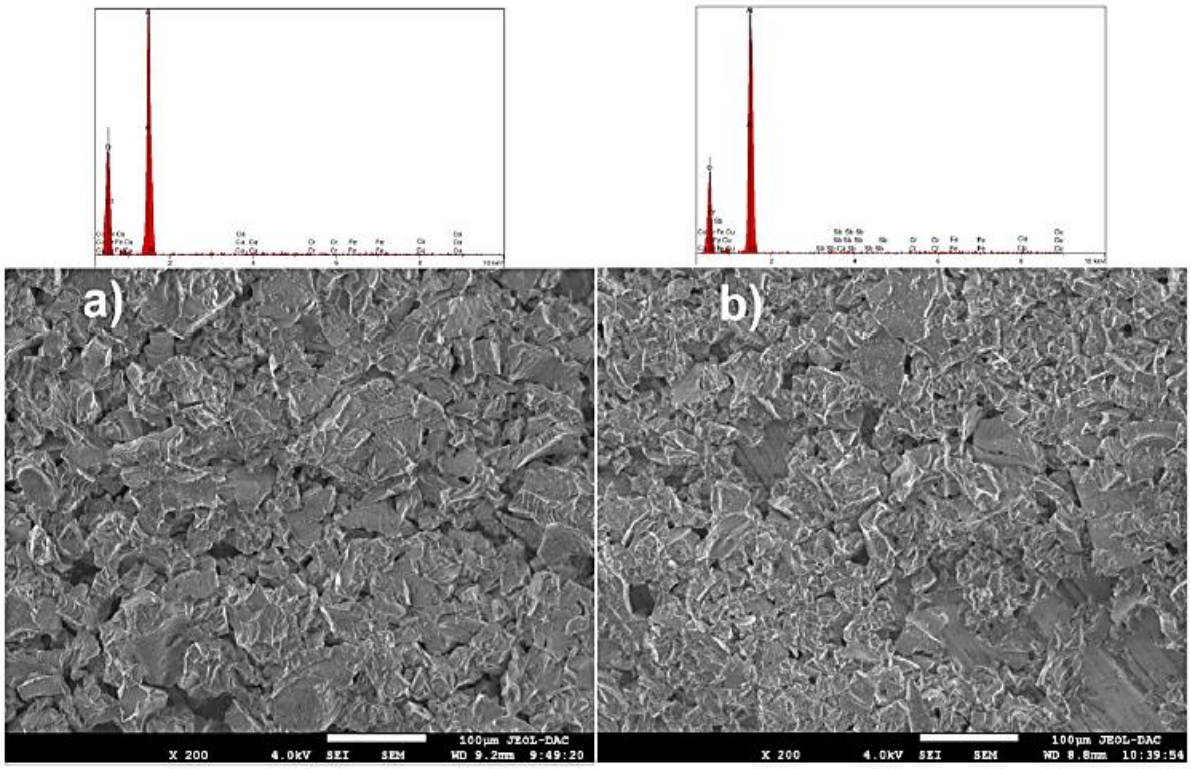

Figure IV.11. (a) Al_2O_3 and (b) Al_2O_3 :$Sb_{1\%}$ SEM-EDX results.

IV.5 TL and OSL study of α-Al_2O_3 detector

The TL glow curves of both undoped and 1% Sb-doped Al_2O_3 detectors exposed to 10 Gy X-rays dose at 5 °C/s linear heating rate are shown in Figure IV.12a. The undoped and 1% Sb-doped Al_2O_3 detectors show two peaks, the first is at ~83 °C for both samples wherease the second is around 230 °C for the pure sample and about 207 °C for 1% Sb-doped Al_2O_3 sample. The second peak is a dosimetric peak [110]. The first peak ~83°C is relatively unstable and may fade over time after radiation exposure [111, 112]. The Al_2O_3:$Sb_{1\%}$ sample total TL intensity was compared to the undoped one and was found to be four times higher when only considering the dosimetry peak and ten times higher when the full TL signal is considered. Figure IV.12b depicts the OSL signals of undoped and 1% Sb-Al_2O_3 detectors exposed to an X-ray dose of 10 Gy. As can be observed, the OSL signal of pure Al_2O_3 decays faster than Al_2O_3:$Sb_{1\%}$. In comparison to pure Al_2O_3, the 1% Sb-doped Al_2O_3 total OSL intensity was nine times higher.

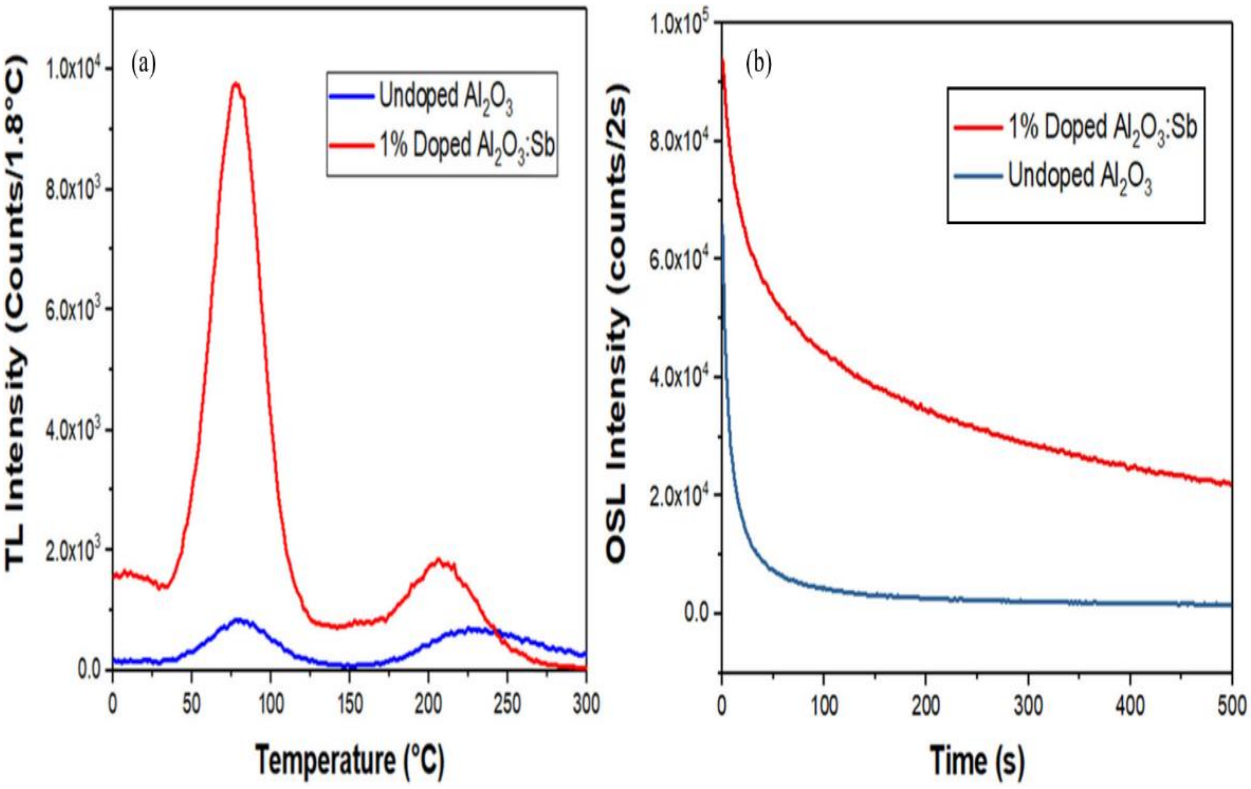

Figure IV. 12. (a) TL and (b) OSLsignals of undoped and Sb-doped Al_2O_3 for 10 Gy X-rays dose.

The addition of Sb dopant enhances the Al_2O_3 TL and OSL features, resulting in a higher ionizing radiation exposure sensitivity, allowing optimal use for dosimetry applications [113].

The incorporation of Sb ions and the growth of Al_2O_3 crystals improved the Al_2O_3 TL and OSL properties. The higher TL and OSL intensities reported for the Al_2O_3:Sb in both TL and OSL can be related to the induced oxygen vacancies (F centers) near the Sb^{3+} substitution in Al^{3+} in the matrix of Al_2O_3. It might also be attributed to the trapping of ionized electrons from F centers and Sb^{3+} ions in the host matrix. These ionized electron emitters (F centers and Sb^{3+} ions) serve as electron donors. When the dosimeter is thermally or optically stimulated, trapped electrons inside the Al_2O_3 lattice are released by F centers and Sb^{3+} ions as given below [114-116] :

F centers:

$$F \rightarrow F^+ + e^- \rightarrow F^* \quad \text{(IV.3)}$$

$$F^* + Sb^{3+} \rightarrow F + (Sb^{3+})^* \rightarrow F + Sb^{3+} + h\nu \quad \text{(IV.4)}$$

Sb^{3+} ions:

$$Sb^{3+} \rightarrow Sb^{5+} + 2e^{-} \quad \text{(IV.5)}$$

$$Sb^{5+} + 2e^{-} \rightarrow (Sb^{3+})^{*} \rightarrow Sb^{3+} + h\nu \quad \text{(IV.6)}$$

IV.5.1 TL&OSL dose-response

Figure IV.13 depicts the TL glow curves of the Al_2O_3:Sb sample after X-ray irradiation with different doses 6 Gy-80 Gy. Figure IV.13a depicts the OSL decay curves of the Al_2O_3:Sb sample irradiated with X-ray source with different doses 6 Gy-80 Gy and recorded at 500 s. As can be seen, the shape of OSL curves depends upon the delivered doses. The OSL curve of 6 Gy irradiated detector decays much faster than that of 80 Gy irradiated detector. Figure IV.13b reveals an increase in the TL intensity of the Al_2O_3:Sb sample as the delivered dose increases. The total TL intensity recorded from the 80 Gy irradiated Al_2O_3:Sb was about 18 times higher than that of the 6 Gy.

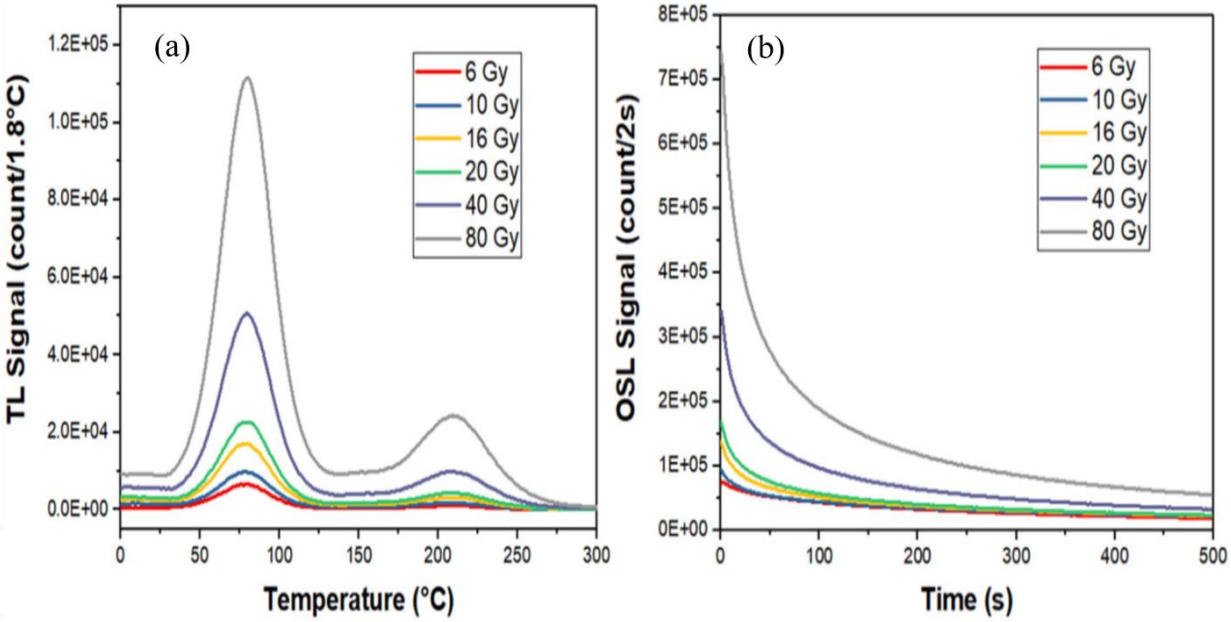

Figure IV. 13. (a) OSL and (b) TL curves of Al_2O_3:Sb for different doses.

Plotting the TL and OSL integral intensities vs the delivered dose yielded the TL and OSL dose-response curves of Al_2O_3:Sb detector in the dose range of 6-80 Gy using an X-ray source. Standard linear regression was used to fit the provided data. Figure IV.14 shows the performed linear fit R-squared values as: 0.9974 (TL) and 0.9975 (OSL). These results imply that the responses exhibit linear behaviour across the considered dose range.

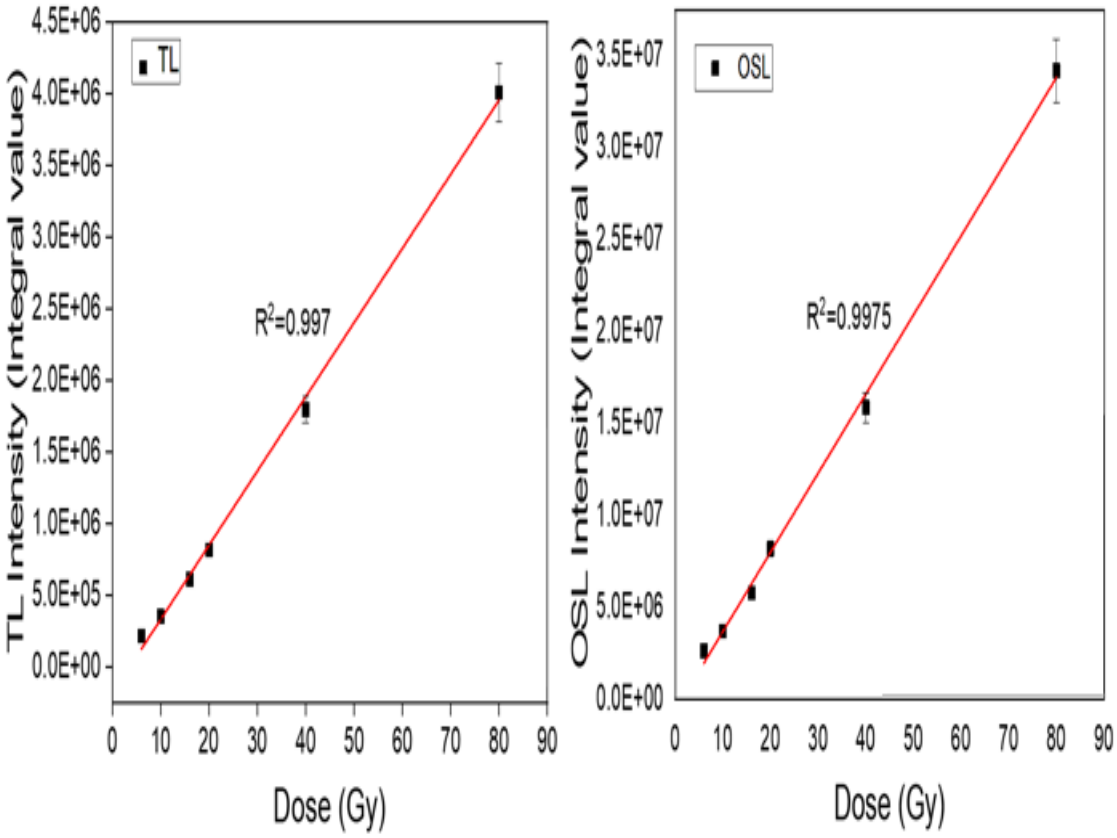

Figure IV. 14. (left) TL and (right) OSL responses of Al_2O_3:Sb to dose.

Repeatability tests for 10 Gy dose measurement, show standard deviations of 4.4% (TL) and 2.8% (OSL). The elaborated $Al_2O_3:Sb_{1\%}$ dosimeter produces the same TL integral intensity of about 10^6 counts as the commercially available Al_2O_3:C TL dosimeter for 10 Gy X-ray [117].

IV.5.2 Energy dependence of TL response

As shown in Figure IV.15, the $Al_2O_3:Sb_{1\%}$ detector exposed to 10 Gy indicated an energy dependence from 5 to 80 keV of low X-ray energies. In the megavoltage region, the TL intensity determined from signals corresponding to 10 Gy shows insignificant energy dependence, allowing effective use of the developed TL-OSL Al_2O_3 material for high energy and high radiation detection and dosimetry.

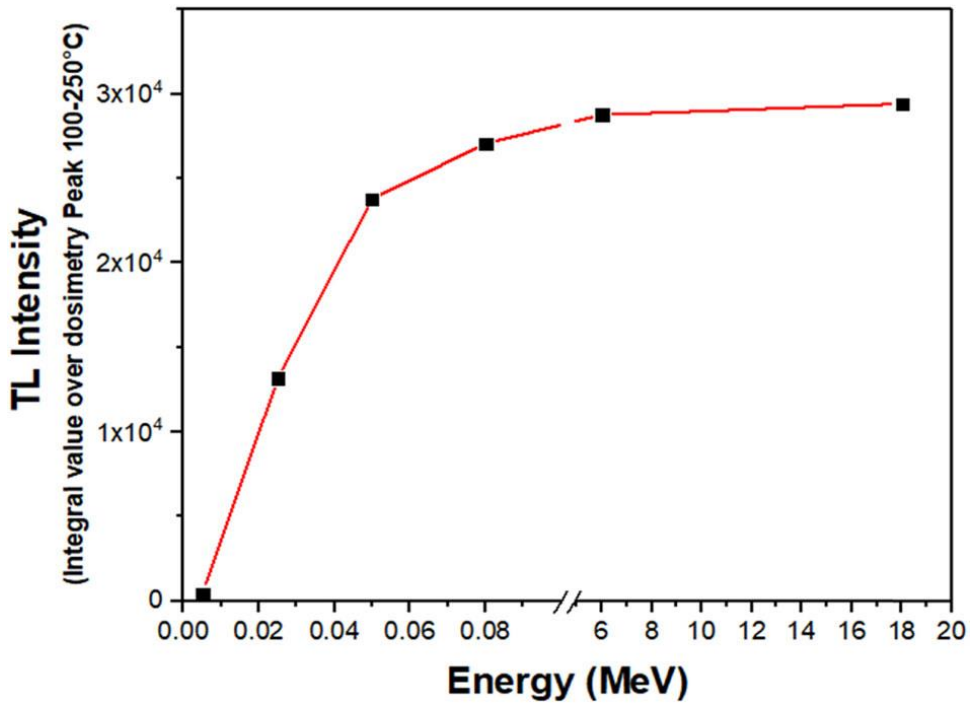

Figure IV. 15. Energy dependence of $Al_2O_3:Sb_{1\%}$ TL/OSL dosimeter showing insignificant dependence in the megavoltage region for an exposure to 10 Gy X-ray dose.

The as-prepared dosimeter exhibits appropriate OSL and TL radiation dosimetry features, such as adequate OSL decay and TL glow curves and good linearity dose response. The cheap and efficient elaborated Al_2O_3:Sb (1%) TL&OSL material for dosimetry presents also dosimetry properties the same performance capabilities as commercial Al_2O_3:C, such as main dosimetric peak around 200°C, linear dose-response, dependence upon energy[117].

CHAPTER V

Kinetic and dose-response study of BeO_R TL&OSL dosimeter

V.1 Objective

Despite BeO's promising properties in radiation dosimetry, a deeper understanding of its TL and OSL mechanisms in terms of trapping parameters is primordial.

In this work, a study was conducted on a developed new type of beryllium-oxide dosimeter BeO_R manufactured by a Turkish company. The results of the TL glow curves analysis of X-ray irradiated BeO by three different TL trapping parameters determination methods, namely: Chen peak shape, FOK-Glow-Fit, and GOK-CGCD using updated formulations and approaches were reported. The OSL kinetics parameters were also determined based on the results of TL kinetics characterization. The dosimeter's behaviour towards the delivered dose was studied and established for TL and OSL X-ray dose within a range of 2-10 Gy. The contribution of this study aims to establish and compare the developed BeO_R dosimeter's kinetic parameters and its relevance for dose monitoring in photon (X-ray) radiotherapy.

V.2 Material and methods

V.2.1 Dosimeter description

BeO ceramics dosimeter in square shape of dimensions and weight of $4 \times 4 \times 1$ mm^3 and 32 mg, respectively was used to perform the study. The studied dosimeter is purchased from a private Turkish company [118, 119].

V.2.2 TL and OSL measurements

The TL measurements were performed using a Risø TL/OSL-DA-20 reader (Risø National Laboratory, Denmark) coupled with a Varian VF-50J (50 kV/1 mA) X-ray unit and a bialkali EMI 9235QB PM tube with a maximum detection efficiency of 200-400 nm. TL measurements were taken in the N_2 atmosphere at a linear heating rate of 5 °C/s in the temperature range 0-480 °C.

The OSL measurements were recorded at 500 s using blue LEDs and continuous-wave stimulation (CW-OSL) mode.

V.3 TL glow curve deconvolution and kinetics study

V.3.1 First-order kinetics TL deconvolution method using Glow-Fit

Based on the assumption of the Randall-Wilkins model for first-order kinetics, the TL glow curve is decomposed into individual components.

An isolated glow peak's TL intensity is provided by Eq.(V.1) :

$$I(T) = I_m exp\left(\frac{E}{kT_m} - \frac{E}{kT}\right) exp\left(-\frac{E}{kT_m^2}\int_{T_m}^{T} \exp\left(\frac{E}{kT_m} - \frac{E}{kT'}\right) dT'\right) \quad \text{(V.1)}$$

where I is the glow peak intensity, k is the Boltzmann constant, T is the absolute temperature, T_m and I_m are the temperature and intensity of the maximum, respectively.

Since the exponential integral of Eq.(V.1) cannot be solved analytically, several approximations and functions describing a single glow peak have been discussed [31]. For Glow-Fit [120], the exponential integral is approximated by [121, 122]:

$$\int_0^T exp\left(-\frac{E}{kT'}\right) dT' \approx \frac{E}{k}\int_x^{\infty} (x')^{-2} exp(-x') dx' = \frac{E}{k}\frac{1}{x}E_2(x) \quad \text{(V.2)}$$

where $x = {}^{E}/_{kT}$, $x' = {}^{E}/_{kT'}$, and $E_2(x)$ may be evaluated by $E_2(x) = \alpha(x)\exp(-x)$, where $\alpha(x)$ is a 4th order polynomial quotient [121]:

$$\alpha(x) = 1 - \frac{a_0 + a_1 x + a_2 x^2 + a_3 x^3 + a_4 x^4}{b_0 + b_1 x + b_2 x^2 + b_3 x^3 + b_4 x^4} \quad \text{(V.3)}$$

Finally, the TL glow peak is described as below [31]:

$$I(T) = I_m\ exp\left(\frac{E}{kT_m} - \frac{E}{kT}\right) exp\left(\frac{E}{kT_m}\left(\alpha\left(\frac{E}{kT_m}\right) - \frac{T}{T_m} exp\left(\frac{E}{kT_m} - \frac{E}{kT}\right)\alpha\left(\frac{E}{kT}\right)\right)\right) \quad \text{(V.4)}$$

According to this equation, the glow curve is a nonlinear function of I_m, $T_m$and E parameters. To find the best-fit values for peak parameters, a series of iterations must be used. Glow-Fit can deconvolve up to 10 glow peaks from the TL glow curve at the same time. The Levenberg-Marquardt algorithm was adopted for nonlinear function minimization. The original algorithms modified to exclude or constrain any given peaks parameter, allowing the user to control the fitting peak parameters [120]. The quality of the applied fit was controlled by the Figure Of Merit (FOM) [123] provided by Eq.(V.5) :

$$FOM = \sum_i \frac{|Y_{exp} - Y_{fit}|}{A} \quad \text{(V.5)}$$

Where: Y_{exp} and Y_{fit} are the experimental and fitted curve data points, and A is the area of the fitted curve. The open-source software "Glow-Fit" is used for the deconvolution task.

V.3.2 General-order kinetics TL deconvolution method using CGCD

The TL glow curve deconvolution was performed using Eq.(V.6) which obeys general-order kinetics (GOK) for TL given as follows:

$$I(T) = I_m . b^{\frac{b}{b-1}} . exp\left(\frac{E}{kT} . \frac{T-T_m}{T_m}\right) \times \left[(b-1).(1-\Delta).\frac{T^2}{T_m^2} . exp\left(\frac{E}{kT} . \frac{T-T_m}{T_m} + Z_m\right)\right]^{-\frac{b}{b-1}} \quad (V.6)$$

where *Im* is the maximum intensity, *b* is the order of kinetic, *Tm* is the maximum temperature of peak and $\Delta = \frac{2kT}{E}$, $Z_m = 1 + (b-1).\Delta_m$, $\Delta_m = \frac{2kT_m}{E}$.

The Figure of Merit (FOM) was used to control the goodness of the fit.

V.4 Results and discussion

V.4.1 Peak shape Chen's method

Figure V.1 depicts the TL glow curve of X-ray irradiated BeO_R for a dose of 6 Gy.

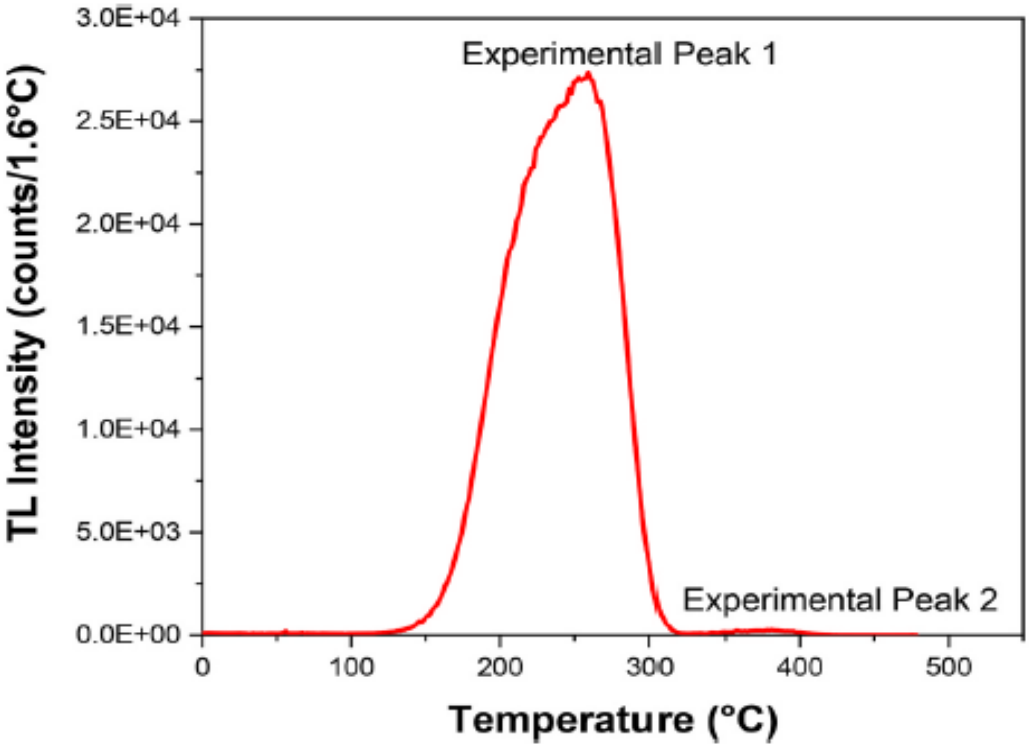

Figure V. 1. TL glow curve of 6 Gy X-ray irradiated BeO_R recorded at a linear heating rate of 5 °C/s.

The TL glow curve of BeO_R shows two experimental peaks located at ~250 ◦C and ~379 ◦C. The 250 °C is the dosimetry peak (peak1).

The peak shape method discussed in the section 3.3 of the chapter I was used. In the present work, the symmetry factor μ_g and the Balarian parameter $\gamma = \delta/\tau$ for the first peak were found to be 0.55 ± 0.01 and 1.24 ± 0.03 respectively, a kinetic order of about 2.5 according to μ_g factor, for the second peak, μ_g equals 0.44 ± 0.01, indicating a kinetic order of 1.1, and γ is equal to 0.79 ± 0.02 as tabulated Table V.1 [30]. The assumptions $b = 2$ for the first peak and $b = 1$ for the second peak were established based on these results.

Table V. 1. Chen and Balarian TL peak parameters.

Peak	**T_1** (°C)	**T_m** (°C)	**T_2** (°C)	**τ** (T_m-T_1)	**δ** (T_2-T_m)	**ω** (T_2-T_1)	**μg=δ/ω**	**γ= δ/τ**
First	211	248	294	37	46	83	0.55	1.24
Second	346	379	405	33	26	59	0.44	0.79

The activation energies were calculated using the following expressions:

$$E_\alpha = c_\alpha \left(\frac{kT_m^2}{\alpha}\right) + b_\alpha (2kT_m) \qquad \text{(V.7)}$$

where α is τ, δ or ω and the values of c_α and b_α can be summarized as:

$c_\tau = 1.51 + 3.0(\mu_g - 0.42)$ $\qquad$ $b_\tau = 1.58 + 4.2(\mu_g - 0.42)$

$c_\delta = 0.976 + 7.3(\mu_g - 0.42)$ $\qquad$ $b_\delta = 0$

$c_\omega = 2.52 + 10.2(\mu_g - 0.42)$ $\qquad$ $b_\omega = 1$

$\mu_g = 0.42$ $\qquad$ for first-order kinetics

$\mu_g = 0.52$ $\qquad$ for second-order kinetics

The obtained activation energies are $E_\tau = 1.01 \pm 0.05$ eV, $E_\delta = 0.98 \pm 0.03$ eV and $E_\omega = 0.99 \pm 0.02$ eV for the first peak and $E_\tau = 1.56 \pm 0.07$ eV, $E_\delta = 1.58 \pm 0.08$ eV and $E_\omega = 1.57 \pm 0.07$ eV for the second peak. The corresponding frequency factors were calculated by equation (V.8) for general-order kinetics at $b = 2.5$ and 1.1 for the first and second peaks, respectively.

$$s = \left(\frac{\beta}{T_m^2}\right)\left(\frac{E}{k}\right)\frac{1}{1+(b-1)\left(\frac{2kT_m}{E}\right)} exp\left(\frac{E}{kT_m}\right) \qquad \text{(V.8)}$$

The obtained frequency factor values for the first and second peaks are respectively $s_\tau = 1.1 \times 10^9$ s^{-1}, $s_\delta = 5.5 \times 10^8$ s^{-1} and $s_\omega = 7.0 \times 10^8$ s^{-1}; $s_\tau = 2.4 \times 10^{11}$ s^{-1}, $s_\delta = 3.4 \times 10^{11}$ s^{-1} and $s_\omega = 2.9 \times 10^{11}$ s^{-1}. The obtained results are in agreement with previous studies [124-126].

The PS method results are tabulated in Table V.2.

Table V. 2. Activation energies and frequency factors evaluated by the TL PS method.

	Peak 1	**Peak 2**	**Method**
E_{eff} **(eV)**	1.01 ± 0.05	1.56 ± 0.07	
s (s^{-1})	1.1×10^9	2.4×10^{11}	**Chen (τ)**
b	2.5	1.1	
E_{eff} **(eV)**	0.98 ± 0.03	1.58 ± 0.08	
s (s^{-1})	5.5×10^8	3.4×10^{11}	**Chen (δ)**
b	2.5	1.1	
E_{eff} **(eV)**	0.99 ± 0.02	1.57 ± 0.07	
s (s^{-1})	7.0×10^8	2.9×10^{11}	**Chen (ω)**
b	2.5	1.1	

V.4.2 First-order kinetics TL deconvolution method using Glow-Fit

The experimental TL glow curve was decomposed into three peaks (1(a), 1(b) and 1(c)) in the region of the recorded experimental peak 1 (150–300 °C) and one peak (2(a)) in the temperature interval 300–400 °C where the second experimental peak 2 is observed by applying TL deconvolution method using Glow-Fit. The activation energies for the first experimental peak range from 1.02 to 1.07 eV, while for the second experimental peak, it equals 1.94 eV.

The FOK-Glow-Fit method's deconvolution of TL glow curves yielded a figure of merit (FOM) of 1.62%, assuring good accuracy. Table V.3 presents main obtained TL kinetics parameters.

Chen's empirical method yields reliable values that are close to those provided by the Glow-Fit first-order kinetics TL deconvolution method.

Table V. 3 TL Kinetic parameters of BeO_R obtained by first-order deconvolution method using Glow-Fit.

	Peak 1(a)	**Peak 1(b)**	**Peak 1(c)**	**Peak 2(a)**
T(°C)	203.5	223.7	259.3	380.8
E(eV)	1.02	1.05	1.07	1.94
s(s^{-1})	1.43×10^{12}	2.0×10^{9}	2.3×10^{8}	2.9×10^{13}
b	1	1	1	1

V.4.3 General-order kinetics TL deconvolution method using CGCD

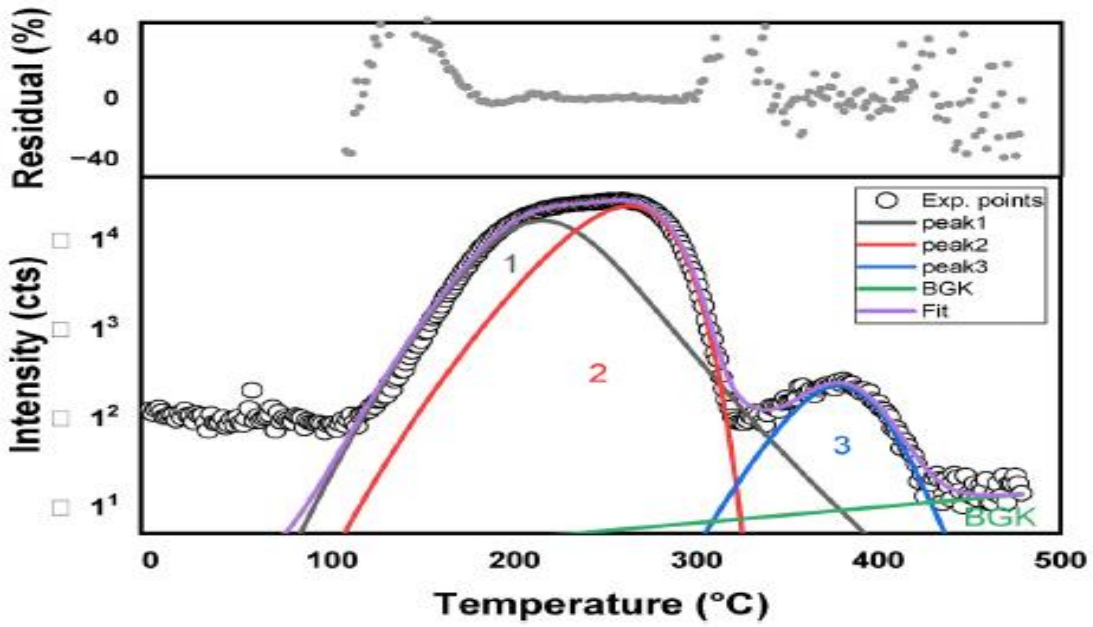

Figure V. 2. GOK-CGCD of 6 Gy irradiated BeO displaying experimental data, identified peaks, fit and residual patterns.

Figure V.2 depicts the deconvolution results of the 6 Gy X-ray irradiated TL glow curve of BeO_R. The experimental TL glow curve was decomposed into three peaks (1, 2 and 3) by applying GOK-CGCD deconvolution. The values of activation energies obtained are 1.04, 1.06 and 2.51 eV for these three (3) deconvoluted peaks.

Table V.4 presents the main obtained TL kinetics parameters.

Table V. 4. BeO_R TL Kinetic parameters obtained by general order kinetics (GOK) deconvolution method using CGCD.

	Peak 1	**Peak 2**	**Peak 3**
T(°C)	218	260	378
E(eV)	1.04	1.06	2.1
s(s^{-1})	1.44×10^{10}	1.56×10^{9}	1.7×10^{14}
b	2	1	2

The frequency factors estimated for the two observed experimental peaks for different obtained orders varied slightly for the different variants of PS method (τ, δ znd ω).

The relatively lower values of activation energy obtained by Chen's method for Peak1 is due to its asymmetry shape [127]. The results of the TL experimental peaks 1 and 2 deconvolution are in good agreement with those already published [128, 118].

V.4.4 OSL kinetics parameters

Since the TL signal of BeO_R includes two main perfectly separated peaks, and based on step annealing studies and using the above-described model and approach by Eq.(I.37) [118], we have opted to decompose the OSL signal of BeO into two components (OSL_1 for TL Peak 1(a) and OSL_2 for TL Peak 2(a)) by taking OSL background (Bk) into account.

The considered OSL kinetic model used can be given as:

$$I_{OSL} = I_{10}.\exp(-t/\tau_{d1}) + I_{20}.exp(-t/\tau_{d2}) + Bk \qquad (V.9)$$

Considering the fitting formula given by Eq.(V.10), the experimental OSL decay curve adjusted (fitted)

$$y = A_1 \exp\left(-\frac{x}{t1}\right) + A_2 \exp\left(-\frac{x}{t2}\right) + y_0 \qquad \text{(V.10)}$$

The most appropriate adjustment equation and the one closest to the experimental data are adopted after several iterations (Figure V.3).

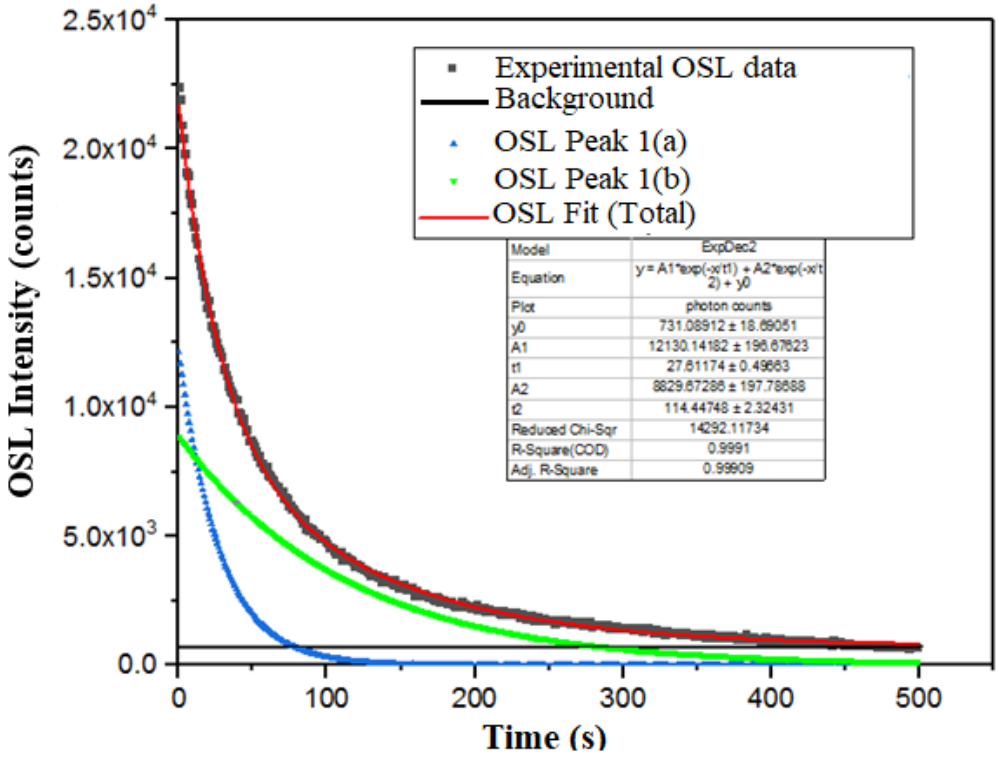

Figure V. 3. OSL signal deconvolution based on TL kinetics results by exploiting the main TL deconvolution peaks (peaks 1 and 2).

The performed OSL kinetics allow us to determine two interesting parameters: the electron de-trapping probabilities,pi ($pi = 1/\tau_i$), and the photoionization cross sections for the two OSL signal components OSL_1 and OSL_2, which are: 3.6×10^{-2} s^{-1} and 2.12×10^{-18} cm^2 for OSL_1 and 8.7×10^{-3} s^{-1} and 5.12×10^{-19} cm^2 for OSL_2.

The obtained results are in good agreement [118].

V.4.5 TL glow curves, OSL decay curves, and dose responses of BeO_R

Figure V.4 depicts the TL glow curves of BeO_R for different X-ray energies ranging from 2 to 10 Gy.

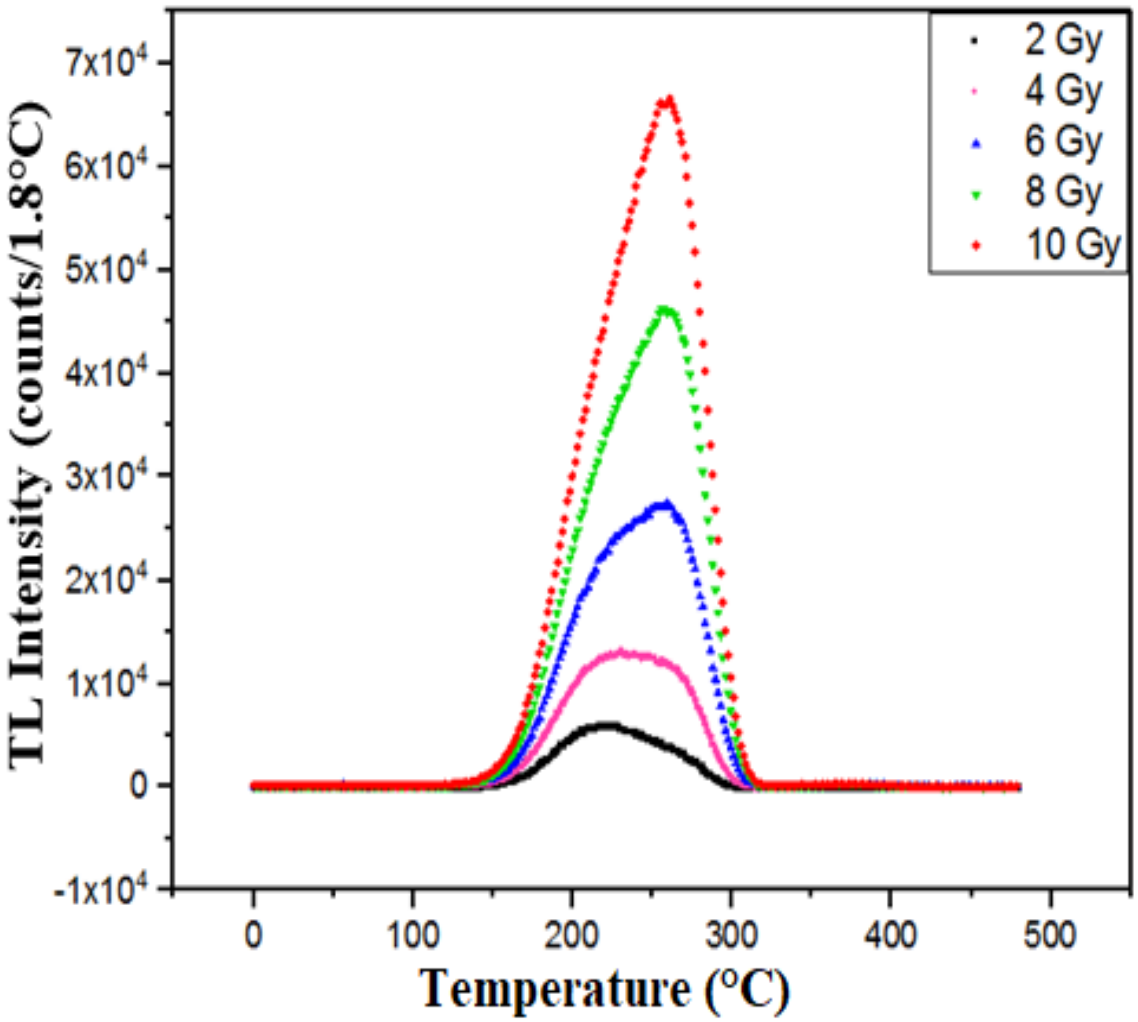

Figure V. 4. TL glow curves for different doses of BeO_R.

The established TL dose-response of BeO_R is depicted in Figure V.5. The TL intensities are obtained for dose response study by integrating the whole TL glow curves.

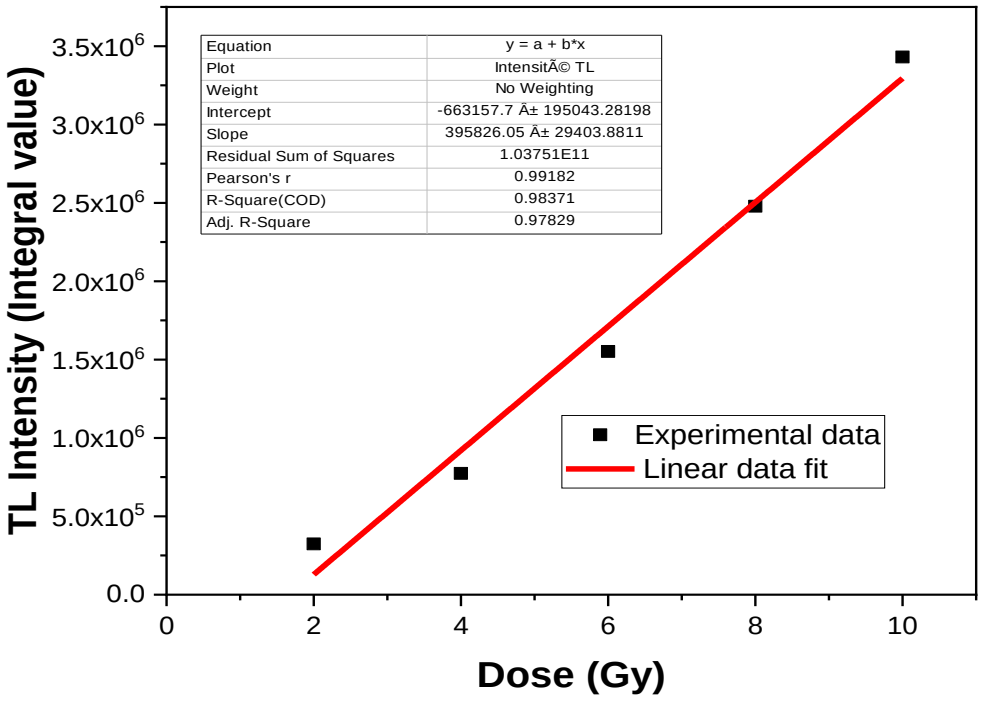

Figure V. 5. TL dose response curve of BeO_R.

Figure V.6. depicts the OSL decay curves of BeO_R for the same considered dose interval as the TL case.

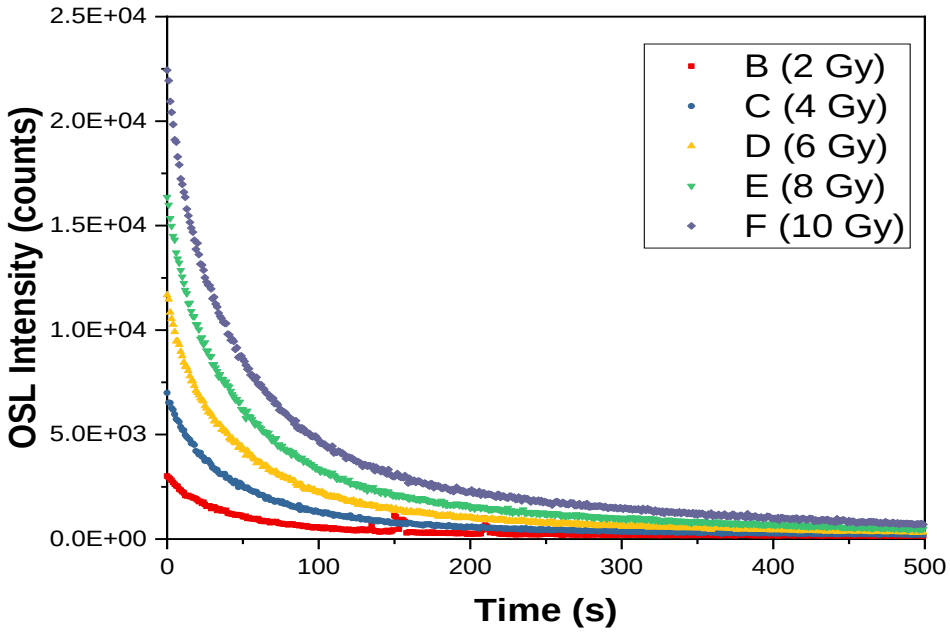

Figure V. 6. OSL decay curves for different doses of BeO_R.

The established OSL dose-response of BeO_R is depicted in Figure V.7.

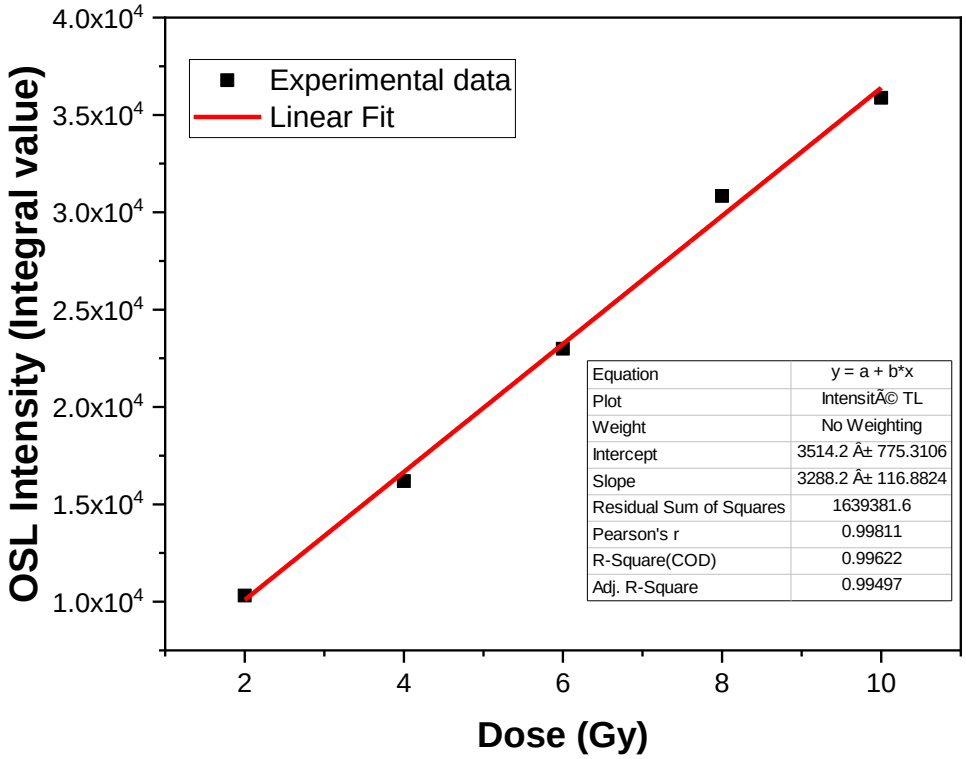

Figure V. 7. OSL dose response curve of BeO_R.

The established TL and OSL dose responses exhibit in both cases linear behaviour, allowing optimal use of the developed BeO_R for X-ray dosimetry purposes in the considered dose range.

Finally, based on the results of the TL and OSL kinetics studies, as well as the dose-response establishment for X-ray irradiation within the dose range of 2-10 Gy, the developed BeO_R dosimeter is suitable for dosimetry application, particularly for medium dose and high energy, as in photon radiotherapy.

General Conclusions and Outlook

In this thesis project, the intended conclusions involve two essential achievements. Indeed, it was the first time that α-Al_2O_3:Sb material has been synthesized by the Sol-Gel process and characterized for final use in TL&OSL radiation dosimetry. Thus, an optimal amount of Antimony (Sb) of about 1% was found to be most suitable to produce the best TL&OSL signals, dose-response, and sensitivity to ionizing radiation of the elaborated dosimeter. The as-prepared α-Al_2O_3:Sb Nano-powders were characterized by TGA, XRD, FTIR, SEM and EDX analysis techniques, showing the main differences in terms of loss in weight, crystalline structure, covalent bonding groups and morphology of pure and Sb-doped Al_2O_3. The TL experimental glow curves show two peaks recorded at a heating rate of 5 °C/s. The first was observed for pure and Sb-doped Al_2O_3 at 83 °C. The second peak was observed at ~230 °C for the undoped samples and around 207 °C for the doped ones. The second more stable peak can be used for radiation dosimetry purpose. The variation in TL-OSL intensity of Al_2O_3:$Sb_{1\%}$ exhibits a linear dependence to X-ray dose. Within the dose interval of 5-80 keV, Sb-doped Al_2O_3 was found to be energy dependent in X-ray irradiation. In the megavoltage region, low energy reliance was observed to X-ray energy. Therefore, it may be assumed that the as-synthesized 1% Sb-doped Al_2O_3 is more suitable for high-energy and high-dose radiation detection and dosimetry. Such prepared dosimeter exhibits suitable OSL and TL radiation dosimetry features, such as adequate TL glow and OSL decay curves and good linearity for the responses towards the delivered dose. The elaborated low-cost and efficient Al_2O_3:$Sb_{1\%}$ TL&OSL dosimetry material exhibits the same dosimetry performances and capabilities as the commercial Al_2O_3:C dosimeter.

Secondly, different methods were used to study the thermoluminescence and optically stimulated luminescence kinetics of a newly developed beryllium-oxide dosimeter (BeO_R) using various methods. The TL glow curves of BeO_R TL&OSL dosimeter show two experimental peaks recorded at ~250 ◦C and ~379 ◦C with a heating rate of 5 °C/s in case of X-ray irradiation within the dose interval of 2–10 Gy. TL and OSL kinetics parameters such as activation energy *E*, frequency factor *s*, kinetics order *b*, electron de-trapping probability *p*, and photoionization cross-section σ were estimated for the studied BeO_R dosimeter. Thus, three different methods have been employed for the TL glow curve deconvolution and analysis: the peak shape (Chen) method, FOK-GlowFit method, and GOK-CGCD method. The application of the peak shape method demonstrates a second and a first-order kinetics behavior of the first and second experimental peaks, respectively. The determined TL&OSL kinetics parameters by

the aforementioned methods were found to be closers and agree well with those of the already published literature on the same BeO_R dosimeter. Moreover, our work provides some new and updated data. The established TL and OSL dose responses show a linear behaviour allowing an effective use of the BeO_R dosimeter for dose assessment, particularly, in external photon radiotherapy.

The performance of Al_2O_3 raw material can be enhanced in radiation detection and dosimetry by doping or co-doping with other elements possessing good luminescent properties, study the sintering temperature effect on its crystalline structure and study its response towards X-ray irradiation. The as-elaborated dosimeters can be used in different dosimetry fields, including: personnel, medical and environmental.

References

[1] D. Adlienė, & R. Adlytė (2017). Dosimetry principles, dose measurements and radiation protection. In: Applications of ionizing radiation in materials processing, Y. Sun and A.G. Chmielewsk. Institute of Nuclear Chemistry and Technology, Warszawa.

[2] E.G. Yukihara, E.D. Milliken, I.C. Oliveira, V.R. Orante-Barrón, I.G. Jacobsohn & M.W. Blair (2011). Systematic development of new thermoluminescence and optically stimulated luminescence materials. Journal of Luminescence 133 : 203-210.

[3] R. Chen & V. Pagonis (2011). Thermally and optically stimulated luminescence: A stimulation approach, 1st ed. John Wiley & Sons.

[4] G. Blasse & B.C. Grabmaier (1994). A general introduction to luminescent materials. In: Luminescent materials, Springer, Berlin, Heidelberg.

[5] L.H. Brixner (1980). On the structural and luminescent properties of the $ScTa_{1-X}Nb_xO_4$ system. Journal of Chemical Education 57 : 588-590.

[6] K.S. Pau (2013). Thermoluminescence studies of naturally occuring salts relevent to dosimetry obtained from Mizoram. Ph.D. Thesis, Dept. Phys., Mizoram Univ., India.

[7] B. Valeur & M.N. Berberan-Santos (2012). Introduction. In Molecular fluorescence: principles and applications. Wiley-VCH Verlag GmbH & Co. KGaA.

[8] V.P. Gribkovskii (1998). Theory of Luminescence. In: Luminescence of Solids, D.R. Vij, Eds. Springer, Boston, MA.

[9] S.W.S. Mckeever (1985). Thermoluminescence of solids, 1st ed. Cambridge University Press.

[10] F. Daniels, C.A. Boyd & D.F. Saunders. (1953, April). Thermoluminescence as a research tool. American Association for the Advancement of Science [Online]. Vol. 117, issue 3040. Available: https://www.jstor.org/stable/1680489.

[11] R.K. Bull (1986). Thermoluminescence and its applications: an introduction. Nucl. Tracks Radiat Meas 11 : 105-113.

[12] C. Furetta (1937). Hnadbook of thermoluminescence, 1st ed. World scientific publishing Co. Pte. Ltd.

[13] C. M. Sunta (2015). Unraveling Thermoluminescence, 1st ed. Springer New Delhi.

[14] R. Chen (2019). Recent advances in the theory of thermoluminescence and optically stimulated luminescence; delocalized transitions. In Advances in Physics and Applications of Optically and Thermally Stimulated Luminescence, R. Chen, V. Pagonis, Eds, World Scientific Publishing Europe Ltd, London.

[15] M.N. Konopka, P. Bilski, B. Obryk, B. Marczewska, P. Olko, M. Klosowski & W. Gieszczyk (2017). Luminescence dosimetry : review of methods, detectors and their applications. Nonlinear Optics and Quantum Optics 48 : 133-146.

[16] L. Bøtter-Jensen (2000). Development of Optically Stimulated Luminescence Techniques using Natural Minerals and Ceramics, and their Application to Retrospective Dosimetry. Ph.D. thesis, Risø National Laboratory, Roskilde.

[17] J. Prakash (2013). Thermoluminescence glow curve involving any extent of retrapping or any order of kinetics. Parmana- J Phys 81 : 521-533.

[18] R. Chen (1983). On the order of kinetics in the study of thermoluminescence. J Phys D: Appl Phys 16 : L107-L114.

[19] R. Chen (2020). Conduction band-valence band theory of TL and OSL : emphasis on delocalized transitions and explanation on some unsual effects. Radiat Prot Dosim 192(2) : 176-195.

[20] A.J.J. Bos (2017). Thermoluminescence as a research tool to investigate luminescence mechanisms. Materials 10(12) :1357.

[21] K.V.R. Murthy (2014). Thermoluminescence and its apllications : a review. Defect and Diffusion Forum 347 : 35-73.

[22] R. Chen and V. Pagonis (2013). On the expected order of kinetics in a series of thermoluminescence (TL) and thermally stimulated conductivity (TSC) peaks. Nuclear Instruments and Methods in Physics Research B 213 : 60-69.

[23] A. Hugo, Borbón-Nuñez & C. Furetta, (2017, October). Activation energy of modified peak shape equations. World Journal of Nuclear Science and Technology. DOI: 10.4236/wjnst.2017.74021.

[24] R.A. Clark (2012). Intrinsic dosimetry: properties and mechanisms of thermoluminescence in commercial borosilicate glass. Ph.D. Dissertation, Dept. Energy, Missouri Univ. Washington.

[25] M. Zahedifar, S. Harooni & E. Sadeghi (2011). Thermoluminescence kinetic analysis of quartz using an improved general order model for exponential distribution of activation energies. Nuclear Instruments and Methods in Physics Research A 654 : 569-574.

[26] G. Kitis, C. Furetta, & J. Azorin (2003). Observations on the properties of second and general-order kinetics equations describing the thermoluminescence processes.

[27] A.J.J. Bos, Theory of thermoluminescence, Radiat Meas 41(6) : S45-S56, 2007.

[28] G.F.J. Garlick, & A.F. Gibson (1948). The Electron trap mechanism of luminescence in sulphide and silicate phosphors. In Proc. Phys. Soc. 60 574.

[29] W. Hoogenstraaten (1958). Electron traps in zinc-sulphide phosphors. California Univ. Philips Res. Rep. 13.

[30] R. Chen (1969). Glow curves with general order kinetics. J Electrochem Soc: Solid state science 116(9) : 1254.

[31] Y.S. Horowitz, & D. Yossian (1995). Computerised glow curve deconvolution: application to thermoluminescence dosimetry. Radiat Prot Dosim 60(1) : 1-114.

[32] E.B. Podgorsak, P.R. Moran, & J.R. Cameron (1971). In Proc. 3rd Int. Conf. On Luminescence Dosimetry, Riso, 11-14 October.

[33] G. Kitis, J.M. Gomez-Ros, & J.W.N Tuyn (1998). Thermoluminescence glow-curve deconvolution functions of first, second and general orders of kinetics. J Phys D: Appl Phys 31 : 2636.

[34] S.H. Tatumi, D.F. Rossetti, & E.A. Amaral Soares (2020). Optically stimulated luminescence (OSL) dating in the Amazonian Wetlands, 1st ed. Cambridge scholars publishing.

[35] M.S. Akselrod (2011). Fundamentals of materials, techniques, and instrumentation for OSL and FNTD dosimetry. In AIP Conf. Proc. Concepts and trends in medical radiation dosimetry, Wollongong, Australia, pp. 274-302.

[36] V.V. Antonov-Romanovskiĭ, I.B. Keirim-Markus, M.S. Poroshina, & Z. A. Trapeznikova (1956). Dosimetry of Ionizing Radiation with the Aid of Infra-red Sensitive Phosphors. USAEC Report, Moscow, pp. 239-250.

[37] S.F. Kry, P. Alvarez, J.E. Cygler, L.A. DeWerd, R.M. Howell, S. Meeks, J. O'Daniel, C. Reft, G. Sawakuchi, E.G. Yukihara & D. Mihailidis (2020). Clinical use of luminescent dosimeters: TLDs and OSLDs. Med Phys 47(2), doi: 10.1002/mp.13839.

[38] K.J. Thomsen, (2004). Optically stimulated luminescence techniques in retrospective dosimetry using single grains of quartz extracted from unheated materials. Ph.D. Thesis. Risø National Laboratory. Roskilde, Denmark. ISBN: 87-550-3307-5.

[39] E.G. Yukihara, & S.W.S. Mckeever (2011). Optically stimulated luminescence, fundamentals and applications. John Wiley & Sons Ltd, Oklahoma, USA.

[40] M.S. Akselrod, L. Bøtter-Jensen, & S.W.S. McKeever (2007). Optically stimulated luminescence and its use in medical dosimetry. Radiat. Meas., vol. 41 : S78-S99.

[41] B. Hu (2010). Optically stimulated luminescence (OSL) and its applications in radiation therapy dosimetry. Ph.D. Thesis, Enginnering Physics, Wollongong Univ.

[42] M.L. Chithambo (2018). Introduction. In: An introduction to time-resolved optically stimulated luminescence. Institute of Physics ebooks, Morgan and Claypool, Bristol. ISBN 9781643271989 (ebook).

[43] L. Bøtter-Jensen, S.W.S. Mckeever, & A.G. Wintle (2003). Optically stimulated luminescence dosimetry. Eds. Elsevier, Amsterdam.

[44] A. Bluszcz, & G. Adamiec (2006). Application of differential evolution to fitting OSL decay curves. Radiat Meas 41 : 886-891.

[45] J.W. Poston (2003). Dosimetry. In : Encyclopedia of Physical Science and Technology (Third Edition), A.R. Meyers. Eds. Academic Press : San Diego. https://doi.org/10.1016/B0-12-227410-5/00185-X.

[46] E.G. Yukihara, S.W.S. McKeever, C.E. Andersen, A.J.J. Bos, I.K. Bailiff, E.M. Yoshimura, G.O. Sawakuchi, L. Bossin, & J.B. Christensen (2022). Luminescence dosimetry. Nat Rev Methods Primers 2 (26). https://doi.org/10.1038/s43586-022-00102-0.

[47] H. Stadtmann (2001). Dose quantities in radiation protection and dosemeter calibration. Radiat Prot Dosim 96 (1-3) : 21-26.

[48] N. Jean-Claude, B. Jean, L. Dominique, R. Alain, T. Dominique (2009). The 2007 Recommendations of the International Commission on Radiological Protection. ICRP publication 103. Institut de Radioprotection et de Surete Nucleaire, France.

[49] the same as [42 [3] in introduction] R. Chen & V. Pagonis (2011). Thermally and optically stimulated luminescence: A stimulation approach, 1st ed. John Wiley & Sons.

[50] R. Chen & S. W. S. McKeever (1997). Theory of thermoluminescence and related phenomena. World Scientific. https://books.google.dz/books?id=jcmFRLktMPQC.

[51] I.K. Bailiff, V.F. Stepanenko, H.Y. Göksu, L. Bøtter-Jensen, V. Correcher, A. Delgado, H. Jungner, L.G. Khamidova, T.V. Kolizshenkov, R. Meckbach, D.V. Petin, M.Yu. Orlov &

S.A. Petrov (2005). Retrospective luminescence dosimetry : development of approaches to application in populated areas downwind of the Chernobyl NPP. Health Physics 89 (3).
[52] ICRP (1991), 1990 Recommendations of the International Commission on Radiological Protection-60.
[53] ICRP (1997), General principles for the radiation of workers, ICRP Publication 75.
[54] S.W.S. Mckeever (2022). A course in luminescence measurements and analyses for radiation dosimetry. John Wiley & Sons Ltd. ISBN:9781119646891.
[55] B.C. Bhatt (2010). Thermoluminescence, optically stimulated luminescence and radiophotoluminescence dosimetry - an overall perspective. India: Bhabha Atomic Research Centre.
[56] I.H. Taam, L.A.R. da Rosa & V.R. Crispim (2008). TLD environmental monitoring at the Insitute of Nuclear Engineering in Brazil. Appl. Radiat. Isot., vol. 66 : 1229-1234.
[57] T. Kron (INVITED) (1999). Applications of thermoluminescence dosimetry in medicine. Radiat Prot Dosim 85(1-4) :333–340, https://doi.org/10.1093/oxfordjournals.rpd.a032865.
[58] C.E. Andersen, S.K. Nielsen, S. Greilich, J. Helt-Hansen, J. C. Lindegaard & K. Tanderup (2009). Characterization of a fiber-coupled Al_2O_3:C luminescence dosimetry system for online in vivo dose verification during 192Ir brachytherapy. Medical physics 36(3) : 708–718. https://doi.org/10.1118/1.3063006.
[59] NCRP-2002, the National Council of Radiation Protection and Measurements, Bethesda, Maryland, NCRP Report 142 (2002).
[60] [34 of chap 1] S.F. Kry, P. Alvarez, J.E. Cygler, L.A. DeWerd, R.M. Howell, S. Meeks, J. O'Daniel, C. Reft, G. Sawakuchi, E.G. Yukihara & D. Mihailidis (2020). Clinical use of luminescent dosimeters: TLDs and OSLDs. Med Phys., vol. 47(2), doi: 10.1002/mp.13839.

[61] R.Dz. Mshelia, N.I. Dibal & S.M. Chiroma (2023). Food irradiation: an effective but under-utilized technique for food preservations. J Food Sci Technol., vol. 60, 2517–2525, https://doi.org/10.1007/s13197-022-05564-4.

[62] J. Izewska & G. Rajan (2005). Radiation Dosimeters. In: Radiation oncology physics: A Handbook for Teachers and Students, E.B. Podgorsak, Eds. International Atomic Energy Agency-IAEA, Vienna.

[63] G. Marinello (1996). Thermoluminescence dosimetry applied to quality assurance in radiotherapy, brachytherapy and radiodiagnostic (IAEA-TECDOC--896). International Atomic Energy Agency (IAEA).

[64] N.S. Rawat (2012). Characterization of TL/OSL phosphors and study of photo-ionization cross-sections of meta-stable trap levels – An experimental and theoretical approach. Physical Sciences Faculty, Homi Bhabha National Institute, India.

[65] E.G. Yukihara, A.J.J. Bos, P. Bolski & S.W.S. Mckeever (2022). The quest for new thermoluminescence and optically stimulated luminescence materials: Needs, strategies and pitfalls. Radiat. Meas., vol. 158 : 106846.

[66] F. Sagastibelza & J.L. Alvarez Rivas (1981). Thermoluminescence in LiF (TLD-100) and LiF crystals irradiated at room temperature. J. Phys. C : Solid State Phys., vol. 14 : 1873-1889.

[67] P. Seth, S. Aggarwal, S. Bahl & Pratik kumar (2022). Optically stimulated luminescence dosimetry on tissue equivalent LiF : Mg, Cu, Na, Si phosphor. Optik, vol. 260 : 169060.

[68] G. Massillon-JL, C.S.N. Johnston & J. Kohanoff (2018). On the role of magnesium in a LiF:Mg, Ti thermoluminescent dosimeter. J. Phys. : Condensed Matter, vol. 31(2) : 025502.

[69] K. Prokert & M. Sommer (1998). A new hypersensitive thermoluminophor based on CaF_2. Radiat. Prot. Dosim., vol. 78 (4) : 249-256.

[70] A.L.M.C. Malthez, B. Marczewska, F. Ferreira, N.K. Umisedo, T. Nowak, P. Bilski & E.M. Yoshimura (2018). OSL dosimetric properties and efficiency of Brazilian natural calcium fluoride pellets. Appl. Radiat. Isot., vol. 135 : 166-170.

[71] P. Brovetto, A. Delunas, A. Floris, V. Maxia, M. Murgia & G. Spano (1990). Investigation on CaF_2 lattice defects by thermoluminescence experiments. Il Nuovo Cimento 12 D : 1651–1665. https://doi.org/10.1007/BF02451265.

[72] D.N. Batchelder & R.O. Simmons (1964). Lattice constants and thermal expansivities of silicon and of calcium fluoride between 6° and 322° K. J. Chem. Phys., vol. 41 : 2324-2329.

[73] E. Bulur & H.Y. Göksu (1998). OSL from BeO ceramics: new observations from an old material. Radiat. Meas., vol. 29(6) : 639-650.

[74] H.F. Song, H.F. Liu & E. Tian (2007). Structural and thermodynamic properties of hexagonal BeO at high pressures and temperatures. J. Phys.: Condens. Matter, vol. 19: 456209.

[75] E. Aşlar, N. Meriç, E. Şahiner, O. Erdem, G. Kitis & G.S. Polymeris (2019). A correlation study on the TL, OSL and ESR signals in commercial BeO dosimeters yielding intense transfer effects. J. Lumin., vol. 214: 116533, doi: https://doi.org/10.1016/j.jlumin.2019.116533.

[76] S.W.S. McKeever, M. Moscovitch & P.D. Townsend (1995). Thermoluminescence dosimetry materials: properties and uses. United Kingdom: Nuclear Technology Publishing.

[77] A.J.J. Bos, M. Prokić & J.C. Brouwer (2006). Optically and thermally stimulated luminescence characteristics of MgO:Tb^{3+}. Radiat. Prot. Dosim., vol. 119(1-4) : 130-133.

[78] M.A. Rajab, S.A. Salman & M.N. Abdullah (2020). Effect of nanoparticles and fibers types on hybrid blend composite materials behavior of epoxy and phenol-fomaldehyde. Int. J. Nanoelectron. Mater., vol. 13(1) : 91-100.

[79] O. Margit.& T. BIRO (1980). Aluminium oxide in TL Dosimetry. Nucl. Instr. Meth,vol. 175, 60-61.

[80] S.W.S. Mckeever & M. Moscovitch (2003). On the advantages and disadvantages of optically stimulated luminescence dosimetry and thermoluminescence dosimetry. Radiat. Prot. Dosim., vol. 104: 263-270.

[81] T. Yamashita, N. Nada, H. Onishi & S. Kitamura (1971). Calcium sulfate activated by thulium or dysprosium for thermoluminescence dosimetry, Health Phys., vol. 21: 295.

[82] N.T. Mandlik, S.R. Rondiya, N.Y. Dzade, M.S. Kulkarni, P.D. Sahare, B.C. Bhatt & S.D. Dhole (2020). Thermoluminescence, photoluminescence and optically stimulated luminescence characteristics of $CaSO_4$:Eu phosphor: experimental and density functional theory (DFT) investigations. Journal of Luminescence, vol. 221 : 117051.

[83] C.L.P. Mauricio, E. Bortolin & S. Onor (1996). ESR study of $CaSO_4$:Dy TLD. Radiat. Meas., vol. 26(4): 639-644.

[84] N.F. Cano, T.K.G. Rao, J.S.A. Arenas, H.S. Javier-Ccallata & S. Watanabe (2021). EPR response of anhydrite crystal ($CaSO_4$) for dosimetry of gamma photon beams. Radiat. Phys. Chem., vol. 180 :109231.

[85] C. Furetta, M. Prokic, R. Salamon, V. Prokic & G. Kitis (2001). Dosimetric characteristics of tissue equivalent thermoluminescent solid TL detectors based on lithium borate. Nuclear Instruments and Methods in Physics Research Section A: Accelerators, Spectrometers, Detectors and Associated Equipment, vol. 456 : 411–417.

[86] M.W. Swinney, J.W. McClory, J.C. Petrosky, S. Yang, A.T. Brant, V.T. Adamiv, Y.V. Burak, P.A. dowben & L.E. Halliburton (2010). I dentification of electron and hole tras in lithium tetraborate ($Li_2B_4O_7$) crystals : Oxygen vacancies and lithium vacancies. J. Appl. Phys., vol. 107 : 113715.

[87] Diamond® 3.0 software. Crystal Impact.

[88] G.F.C. Bispo, D.S. Nascimento, L.B. Santana G.S. Ferreira, H.R.B.R. Lima, S.O. Souza, F. d'Errico, R.A. Jackson & M.E.G. Valerio (2022). Defects in MgB_4O_7 (pure and doped with lanthanides): a case study using a computational modelling approach. Phys. B: Condens. Matter, vol. 640 : 414049.

[89] A. Ozdemir, V. Altunal, V. Guckan, K. Kurt, Z. Yegingil (2021). LLuminescence charateristics of newly-developed MgB_4O_7: Ce^{3+}, Na^+ pgosphor as an OSL dosimeter. J. Alloys Compd., vol. 865 : 158498.

[90] H. Bartl & W. Schuckmann (1966), Zur Struktur des Magnesiumdiborats, $MgO(B_2O_3)_2$, Neues Jahrbuch Für Mineralogie – Monatshefte, vol. 2 : 142–148.

[91] P.D. Townsend, Y. Wang & S.W.S. McKeever (2021). Spectral evidence for defect clustering: relevance to radiation dosimetry materials. Radiat. Meas., vol. 147 : 106634.

[92] d. Bokov, A.T.Jalil, S. Chupradit, W. Suksatan, M.J. Ansari, I.H. Shewael, G.H. Valiev & E. Kianfar (2021). Nanomaterial by sol-gel method: synthesis and application. Adv. Mater. Sci. Eng., vol. 2021 : 1-21.

[93] S. Ebnesajjad (2011). 4 - Surface and Material Characterization Techniques. In : Handbook of Adhesives and Surface Preparation. William Andrew Publishin, pp. 31-48.

[94] A.A. Bunaciu, E.G. Udriştioiu & H.Y. Aboul-Enein (2015). X-Ray Diffraction: Instrumentation and Applications. Crit Rev Anal Chem ., vol. 45(4) : 289-299, doi: 10.1080/10408347.2014.949616.

[95] P.B. Raja, K.R. Munusamy, V. Perumal & M.N.M. Ibrahim (2022). 5 - Characterization of nanomaterial used in nanobioremediation. In : Micro and nano technologies, Nano Bioremediation : Fundamentals and applications, H.M.N. Iqbal, M. Bilal & T.A. Nguyen, Elsevier.

[96] R. E. Kirk & D. F. Othmer (1953). Encyclopedia of chemical technology, vol. 2. The Interscience Encyclopedia, Inc; New York.

[97] J.I. Goldstein, D.E. Newbury, J.R. Michael, N.W.M. Ritchie, J.H.J. Scott & D.C. Joy (2018). Scanning Electron Microscope (SEM) Instrumentation. In: Scanning Electron Microscopy and X-Ray Microanalysis. Springer, New York, NY. https://doi.org/10.1007/978-1-4939-6676-9_5.

[98] F. Kharfi F & R. Ketfi (2018). Irradiated black pepper identification based on thermoluminescence of silicate minerals, Journal of Radioanalytical and Nuclear Chemistry 315 : 503–507.

[99] Risø (2015). Guide to the Risø TL/OSL Reader, DTU Nutech. Denmark.

[100] J.T. Dawley, P.G. Clem, T.J. Boyle, L.M. Ottley, D.L. Overmyer & MP Siegal (2004). Rapid processing method for solution deposited $YBa_2Cu_3O_7$-γ thin films. Phys. C: Supercond., vol. 402:143–151.

[101] D. Mondelares, G. Vanhoyland, H. Van den Rul, J. D'Haen, M.K. Van Bael, J. Mullens & L.C. Van Poucke (2002). Synthesis of ZnO nanopowder via an aqueous acetate-citrate gelation method. Mater. Res. Bull., vol. 37(5) : 901–914.

[102] J. Li, Y. Pan, C. Xiang, Q. Ge & J. Guo (2006). Low-temperature synthesis of ultrafine α-Al_2O_3 powder by a simple aqueous sol-gel process. Ceram. Int., vol. 32(5) : 587–591.

[103] K.C. Song, K.J. Woo &Y. Kang (1999). Preparation of alumina fibers from aluminum salts by the sol-gel method. Korean J. Chem. Eng., vol. 16(1) : 75–81.

[104] K. Li & T. Kobayashi (2016). A FT-IR spectroscopic study of ultrasound effect on aqueous imidazole based ionic liquids having different counter ions. Ultrason. Sonochem., vol. 28 : 39–46.

[105] H.M. Said, S.G. Abd Alla & A.W.M. El-Naggar (2004). Synthesis and characterization of novel gels based on carboxymethyl cellulose/acrylic acid prepared by electron beam irradiation. React. Funct. Polym., vol. 61 : 397–404.

[106] Z. Filip, S. Hermann & K. Demnerova (2008). FT-IR spectroscopic characteristics of differently cultivated Escherichia coli. Czech. J. Food Sci., vol. 26 : 458–463.

[107] A. Khodadadi, M. Farahmandjou & M. Yaghoubi (2018). Investigation on synthesis and characterization of Fe-doped Al_2O_3 nanocrystals by new sol-gel precursors. Mater. Res. Express, vol. 6.

[108] Y.P. Gómez Espinoza, M.R. Pérez, E.G.P. Beas, J.C. Juárez Tapia, M. Pérez-Labra, I.A.R. Domínguez, M.U.F. Guerrero & V.E.R Cruz (2020). Characterization by FTIR of oxidized pyrargyrite with sodium sulfide. In: Characterization of Minerals, Metals, and Materials. The Minerals, Metals & Materials Series. Springer, Cham.

[109] A. Faraji Alamouti, M. Nadafan, Z. Dehghani, M.H. Majles Ara & A. Vejdani Noghreiyan (2020). Structural and optical coefficients investigation of γ-Al_2O_3 nanoparticles using Kramers-Kronig relations and Z-scan technique. J. Asian Ceram. Societies, vol. 9(1) : 366–373.

[110] C.X. Zhang, Q. Tang, L.B. Lin & D.L. Luo (2006). Thermoluminescence glow curves and optical stimulated luminescence of undoped α- Al_2O_3 crystals. Radiat. Prot. Dosim., vol. 119 : 402–407.

[111] D. Ekendahl & L. Judas (2012). Retrospective dosimetry with alumina substrate from electronic components. Radiat. Prot. Dosim., vol. 150 : 134–141.

[112] A.N. Yazici, S. Solak, Z. Özturk, M. Topaksu & Z. Yegingil (2003). The analysis of dosimetric thermoluminescent glow peak of α-Al_2O_3:C after different dose levels by β-irradiation. J. Phys. D.: Appl. Phys., vol. 36 : 181–191.

[113] W.M. de Azevedo, G.B. de Oliveira, E.F. da Silva Jr, H.J. Khoury & E.F. Oliveira de Jesus (2006). Highly sensitive thermoluminescent carbon doped nanoporous aluminium oxide detectors. Radiat. Prot. Dosim., vol. 119 : 201–205.

[114] J. Singh, J. Manam & F. Singh (2017). Thermoluminescence studies of solid-state reaction derived and γ-irradiated $SrGd_2O_4:Eu^{3+}$. Mater. Res. Bull., vol. 93 : 318–324.

[115] P.P. Pal & J. Manam (2013). Photoluminescence and thermoluminescence studies of Tb^{3+} doped ZnO nanorods. Mater. Sci. Eng. B, vol. 178 : 400–408.

[116] S.S. Reddy, K.R. Nagabhushana & F. Singh (2017). Mechanism of thermoluminescence in high energy carbon ion irradiated Tb^{3+} doped Al_2O_3 phosphor for carbon ion beam dosimetry. Mater. Res. Express, vol. 4.

[117] L.C. Matsushima, G.R.Veneziani, R.K. Sakuraba, J.C. Cruz & L.L. Campos (2015). TL and OSL dose response of LiF:Mg,Ti and Al_2O_3:C dosimeters using a PMMA phantom for IMRT technique quality assurance. Appl. Radiat. Isotopes, vol. 100:7–10.

[118] E. Aşlar, E. Şahiner, G.S. Polymeris & N. Meriç (2021). Thermally and optically stimulated luminescence properties of BeO dosimeter with double TL peak in the main dosimetric region. Appl Radiat Isot 170 : 109635.

[119] S. Şahin, E. Şahiner, F. Göksel & N. Meriç (2020). Comprehensive evaluation of electron radiation dose using beryllium oxide dosimeters at breast radiotherapy. J Radiother Pract 19 (1) : 38–44.

[120] M. Puchalska & P. Bilski (2006). GlowFit-a new tool for thermoluminescence glow-curve deconvolution. Radiat Meas 41 (6) : 659–664.

[121] M. Abramowitz & I.A. Stegun (1972). Handbook of Mathematical Functions. Tenth Printing, Washington, D.C.

[122] A.J.J. Bos, T.M. Piters, J.M. Gomez Ros & A. Delgado (1993). An intercomparison of glow curve analysis computer programs: I. Synthetic glow curves. Radiat. Protect. Dosim. 47 (1–4) : 473–477.

[123] H.G. Balian & N.W. Eddy (1977). Figure-Of-Merit (FOM), an improved criterion over the normalized chi-squared test for assessing goodness-of-fit of gamma-ray spectral peaks. Nucl Instrum Methods 145 : 389–395.

[124] F.J. Algarve & L.V.E. Caldas (2018). Determination of the kinetic parameters of BeO thermoluminescent samples using different methods. Braz. J Rad Sci 6 (2) : 1–12.

[125] E. Aşlar, E. Şahiner, G.S. Polymeris & N. Meriç (2017). Determination of trapping parameters in BeO ceramics in both quenched as well as reconstructed thermoluminescence glow curves using various analysis methods. Appl Radiat Isot 129 : 142–151.

[126] V.S. Kortov & I.I. Milman (1996). Luminescence properties of transparent BeO: Li ceramics. Radiat Protect Dosim 65 (1–4) : 355–358.

[127] M.T. Jose, S.R. Anishia, O. Annalakshmi & V. Ramasamy (2011). Determination of thermoluminescence kinetic parameters of thulium doped lithium calcium borate. Radiat Meas 46 : 1026–1032.

[128] R.M. Baltezar & J.A. Nieto (2019). Analysis of the BeO thermoluminescent glow curve by the deconvolution method. Appl Radiat Isot 150 : 53–56.

Abstract: The main objective of this doctoral thesis project is the elaboration by sol-gel process and characterization by different techniques of Sb-doped Al_2O_3 (Al_2O_3:Sb). BeO dosimetry material was also characterized in terms of dose-response and luminescence kinetics. The tested dose-response, energy dependence and repeatability of Al_2O_3:Sb were optimal, by producing higher TL and OSL intensity signals, for an Sb dopant optimal amount of ~1 wt%. The dose-response of $Al_2O_3:Sb_{1\%}$ was linear of both TL&OSL signals within the studied dose range (0-80 Gy). The dose-response and the energy dependence (5 keV-18 MeV) of this material allow effective use in high-energy radiation detection and dosimetry. Repeatability test indicates standard deviation values of 4.4% for TL and 2.8% for OSL. The elaborated cheap and efficient Sb-doped Al_2O_3 TL-OSL material exhibits the same level performance as commercial Al_2O_3:C. The TL and OSL kinetics of a recently developed beryllium-oxide dosimeter BeO_R have been studied using different methods, namely: peak shape (PS), FOK-GlowFit and GOK-CGCD. Main kinetics parameters were extracted and compared. Established kinetics and dose-response of BeO_R demonstrate an advantage in the application of such dosimeter for photon dosimetry in radiotherapy.

Keywords: Thermoluminescence, Optically stimulated luminescence, BeO_R, Al_2O_3:Sb TL-OSL dosimeter, Sol gel process, Luminescence kinetics.

Résumé: L'objectif principal de ce projet de thèse de doctorat est l'élaboration par procédé sol-gel et la caractérisation par différentes techniques de Sb-dopé Al_2O_3 (Al_2O_3:Sb). Le matériau de dosimétrie BeO a également été caractérisé en termes de cinétique de dose-réponse et de luminescence. La dose-réponse testée, la dépendance énergétique et la répétabilité d'Al_2O_3:Sb étaient optimales, en produisant des signaux d'intensité TL et OSL plus élevés, pour une quantité optimale de dopant Sb de ~1 wt%. La réponse dose-réponse d'$Al_2O_3:Sb_{1\%}$ était linéaire des deux signaux TL&OSL dans la gamme de dose étudiée (0-80 Gy). La relation dose-réponse et la dépendance énergétique (5 keV-18 MeV) de ce matériau permettent une utilisation efficace dans la détection et la dosimétrie des rayonnements à haute énergie. Le test de répétabilité indique des valeurs d'écart type de 4,4 % pour TL et de 2,8 % pour OSL. Le matériau Al_2O_3 TL-OSL dopé Sb, bon marché et efficace, présente les mêmes performances que l'Al_2O_3:C commercialisé. Les cinétiques TL et OSL d'un dosimètre récemment développé à base d'oxyde de béryllium BeO_R ont été étudiés à l'aide de différentes méthodes, nommées: la forme du pic (PS), FOK-GlowFit et GOK-CGCD. Les principaux paramètres cinétiques ont été extraits et comparés. La cinétique et la réponse en dose établies du BeO_R démontrent un avantage dans l'application d'un tel dosimètre pour la dosimétrie des photons en radiothérapie.

Mots clés: Thermoluminescence, Luminescence stimulée optiquement, BeO_R, Dosimètre TL-OSL Al_2O_3:Sb, Sol-gel procédé, Cinétique de luminescence.

ملخص: الهدف الرئيسي لمشروع اطروحة الدكتوراه هذا هو إعداد عن طريق عملية صول-جل (sol-gel) و توصيف بالاستعانة بتقنيات مختلفة Al_2O_3 المنشط ب Sb (Al_2O_3:Sb). كما تم توصيف مادة قياس الجرعات BeO من حيث الاستجابة للجرعة وحركية التألق. كانت الاستجابة للجرعة التي تم اختبارها والاعتماد على الطاقة وقابلية التكرار الخاصة ب Al_2O_3:Sb مثالية، من خلال إنتاج إشارات شدة TL و OSL أعلى، لكمية مثلى من المنشط Sb تبلغ ~ 1 wt٪. كانت استجابة جرعة Al_2O_3 :$Sb_{1\%}$ خطية لكل من إشارات TL و OSL ضمن نطاق الجرعة المدروسة (0-80 Gy). تسمح الاستجابة للجرعة والاعتماد على الطاقة (5 keV-18 MeV) لهذه المادة بالاستخدام الفعال في الكشف عن الإشعاع عالي الطاقة وقياس الجرعات. يشير اختبار التكرار إلى قيم انحراف قياسية تبلغ 4.4% لـ TL و2.8% لـ OSL. تُظهر مادة TL-OSL Al_2O_3 المنشط ب Sb الغير مكلفة والفعالة المعدة نفس الأداء مثل Al_2O_3:C التجارية. تمت دراسة حركية التألق الحراري والتألق المحفز ضوئيا لمقياس جرعة أكسيد البيريليوم BeO_R الذي تم تطويره مؤخرًا باستخدام طرق مختلفة، وهي: شكل الذروة (PS) و FOK-GlowFit و GOK-CGCD. تم استخراج ومقارنة معلمات الحركية الرئيسية. تُظهر الحركية المنشأة واستجابة الجرعة لـ BeO_R ميزة في تطبيق مقياس الجرعات هذا لقياس جرعات الفوتون في العلاج الإشعاعي.

كلمات مفتاحية: التألق الحراري، التألق المحفز ضوئيا، أوكسيد البيريليوم، مقياس جرعات Al_2O_3:Sb حراري-محفز ضوئيا ، عملية الصول-جل، حركية التألق.